The Virtual Source Method: Implementation Issues, Improvement Using Wavefield Separation and Application to Time-Lapse Monitoring

Kurang Mehta

— Doctoral Thesis —
Geophysics

Defended December 2006

Advisor: Dr. Roel Snieder
Committee members: Dr. Masami Nakagawa
                     Dr. Paul Sava
                     Dr. David Wald
                     Dr. Mike Mooney
                     Dr. Rodney Calvert
                     Dr. Ken Larner

Abstract

The virtual source method is a technique to image and monitor below a complex and time-varying overburden without the knowledge of overburden velocities and near-surface changes. It is based on extracting the response between a given pair of receivers by correlating the wavefields recorded by them and stacking over the physical sources. There are several challenges that arise while generating virtual source data, such as the maximum allowable spacing of the physical sources, limited acquisition aperture and reflections/multiples from the overburden, that need to be addressed.

Some of these challenges can be overcome by separating the wavefield into upgoing and downgoing waves. Wavefield separation not only suppresses the artifacts associated with the limited acquisition aperture typically used in practice, but also helps reconstruct a response in the absence of downgoing reflections and multiples from the overburden. These improvements in removing the artifacts caused by limited acquisition aperture and overburden-related multiples are illustrated on a synthetic dataset of a complex layered model modeled after the Fahud field in Oman, and on OBC data acquired in the Mars field in the deepwater Gulf of Mexico.

The virtual source method requires surface shooting recorded by subsurface receivers placed below the distorting or changing part of the overburden. Redatuming the recorded response to the receiver locations allows the reconstruction of a complete downhole survey as if the sources were also buried at the receiver locations. The ability to redatum the data independent of the knowledge of time-varying overburden velocities makes the virtual source method a valuable tool for time-lapse monitoring. The virtual source method is applied to the Mars field OBC data acquired in the deepwater Gulf of Mexico with 120 multi-component sensors permanently placed on the seafloor. Applying a combination of wavefield separation and deconvolution of the correlation gather by the source power spectrum to the virtual source method suppresses the causes of non-repeatability in the overburden (sea water) and acquisition discrepancies, forming the basis for the improvement the virtual source method offers for time-lapse monitoring.

When the two wavefields recorded by the receivers are correlated, along with the estimation of the Green's function between the two receivers the correlation also contains the power spectrum of the source-time function. For a short duration source, the correlated data can be deconvolved by the source power spectrum. When, however, the source-time function is long and difficult to estimate (e.g., earthquake or other passive seismic recording), deconvolution as opposed to correlation becomes a preferred seismic interferometric tool because the deconvolved wavefield is independent of the source-time function. To demonstrate the usefulness of deconvolution as a tool for seismic interferometry, the method is applied to earthquake waves recorded in a borehole to extract near-surface properties such as the 1-D velocity profile. Furthermore, a connection is established between the decon-

volved waveforms and the elements of the propagator matrix. Using the same earthquake recording, a P-to-S mode conversion is characterized by extending the application of the receiver function to downhole measurements.

Table of Contents

Acknowledgment

Chapter 1

Introduction

The virtual source method (Bakulin and Calvert, 2004, 2006; Calvert, et al., 2004) has recently been proposed to image and monitor below a complex and time-varying overburden without the knowledge of overburden velocities and near surface changes. The virtual source method is a form of seismic interferometry (Lobkis and Weaver, 2001; Derode, et al., 2003; Schuster, et al., 2004; Snieder, 2004; Wapenaar, 2004; Wapenaar, et al., 2005; Korneev and Bakulin, 2006; Snieder, et al., 2006a; Larose, et al., 2006; Curtis, et al., 2006; Wapenaar and Fokkema, 2006; Draganov, et al., 2006). Theory states that if a given pair of receivers record waves excited by sources that populate a closed surface enclosing the two receivers, the correlation of the wavefield recorded by the receivers when stacked over the physical sources gives the true impulse response between the receivers.

To implement the virtual source method, the wavefield recorded by a given reference receiver is correlated with that by every other receiver and stacked over the physical sources. The resultant virtual source gather is comparable to the shot gather generated by putting a physical source at the reference receiver location. Since there is no real source at the reference receiver location, this method is referred to as the *virtual source method* (Bakulin and Calvert, 2004, 2006; Calvert, et al., 2004; Korneev and Bakulin, 2006). A crucial advantage of the virtual source method is the ability to image below a complex and time-varying overburden, provided the receivers are placed below it. Another advantage of the virtual source method is that the wavefield recorded by the two receivers can be generated either by active sources or by incoherent sources such as ambient noise (Curtis, et al., 2006; Larose, et al., 2006; Sabra, et al., 2005; Shapiro, et al., 2005; Shapiro and Campillo, 2004; Artman, 2006). To understand the practicality of seismic interferometry, van Wijk (2006) used a controlled ultrasonic experiment to retrieve a band-limited estimate of the Green's function between receivers in an elastic medium.

Correlation of the wavefields recorded by a given pair of receivers followed by deconvolution of the source power spectrum gives the true impulse response between them provided the receivers are surrounded by physical sources. For geophysical applications, however, it is impractical to have sources surrounding the receivers. To overcome a part of this limitation, scattering in a complex and heterogeneous overburden assists by allowing waves to arrive at the receivers from a larger possible range of directions, hence improving the focusing of the energy at the virtual source location (Fink, 1993, 1999; Clouet and Fouque, 1997; Borcea, et al., 2002; Borcea, et al., 2003; Parvulescu, 1995; Blomgren, et al., 2002; Mehta and Snieder, 2006; Haider, et al., 2004).

The virtual source method has several implementation issues and challenges that one

encounters while redatuming with the recorded Green's function to reconstruct a complete downhole survey as if the sources were also buried at the receiver locations. An important implementation issue is the maximum allowable spacing of the physical sources to prevent spatial aliasing in the virtual source data (Mehta and Snieder, 2007). The prestack correlated data (i.e., correlation gather) is a useful tool for designing the maximum allowable source spacing for a specific acquisition geometry. It is also useful to determine the source locations that give the stationary phase contribution (Wapenaar, et al., 2005; Snieder, et al., 2006a). Other implementation issues and challenges arise because of incomplete source aperture, reflections/multiples coming from the overburden, and edge-effects generated while stacking the correlation gather over the physical sources, due to the contribution of the sources at the ends of the source aperture.

The challenges attributable to incomplete source aperture and reflections/multiples coming from the overburden can be overcome by incorporating a combination of up-down wavefield separation and time-windowing of the direct arrival in the virtual source method (Mehta, et al., 2007b). The current practice in generating a virtual source gather involves correlating the direct arrival time-windowed in the total wavefield at the virtual source with the total wavefield at the receivers. This practice imposes the downward radiation pattern on the virtual source but cannot suppress the spurious events arising from incomplete source aperture and overburden multiples. To suppress these spurious events, a better approach to generating a virtual source gather is to correlate the direct arrival time-windowed in the downgoing waves at the virtual source with the upgoing waves at the receivers.

The ability to redatum the data independent of knowledge of time-varying overburden velocities makes the virtual source method a valuable tool for time-lapse monitoring. Conventionally, changes in the subsurface can be tracked by observing differences between two seismic surveys obtained over the surveillance period. Apart from changes in the subsurface caused by fluid flow, differences in the two seismic surveys include changes in the overburden along with acquisition discrepancies, which are both prominent and undesirable. The virtual source data, generated after decomposing the wavefield into upgoing and downgoing waves, are independent of both the overburden and acquisition discrepancies, and hence, are useful for time-lapse monitoring (Mehta, et al., 2007d).

The variation of the source signature, however, exists in the virtual source data even after applying wavefield separation. Correlation of the wavefield recorded by a given pair of receivers results in the auto-correlation of the source-time function convolved with the estimated impulse response between the receivers. Theory states that the correlation gather must be deconvolved by the auto-correlation of the source-time function before stacking over the physical sources. Such deconvolution gives the virtual source data independent of the variation of the source signature as well.

The estimation of the source power spectrum, which is the frequency domain representation of the auto-correlation of the source-time function, is possible for relatively short-duration source data. For applications such as earthquakes and drill-bit seismics, the source-time function is long, and hence, difficult to estimate. For such applications, instead of correlation, deconvolution can be used as a seismic interferometric tool. In contrast to correlation, when the two recorded signals are deconvolved the source-time function drops

out, making the resultant interferometric data independent of the source-time function (Snieder and Şafak, 2006; Vasconcelos and Snieder, 2006; Vasconcelos and Snieder, 2007a; Vasconcelos and Snieder, 2007b; Vasconcelos and Snieder, 2007c; Vasconcelos, et al., 2007a; Vasconcelos, et al., 2007b).

Deconvolution interferometry applied to earthquake recording in a borehole is useful for extracting the near-surface properties (Mehta, et al., 2007a). Correlation of the wavefield recorded by a given pair of receivers gives the filtered version of the sum of causal and acausal Green's function. The deconvolved waveforms, instead, represent the elements of the propagator matrix. Apart from extracting the near-surface properties, deconvolution in the form of receiver function applied to borehole data can be used to characterize mode conversion (Mehta, et al., 2007c).

The following publications comprise this dissertation:

Chapter 2:
Mehta, K., Snieder, R., Calvert, R., & Sheiman, J. 2006. Virtual source gathers and attenuation of free-surface multiples using OBC data : implementation issues and a case study. *76th Annual Meeting, SEG, Expanded Abstracts*, 2669-2673.

Mehta, K., Snieder, R., Calvert, R., & Sheiman, J. 2007. Acquisition geometry requirements for generating virtual source data. *The Leading Edge*, In preparation.

Chapter 3:
Mehta, K., Bakulin, A., Sheiman, J., Calvert, R., & Snieder, R. 2007. Improving virtual source method by wavefield separation. *Geophysics*, Accepted.

Chapter 4:
Mehta, K., Sheiman, J., Snieder, R., & Calvert, R. 2007. Virtual source method applied to Mars OBC data for time-lapse monitoring. *Geophysics*, In Revision.

Chapter 5:
Mehta, K., Snieder, R., & Graizer, V. 2007. Extraction of near-surface properties for a lossy layered medium using the propagator matrix. *Geophysical Journal International*, **169**, 271-280.

Mehta, K., Snieder, R., & Graizer, V. 2007. Downhole receiver function: a case study. *Bulletin of Seismological Society of America*, In Revision.

Chapter 2

Implementation issues and challenges in generating a virtual source gather

2.1 Summary

The virtual source method, a technique to image below complex overburden without the knowledge of overburden velocities and near-surface changes, is based on extracting the response between a given pair of receivers by correlating the wavefields recorded by them and stacking over the physical sources. Several issues arise while generating virtual source data, such as the maximum allowable spacing of the physical sources, reflections and multiples from the overburden, and artifacts due to incomplete source aperture. The current chapter addresses these issues using a simple synthetic model and the Mars field ocean bottom cable (OBC) data set.

2.2 Introduction

The virtual source method (Bakulin and Calvert, 2004, 2006; Calvert, et al., 2004) is a technique based on extracting the Green's function that characterizes wave propagation between two receivers, by correlating the wavefields recorded by these receivers. This chapter focuses on implementation issues and challenges involved in generating a virtual source gather. The implementation issues include limitations on the source spacing, reflections and multiples from the overburden, and artifacts resulting from incomplete source aperture.

A virtual source gather is generated by correlating the wavefield recorded by a pair of receivers and stacking over the physical sources (Bakulin and Calvert, 2004, 2006; Calvert, et al., 2004). An important consideration while generating a virtual source gather is the spacing of the physical sources. If the spacing of the sources over which the correlated data (i.e., correlation gather) is stacked is too large, the virtual source data will be spatially aliased. The source spacing cannot exceed a maximum allowed spacing in order to prevent spatial aliasing in the virtual source data. The correlation gather is a useful diagnostic for quality control and assessing the maximum allowable source spacing required to prevent spatial aliasing. In the following section, the dependence of the maximum allowable source spacing on the subsurface and receiver depth is demonstrated using a simple synthetic model.

Other implementation issues, such as the choice of receiver that acts as the virtual source, and the number of sources over which the correlation gather is stacked are demon-
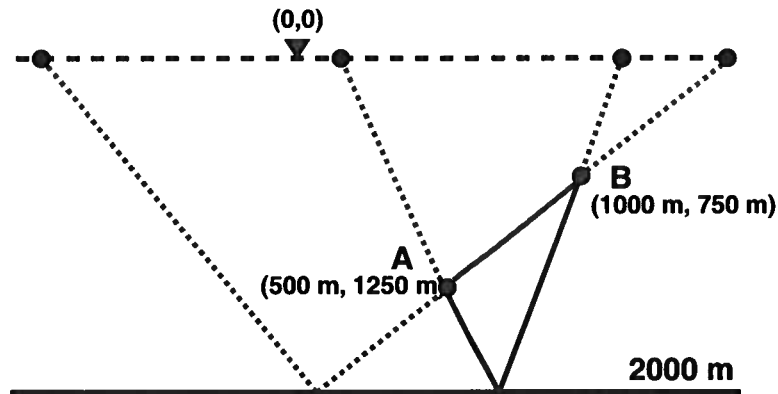
Figure 2.1. Depth section cartoon for a synthetic homogeneous model with two receivers, A and B, located at different depths and a reflector 2 km deep. The four blue circles are the source locations that give stationary phase contribution.

strated using the Mars field OBC data (www.rigzone.com/data/projects). Depending on the receiver chosen to act as the virtual source, different source locations give a stationary phase contribution (Wapenaar, et al., 2005; Snieder, et al., 2006a). The correlation gather is a useful diagnostic for determining the source locations that give the stationary phase contribution. To illustrate the contribution of the sources in the stationary phase region, I generated virtual source gathers with a given receiver as the virtual source but with sources in different subsets of source aperture used for stacking.

The virtual source gathers contain not only undesirable physical arrivals from waves propagating through the overburden but also unphysical arrivals (artifacts) caused by the contribution from the sources at the edges of the source aperture and spurious events due to incomplete source aperture (Snieder, et al., 2006a). These undesirable events are addressed in the final section of the chapter.

2.3   Maximum Allowable Source Spacing

An important consideration for generating a virtual source gather is the maximum allowable source spacing required to prevent spatial aliasing. The dependence of the maximum allowable source spacing on velocity, depth of the receivers, and depth of reflectors is demonstrated through the study of correlation gathers.

Let us start with the simple model shown in figure 2.1. Two receivers, A and B, are placed at different depths, and a reflector is placed at a depth of 2 km. The surface is indicated by the black dashed horizontal line, and the four circles on the dashed line indicate the source locations that give the stationary phase contribution (Wapenaar, et al., 2005; Snieder, et al., 2006a). The model is homogeneous with velocity 1500 m/s. Figure 2.2 shows a correlation gather for this model geometry with sources spaced every 5 m. Each of the traces is the correlation of the reflection response recorded at receivers A and B as
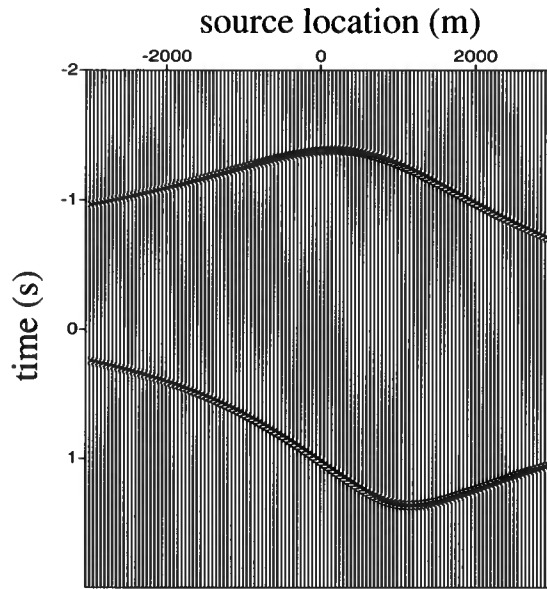
source location (m)

Figure 2.2. Correlation gather showing the reflection response for the model shown in figure 2.1. Sources are spaced every 5 m.

a function of source location. Regions in the vicinity of the extrema of the two reflection events show the source locations that give the stationary phase contribution (Wapenaar, et al., 2005; Snieder, et al., 2006a). The maximum allowable source spacing required to prevent spatial aliasing is related to the maximum slope of the reflection events in these correlation gathers. Larger maximum slope of the reflection events in the correlation gather hence requires smaller source spacing to prevent spatial aliasing in the virtual source data.

Suppose two shots P and Q, separated by offset Δx, are excited on the surface and two receivers, M and N, record the downgoing and upgoing waves respectively at a depth d (figure 2.3(a)). A reflector is present at a depth $d + h$. Figure 2.3(b) is a cartoon of two traces (corresponding to the shots P and Q) of the correlation gather for the receivers M and N. The horizontal axis is offset, and the vertical axis is time. Each of the two traces shows a pulse with arrival time equal to the difference in the traveltime for the waves to propagate from the source to the two receivers. For shot P in figure 2.3(a) the arrival time is given by $\tau_P = [(L_2^P + L_3^P - L_1^P)/v]$, where v is the velocity of the medium and L_2^P, L_3^P, and L_1^P are the propagation distances shown in figure 2.3(a). For a fixed source spacing, the slope of the reflection event in the correlation gather p is proportional to the difference
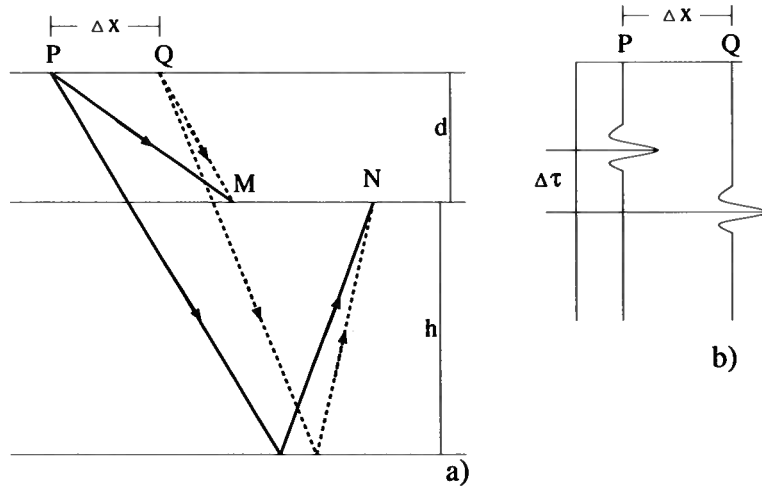
Figure 2.3. Geometry (a) with two sources P and Q on the surface, two receivers M and N at a depth d, and a reflector at a depth $d + h$. The paths of primary propagation from sources P and Q, downgoing to receiver M and upgoing to receiver N are shown by solid and dashed lines respectively. Figure (b) shows two traces (corresponding to the shots P and Q) of the correlation gather for receivers M and N.

in the arrival times for adjacent sources and is given by

$$
\begin{aligned}
p\Delta x &= \Delta \tau \\[2mm]
&= |\tau_P - \tau_Q| \\[2mm]
&= \frac{|(L_2^P + L_3^P - L_1^P) - (L_2^Q + L_3^Q - L_1^Q)|}{v} \\[2mm]
&= \frac{|(L_2^P - L_2^Q) + (L_3^P - L_3^Q) - (L_1^P - L_1^Q)|}{v},
\end{aligned}
\tag{2.1}
$$

where L_2^P, L_2^Q, L_3^P, L_3^Q, L_1^P, and L_1^Q can be expressed in terms of d, h and the angles of incidence and reflection. The maximum slope of the reflection event in the correlation gather hence depends on the velocity of propagation, depth of the receivers (d), depth of the reflector ($d + h$), and the angles of incidence and reflection.

Figure 2.4 depicts correlation gathers and their corresponding f-k spectrum, obtained by Fourier transforming the correlation gather both in space and time. Figure 2.4(a) shows correlation gather with no spatial aliasing. The slope of the reflection event in the correlation gather is denoted by p. Figure 2.4(b) is a cartoon of the corresponding f-k spectrum obtained by taking the Fourier transform both in time and space, with f referring to frequency and k
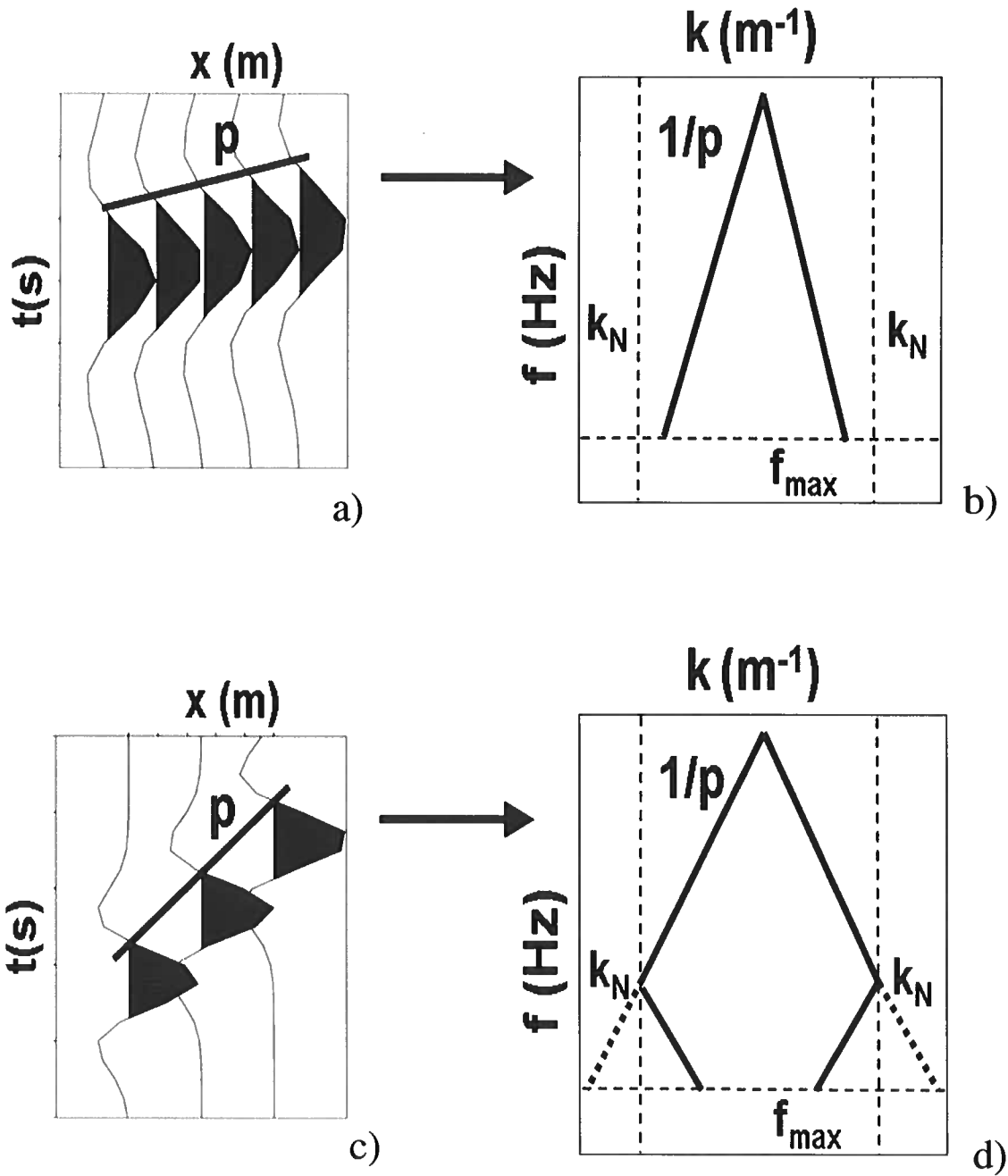
Figure 2.4. (a) is a subset of a correlation gather for the data that are not spatially aliased. (b) is the corresponding f-k spectrum. (c) is a subset of a correlation gather for data that are spatially aliased. (d) is the corresponding f-k spectrum. p is the slope of the reflection event in the correlation gather. f_{max} is the maximum frequency and k_N is the Nyquist wavenumber.

to the wavenumber. The f-k plot is a useful diagnostic for detecting aliasing. The maximum wavenumber is $k_{max} = 1/\Delta x$, where Δx is the source spacing. The Nyquist wavenumber, k_N (Karl, 1989), is the highest wavenumber that can be unambiguously represented by the signal sampled in space, and is equal to half of the maximum wavenumber ($k_N = k_{max}/2$). The f-k plot in figure 2.4(b) has all the wavenumbers within the Nyquist wavenumber range, hence there is no spatial aliasing.

Figure 2.4(c) shows a correlation gather that is spatially aliased and figure 2.4(d) gives the corresponding f-k spectrum. The f-k plot in figure 2.4(d) shows that the wavenumbers are not contained within the Nyquist wavenumber range. The wavenumbers outside the Nyquist range (dashed lines) show up in the f-k plot as a wrap-around (solid lines), indicating spatial aliasing. The relation of maximum frequency, Nyquist wavenumber, and the slope of the spectrum in figures 2.4(b) and 2.4(d) suggest the following condition to prevent spatial aliasing:

$$
\begin{aligned}
&pf_{max} \leq k_N \\
\Rightarrow \quad &pf_{max} \leq \frac{1}{2\Delta x} \\
\Rightarrow \quad &\Delta x \leq \frac{1}{2pf_{max}}.
\end{aligned}
\tag{2.2}
$$

The maximum allowable source spacing to prevent spatial aliasing therefore decreases with increasing maximum frequency and maximum slope of the reflection event in the correlation gather. The maximum slope of the reflection event in the correlation gather [equation (2.1)] depends on the velocity of propagation, depth of the receivers, depth of the reflector, and angles of incidence and reflection.

Let us illustrate the effect of spatial aliasing in the virtual source data. The correlation gather (figure 2.2) stacked horizontally over all the source locations generates a virtual source trace consisting of a reflection event for both causal and acausal times as shown in the right panel of figure 2.5. The causal pulse refers to the signal recorded by the second receiver as if a virtual source at the first receiver is excited at time t=0 and propagates forward in time. The acausal pulse refers to the signal recorded by the first receiver as if a virtual source at the second receiver is excited at time t=0 and propagates backward in time (Petrashen and Nakhamkin, 1973). The left panel of figure 2.5 is the same as figure 2.2. Along with the reflection events, the virtual source trace also shows four low amplitude blips. The low amplitude blips are the contribution of sources near the edges of the source aperture. These edge effects are commonly observed in seismic data processing (Yilmaz, 2001) and can be suppressed by either using a larger source aperture or tapering the correlation gather before stacking. Figure 2.6 shows the correlation gather for the same model (figure 2.1) but with a larger source aperture. The new source aperture is 12000 m instead of 6000 m. Comparison of the horizontal stack in the right panel of figures 2.5 and 2.6 confirms that the edge effects tend to diminish with increase in the source aperture. Wapenaar (1992) states that finite aperture artifacts cannot be removed by extending the aperture unless some taper is applied. In the presence of geometrical spreading and attenuation, however, the edge effects diminish when the source aperture is increased.
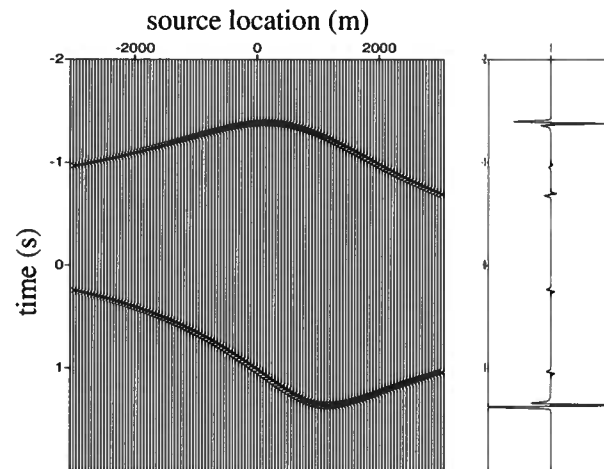
Figure 2.5. Correlation gather showing the reflection response for the model shown in figure 2.1 and horizontal stack on the right. Sources are spaced every 5 m.
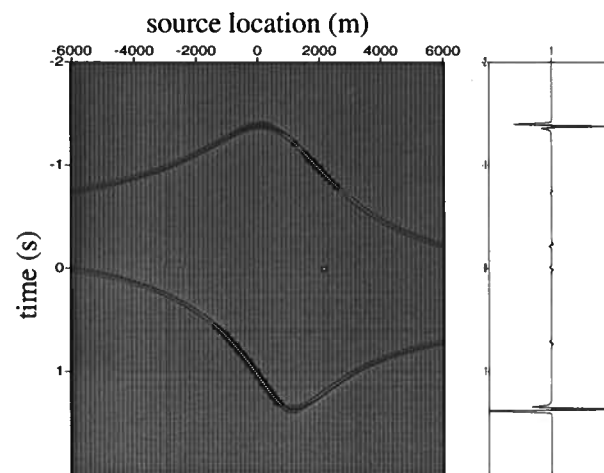
Figure 2.6. Correlation gather showing the reflection response and horizontal stack for the same model (figure 2.1), but with a larger source aperture (12000 m). Sources are spaced every 5 m.
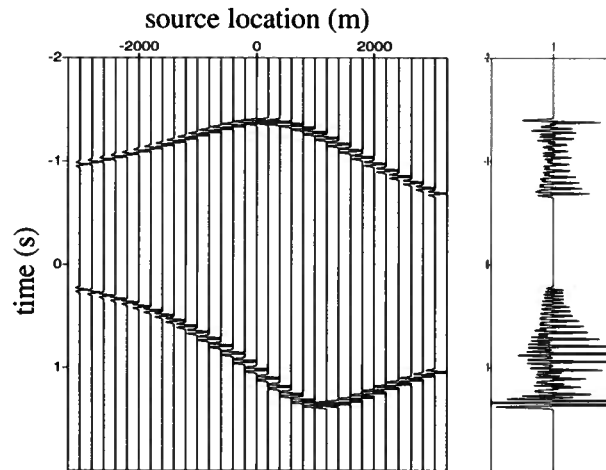
Figure 2.7. Correlation gather showing the reflection response and horizontal stack for the model shown in figure 2.1 with sources spaced every 200 m.

The correlation gathers presented until now had a source spacing of 5 m, and there was no spatial aliasing in the virtual source traces. If, however, the source spacing is increased to 200 m [large enough to violate the inequality in equation (2.2)] for the model of figure 2.1, the resultant correlation gather is shown in the left panel of figure 2.7. Spatial aliasing shows up in the form of ringing in the stack (right panel of figure 2.7).

The following subsection illustrates the dependence of maximum allowable source spacing on the velocity of propagation, depth of the receivers, and depth of the reflector, as given by equation (2.2).

2.3.1   Synthetic Model

Consider a homogeneous model with two receivers at a depth of 90 m, a single reflector at a depth of 2000 m, and velocity 1500 m/s (figure 2.8). The physical sources are fired at the surface. The geometry of the model is chosen to be similar to an OBC acquisition geometry in order to relate to the source spacing for the Mars field (located in the deepwater Gulf of Mexico) OBC data that are used in the second part of the chapter. The depth of the seafloor for the Mars field is 1000 m. To understand the dependence of the maximum allowable source spacing on the depth of the receivers and to relate to the source spacing requirement for the Mars field, the same model with receivers at a depth of 1000 m is considered later in the chapter.

The left panel of figure 2.9 shows the correlation gather for the model in figure 2.8. The horizontal stack of the correlation gather for this model (right panel of figure 2.9) shows two reflection events. The edge effects are negligible because the slope of the reflection event in the correlation gather near the edges is higher than that of the previous model. Bender and

c = 1500 m/s
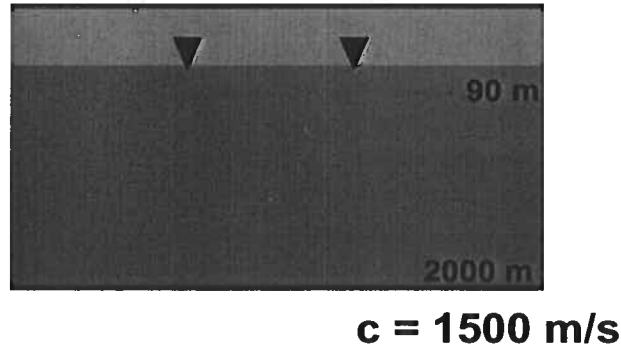
Figure 2.8. Depth section cartoon showing the geometry for the synthetic model.

Orszag (1978) show mathematically that for an oscillating function having non-zero values at the end points the amplitude of the end points is inversely proportional to the derivative of the phase function. The phase function for the virtual source data is the correlation gather.

The source spacing in the correlation gather (left panel in figure 2.9) is 5 m. As discussed in the previous section, the most common way to study aliasing is to Fourier transform the data to the frequency-wavenumber (f-k) domain. A wrap-around in f-k spectrum indicates aliasing. Figure 2.10 shows the f-k spectrum of the correlation gather in left panel of figure 2.9. For source spacing $\Delta x = 5$ m, the maximum wavenumber $k_{max} = 0.2$ m^{-1} ($k_{max} = 1/\Delta x$). The corresponding Nyquist wavenumber k_N is 0.1 m^{-1} ($k_N = k_{max}/2$), which is the limit of the wavenumber axis in figure 2.10. All the wavenumbers are within the Nyquist wavenumber range, indicating no spatial aliasing.

The correlation gather for source spacing of 50 m is shown in the left panel of figure 2.11. The ringing in the horizontal stack (right panel of figure 2.11) indicates that the data are spatially aliased. Figure 2.12 shows the corresponding f-k plot. For source spacing $\Delta x = 50$ m, the maximum wavenumber $k_{max} = 0.02$ m^{-1}. The corresponding Nyquist wavenumber k_N is 0.01 m^{-1}, which is the limit of the wavenumber axis in figure 2.12. The wrap-around in the spectrum indicates the presence of wavenumbers outside the Nyquist wavenumber range indicating that the data are spatially aliased. Hence, the maximum allowable source spacing for this model lies between 5 m and 50 m. A combination of the f-k plot and equations (2.1) and (2.2) can be used to design the maximum allowable source spacing to prevent spatial aliasing in the virtual source data.

Equations (2.1) and (2.2) indicate that the maximum allowable source spacing depends on maximum slope of the reflection event in the correlation gather (p), which in turn depends on the velocity of the medium. According to equation (2.1) the maximum slope of the reflection event in the correlation gather decreases with increasing the velocity. Figure 2.13 shows the correlation gather for velocity of 2000 m/s (instead of 1500 m/s) with the same model (figure 2.8). With the higher velocity, the maximum slope of reflection event [equation
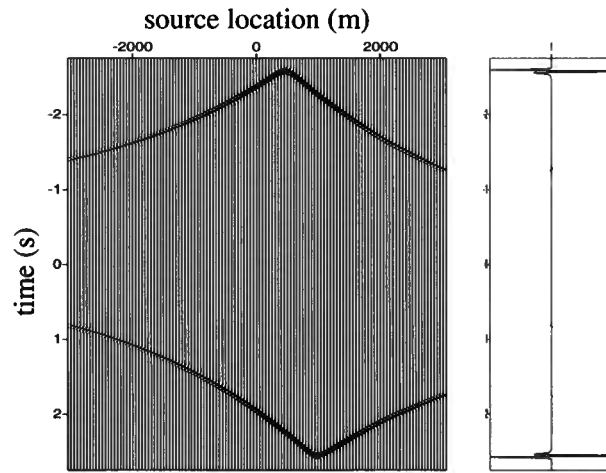
Figure 2.9. Correlation gather showing the reflection response for the model shown in figure 2.8. Sources are spaced every 5 m.


Figure 2.10. Frequency-wavenumber (f-k) plot corresponding to the correlation gather shown in figure 2.9. For source spacing (Δx) of 5 m, the maximum wavenumber k_{max} is 0.2 m^{-1} ($k_{max} = 1/\Delta x$). The corresponding Nyquist wavenumber k_N is 0.1 m^{-1} ($k_N = k_{max}/2$), which is the limit of the wavenumber axis.
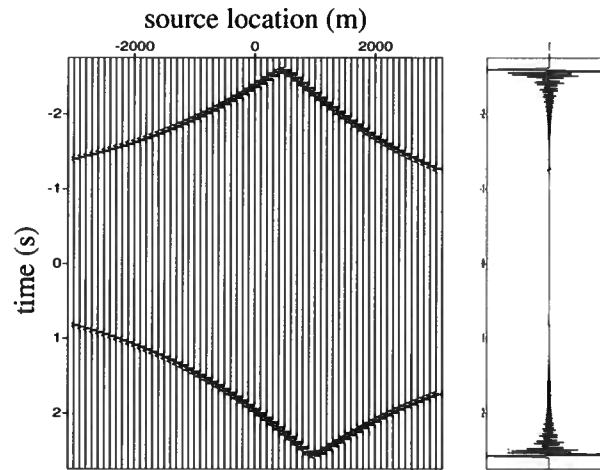
Figure 2.11. Correlation gather showing the reflection response for the model shown in figure 2.8 with sources spaced every 50 m.
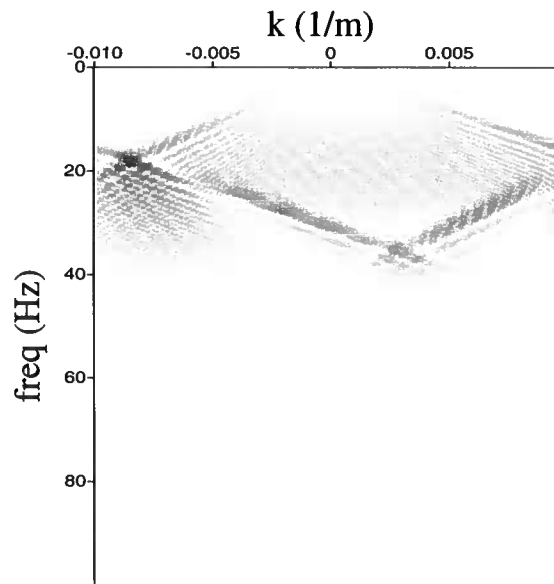
Figure 2.12. Frequency-wavenumber (f-k) plot corresponding to the correlation gather shown in figure 2.11. For source spacing (Δx) of 50 m, the maximum wavenumber k_{max} is 0.02 m^{-1} ($k_{max} = 1/\Delta x$). The corresponding Nyquist wavenumber k_N is 0.01 m^{-1} ($k_N = k_{max}/2$), which is the limit of the wavenumber axis.

Figure 2.13. Correlation gather showing the reflection response and horizontal stack for the model shown in figure 2.8 but with velocity 2000 m/s. Sources are spaced every 5 m.

(2.1)] in this correlation gather is smaller than the maximum slope of the reflection event in the correlation gather in figure 2.9. The reduction in the maximum slope of the reflection event can be physically explained by the decrease in the traveltime difference between the adjacent receivers with increase in the velocity. Hence, the maximum slope of the reflection event in the correlation gather reduces with increasing the velocity, thus allowing a larger source spacing.

The maximum slope of the reflection event in the correlation gather [equation (2.1)] depends on the propagation lengths L_1, L_2 and L_3 (figure 2.3). These propagation lengths depend on the depth of the reflector, making it an important parameter that constraints the maximum allowable source spacing. Figure 2.14 shows the correlation gather for reflector depth of 1000 m (instead of 2000 m). Because of the decrease in the reflector depth, the maximum slope of the reflection event in this correlation gather reduces compared to that of the reflection event in the correlation gather in figure 2.9. As with the velocity increase, the reduction in the maximum slope of the reflection event in the correlation gather due to a decrease in the reflector depth can be physically explained by a decrease in the traveltime difference. The maximum slope of the reflection event in the correlation gather thus increases with increasing the reflector depth, causing the maximum allowable source spacing to decrease. Therefore, the deepest reflector in the subsurface controls the maximum allowable source spacing without introducing spatial aliasing.

The propagation lengths L_1, L_2 and L_3 that control the maximum slope of the reflection event in the correlation gather, also depend on the depth of the receivers [equation (2.1)]. Let us illustrate the dependence of the maximum allowable source spacing on the depth of the receivers. The reflector is 2000 m deep, and the velocity is 1500 m/s. The
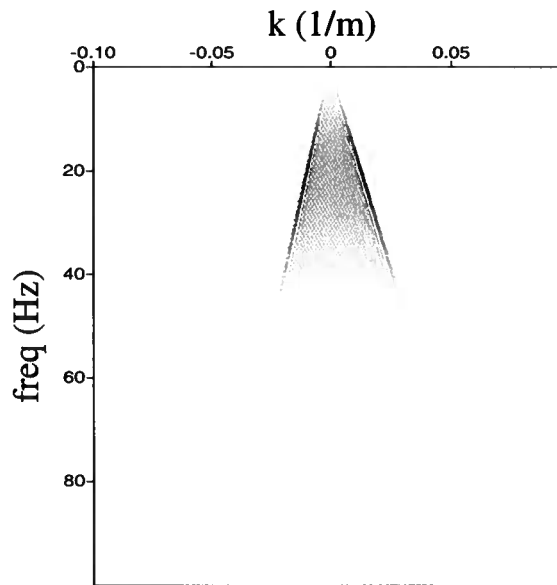
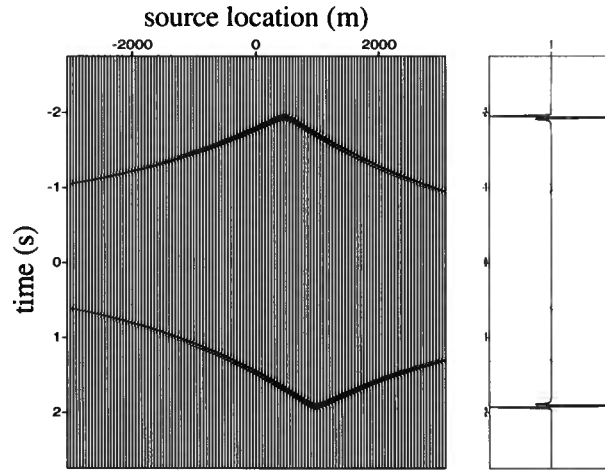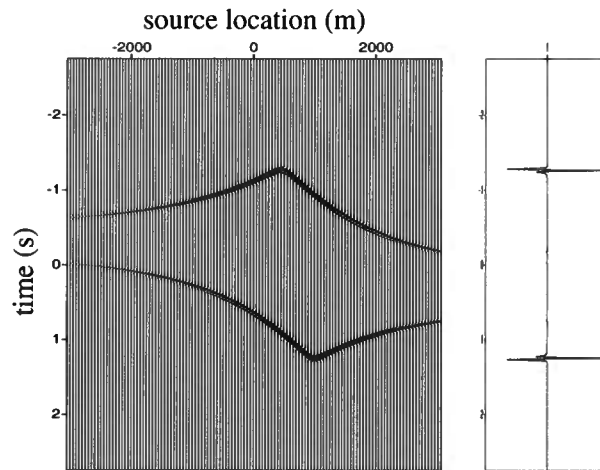Figure 2.14. Correlation gather showing the reflection response and horizontal stack for the model shown in figure 2.8 but with reflector 1 km deep. Sources are spaced every 5 m.

two receivers are, however, placed at a depth of 1000 m. This geometry is similar to that of the Mars field OBC data acquisition. Increasing the depth of the receivers (from 90 m to 1000 m) for a fixed depth of the reflector (2000 m) is analogous to reducing the depth of the reflector therefore leading to a decrease in the maximum slope of the reflection event in the correlation gather [equation (2.1)]. Deeper receivers, therefore, allow a larger source spacing without introducing spatial aliasing.

The correlation gather for this model with 5 m source spacing is shown in the left panel of figure 2.15. The maximum slope of the reflection event in this correlation gather is smaller than that in the correlation gather in the left panel of figure 2.9. The horizontal stack (right panel of figure 2.15) shows the two clean reflections with their edge effects, hence suggesting no spatial aliasing. The edge effects in this case are stronger as compared to that in figure 2.5 because the slope of the reflection event in the correlation gather shown in figure 2.15 is smaller at the end points than that in figure 2.5. When the source spacing is increased to 50 m, the resultant horizontal stack (right panel of figure 2.16) shows weak ringing (around $\pm$ 1 s), suggesting that the data are spatially aliased but not nearly as severely as for the model with receivers 90 m deep. Increasing the depth of the receivers reduced the maximum slope of the reflection event in the correlation gather, thus allowing a larger source spacing without introducing severe spatial aliasing. This suggests that shallower receiver locations results in a larger maximum slope of the reflection event in the correlation gather and thus, requires smaller source spacing to prevent spatial aliasing.

The maximum allowable source spacing, a crucial consideration while designing a virtual source experiment, can be constrained with the help of the f-k spectrum plot and equations (2.1) and (2.2). Summarizing, the maximum allowable source spacing depends on the propagation lengths L_2^P, L_2^Q, L_3^P, L_3^Q, L_1^P, and L_1^Q which in turn depend on the depth
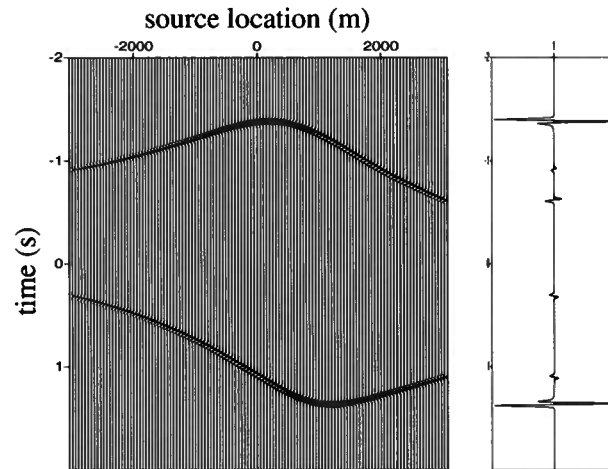
Figure 2.15. Correlation gather and horizontal stack showing the reflection response for the the model shown in figure 2.8 but with receivers 1000 m deep.
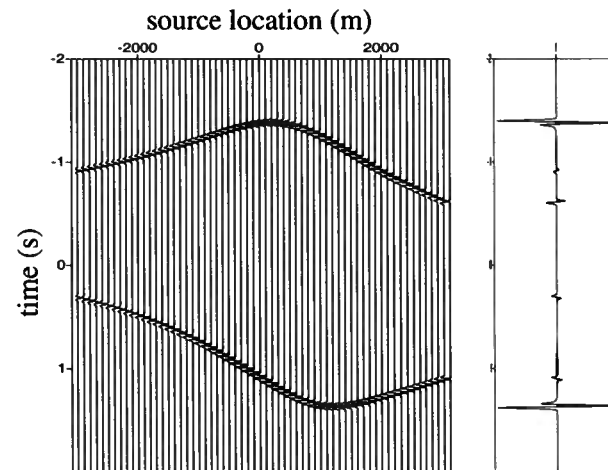
Figure 2.16. Correlation gather and horizontal stack showing the reflection response for the the model shown in figure 2.8 but with receivers 1000 m deep and source spacing 50 m.
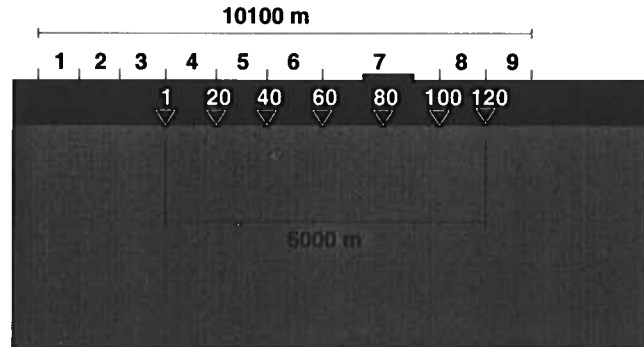
Figure 2.17. Cartoon of the acquisition geometry of the ocean-bottom cable data set obtained from the Mars field. The seafloor is at a depth of 1 km. There are 120 4-C sensors permanently stationed on the seafloor with spacing of 50 m (triangles). A total of 364 shots were fired from the sea-surface every 25 m. The shots are divided into 9 panels, each panel consisting of about 40 shots. The missing shots in panel 7 are indicated by the horizontal bar.

of the receiver, depth of the reflector, velocity of the medium and the angles of incidence and reflection.

A surface seismic experiment requires the receivers to be densely sampled to prevent spatial aliasing that would occur when the data are used for imaging (e.g., Kirchhoff migration). The maximum allowable receiver spacing to prevent spatial aliasing in surface seismic data depends on the subsurface parameters such as the velocity and the deepest reflector. For the virtual source method the receivers are located in the subsurface. The receiver spacing requirements for the virtual source method, however, are similar to that for the surface seismic experiment. In addition to the optimum receiver spacing, for the virtual source method the sources on the surface also requires to be designed as described above to prevent spatial aliasing artifacts in the virtual source data.

Apart from the source spacing and receiver spacing, other implementation issues include the choice of the receiver that acts as the virtual source, the locations of the physical sources used for stacking, and undesirable events resulting from limited acquisition aperture and overburden multiples generated while creating a virtual source gather. These issues are addressed in the following sections.

2.4   Generation of Virtual Source Gathers

A virtual source gather is generated by correlating the wavefield recorded by a reference receiver (virtual source) with that of all the other receivers and stacking the correlation gather over the physical sources. The generation of the virtual source gathers is demonstrated using multi-component ocean-bottom cable data recorded at the Mars field (www.rigzone.com/data/projects). The Mars field is located in the deepwater Gulf of Mexico. Figure 2.17 sketches a model of the acquisition geometry. The geometry consists of 364
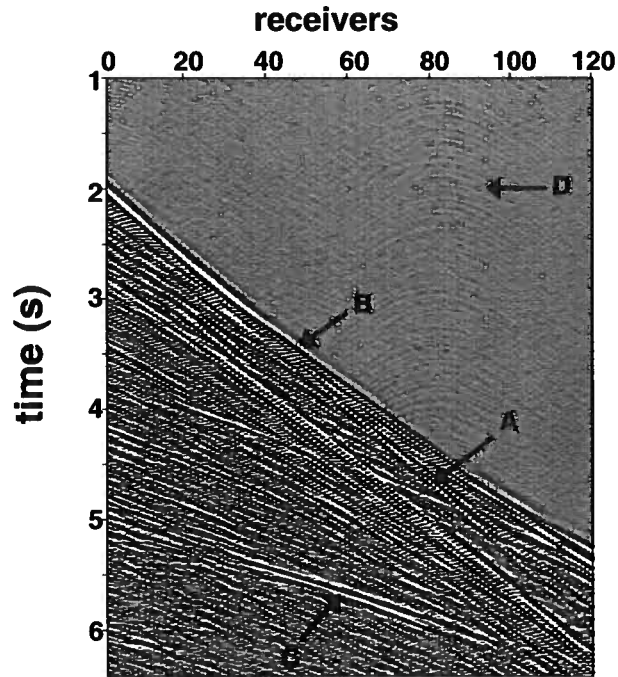
Figure 2.18. A single raw shot gather (hydrophone component) showing direct arrival, refractions, reflections and ship noise that are labeled as A, B, C, and D, respectively.

shots fired (at a spacing of 25 m) on the sea-surface with 120 4-C sensors (spaced every 50 m) permanently stationed on the seafloor about 1 km deep. The source spacing analysis for receivers located at a depth of 1000 m suggests that 25 m source spacing is sufficient to prevent spatial aliasing in the virtual source data for receivers located on the seafloor 1 km deep. As shown in figure 2.17, these 364 shots are divided into nine groups, which I refer to as *panels*. The horizontal bar in shot panel 7 indicates missing shots attributable to the presence of the platform.

Let us concentrate on the hydrophone component (figure 2.18). The shot gather depicts a direct arrival (A) that propagates with the water velocity (1500 m/s), refractions (B) and reflections (C). The group of events marked by D correspond to the noise generated by a service boat. This boat is docked at the platform for prolonged periods while loading and unloading supplies during data acquisition.

Apart from source spacing, another crucial consideration for generating a virtual source is the location of the sources over which the correlation gather is generated and stacked. Stationary phase analysis is useful to diagnose the source locations that give the dominant contribution (Wapenaar, et.al., 2005; Snieder, et.al., 2006a). Figure 2.19 shows, for the hydrophone component, a correlation gather with each trace representing the correlation of the waves recorded by the hydrophone at receiver 1 with the waves recorded by the
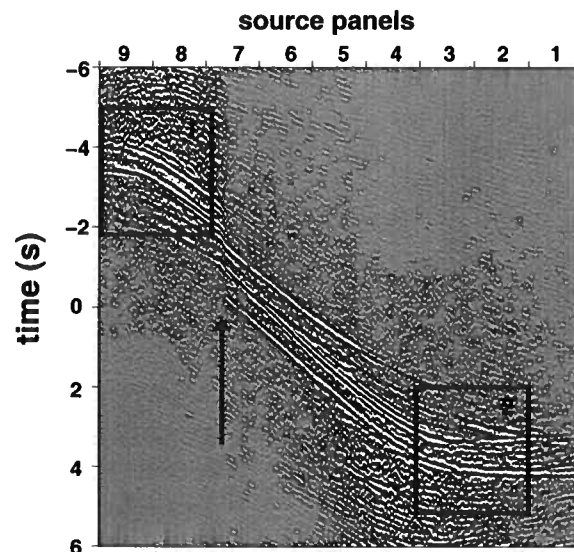
Figure 2.19. Correlation gather generated by correlating the wavefield recorded by the hydrophone in the receiver 1 with the wavefield recorded by the hydrophone in the receiver 120 for all source locations. The horizontal axis corresponds to source location. The extremas indicated by boxes 1 and 2 correspond to the sources giving stationary phase contribution. The arrow points to the discontinuity resulting from the missing shots in source panel 7. In order to increase the signal-to-noise level, it has been low-pass filtered.

hydrophone at receiver 120 as a function of source location. The events in the correlation gather have two extremas, labeled 1 and 2, corresponding to two stationary phase regions. The arrow indicates a discontinuity in the correlation gather that is caused by the missing shots in source panel 7. Low pass filtering (cut-off frequency = 15 Hz) is applied to the correlation gather to increase the signal-to-noise level, as shown in figure 2.19.

This correlation gather would be stacked over all the sources to obtain a trace that represents the wavefield recorded by receiver 120 as if a source was located at the position of receiver 1. Similar virtual source traces can be generated by correlating the wavefield recorded by receiver 1 with the wavefield recorded by every other receivers and stacking over the source locations, to form a virtual source gather with receiver 1 as the virtual source. In the stack, the prominent contribution comes from physical sources located in the stationary region; sources placed at other locations give contributions that interfere destructively. Instead of stacking over all sources, a virtual source gather can also be generated by stacking the correlation gather over sources in a subset of the source aperture that includes the sources giving the stationary phase contribution.

Figure 2.20 shows, for the hydrophone, the virtual source gather with receiver 1 as the virtual source and the correlation gather stacked over the sources in source panel 1. The gather looks similar to a conventional shot gather. A direct arrival (A), a few refractions,

Figure 2.20. Virtual source gather for hydrophone with receiver 1 as the virtual source and source panel 1 used for stacking. The direct arrival is shown by A and a strong reflection shown by B.

and a strong reflection (B) are present in this virtual source gather. Figure 2.19 shows that for t > 0, source panel 3 mostly contain the sources that give stationary phase contribution.

If the correlation gather is stacked over the sources in source panel 3 instead over those in source panel 1, one obtains the virtual source gather shown in figure 2.21. Apart from a few refractions, most of the arrivals are reflections either from the subsurface or from the free-surface. The difference in the virtual source gathers obtained by stacking over the sources in source panel 1 as compared to stacking over the sources in source panel 3 arises because the waves excited by sources in source panel 3 arrive with a different slowness range compared to those from source panel 1.

Virtual source gathers generated by stacking over sources in different source panels can therefore be used to separate waves propagating with different slownesses. This is similar to beam steering or "focused stack" (Poletto and Miranda, 2004; Sheriff, 1999), which emphasizes energy from particular directions. The raw shot gather (figure 2.18) shows the direct arrival, refractions and reflections. In contrast, virtual source gathers generated by stacking over different source panels can be used to separate the reflections from the direct arrival and refractions.

Figure 2.21 shows three strong events occurring at about 1.4, 2.8 and 4.2 s, marked by A, B and C, respectively. These arrivals correspond to the reflections from the free-surface (i.e., free-surface multiples) whose ray paths are shown in figure 2.22. These arrivals, coming

Figure 2.21. Virtual source gather for hydrophone with receiver 1 as the virtual source and source panel 3 used for stacking. The events pointed by the arrow correspond to the free-surface multiples. The artifact caused by the edge effect is highlighted by an ellipse.

from the water layer, are a part of the undesirable overburden response in the virtual source data. The next chapter focuses on the use of wavefield separation applied to the virtual source method to remove such events coming from the overburden.

In figure 2.21 the arrival close to the direct arrival for near offset, highlighted by an ellipse, is an artifact caused by edge effects associated with truncation of the stack over the finite number of shots. The shape of the artifacts introduced by edge effects is diagnosed in the next subsection.

2.4.1 Edge Effect

To illustrate the edge effect in the generation of the virtual source gathers, let us consider the virtual source gather for hydrophone data with receiver 60 as the virtual source (figure 2.23). The correlation gather is stacked over the sources in source panel 5. These sources give the stationary phase contribution. The two thin perpendicular lines mark zero time and the location of the virtual source, respectively. The wavefield for positive times and positive offsets (with respect to receiver 60) is comparable to a conventional shot gather. It consists mainly of the direct arrival, refractions, and a strong reflection (D). Let us identify the events marked by A through E in the virtual source gather.
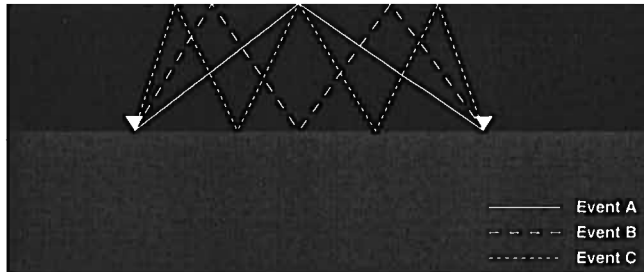
Figure 2.22. Depth section cartoon illustrating the ray paths corresponding to the three free-surface multiples arriving at different times as shown in figure 2.21.
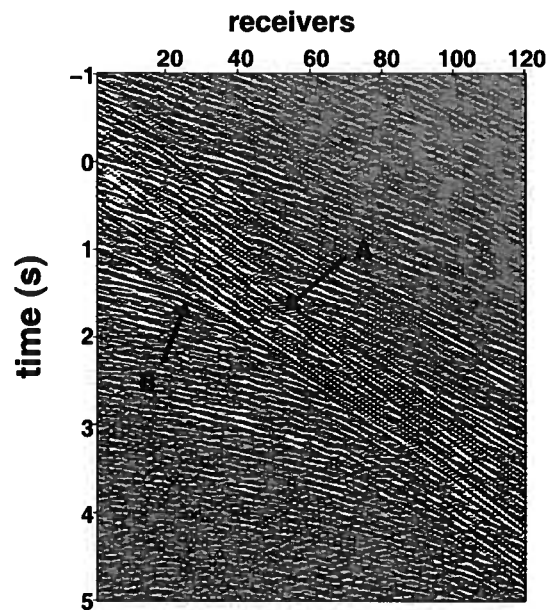

Figure 2.23. Virtual source gather for hydrophone data with receiver 60 as the virtual source and source panel 5 used for stacking. The two perpendicular lines show the zero time and the location of the virtual source. The arrows close to $\pm$ 1.4 s (denoted by D and E) and the dashed line shows the apexes of the free-surface multiples for the causal and acausal responses. Box A indicates the artifact due to waves coming only from one side of the virtual source, which is caused by use of a small source aperture located to the left of the virtual source. Spurious events shown by B are the side-lobes in the auto-correlation. The artifacts from the edges are indicated by C and are highlighted by a dashed line.
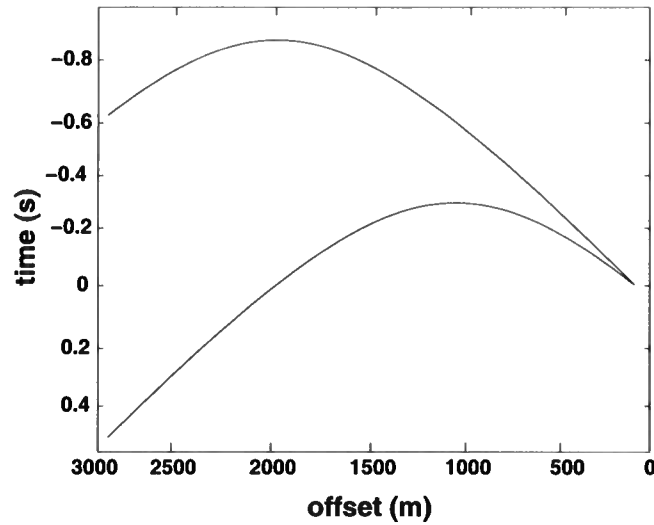
Figure 2.24. Traveltime difference curve (as a function of receiver offset) representing the difference in the traveltime for waves to travel from the source to the receiver 60 and that for waves to travel from the source to receivers 1 through 59 for the the two sources each located at the edge of source panel 5.

- **Box A** shows a group of spurious arrivals that arise because the correlation gather is stacked over a small subset of sources (source panel 5). These spurious events average out by using a larger source aperture such that energy comes from a larger range of directions. If the overburden was complex and heterogeneous instead of the homogeneous water layer, scattered waves come from a larger range of directions, thus creating an effective larger source aperture (Fink, 1993, 1999; Clouet and Fouque, 1997; Borcea, et al., 2002; Borcea, et al., 2003; Parvulescu, 1995; Blomgren, et al., 2002; Mehta and Snieder, 2006; Haider, et al., 2004).

- The weak arrivals marked by **B** have moveout parallel to that of the direct arrival. These arrivals are the side-lobes of the auto-correlation of the source-time function that results from the correlation of the wavefields recorded by the virtual source and the receiver. Let P be the virtual source and Q be the receiver. The correlation of the wavefields recorded by the virtual source and the receiver is given, in the frequency domain, by

$$U(\mathbf{r_P},\mathbf{r_S},\omega)U^*(\mathbf{r_Q},\mathbf{r_S},\omega) \quad = \quad |S(\omega)|^2 G(\mathbf{r_P},\mathbf{r_S},\omega)G^*(\mathbf{r_Q},\mathbf{r_S},\omega), \qquad (2.3)$$

where $S(\omega)$ is the frequency domain representation of the source wavelet, $G(\mathbf{r_P},\mathbf{r_S},\omega)$ is the Green's function for wave propagation from the source to the virtual source P, $G(\mathbf{r_Q},\mathbf{r_S},\omega)$ is the Green's function for wave propagation from the source to the receiver Q and $\mathbf{r_S}$, $\mathbf{r_P}$ and $\mathbf{r_Q}$ are the coordinates of the source, the virtual source P,
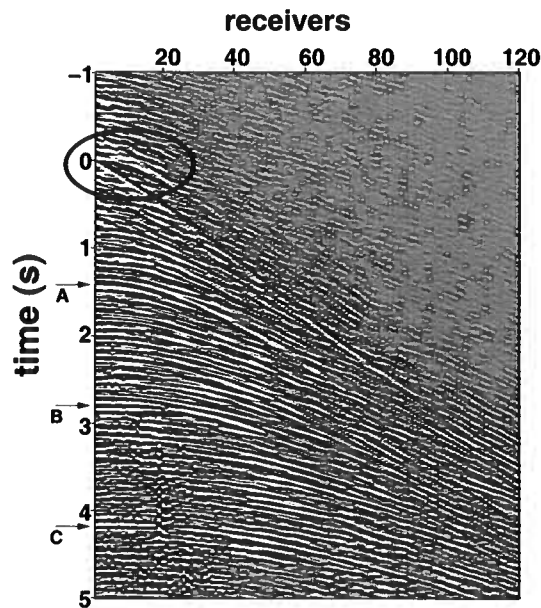
Figure 2.25. Virtual source gather for hydrophone with receiver 60 as the virtual source and source panel 5 used for stacking. The artifacts caused by the edges of the source panel (indicated by C in figure 2.23) agree well with traveltime difference curve.

and the receiver Q, respectively. The power spectrum of the source pulse $|S(\omega)|^2$ corresponds, in time domain, to the auto-correlation of the source-time function whose side-lobes are labeled as B in figure 2.23. These side-lobes can be removed by deconvolving the traces in the correlation gather by the auto-correlation of the source-time function before stacking over the sources. The deconvolution of the correlation gather by the auto-correlation of the source-time function is addressed in chapter 4.

- The direct arrival extends to negative times to give two spurious arrivals shown by C. These are artifacts attributable to truncation of the stack over the sources. These arrivals are extended by dashed thin lines to highlight the shape of the artifact with increasing offset. A useful tool to diagnose the shape of the artifact is the traveltime difference curves (figure 2.24) representing the difference in traveltime for waves traveling from the two sources (each at the two ends of source panel 5) to receiver 60 and in that for waves traveling from the same sources to the receivers 1 through 59, using the water velocity as 1500 m/s. Figure 2.25 shows that the traveltime difference curve agrees well with the kinematics of the edge effect artifact and, hence, is a good diagnostic for estimating the shape of that artifact. A simple way to suppress the

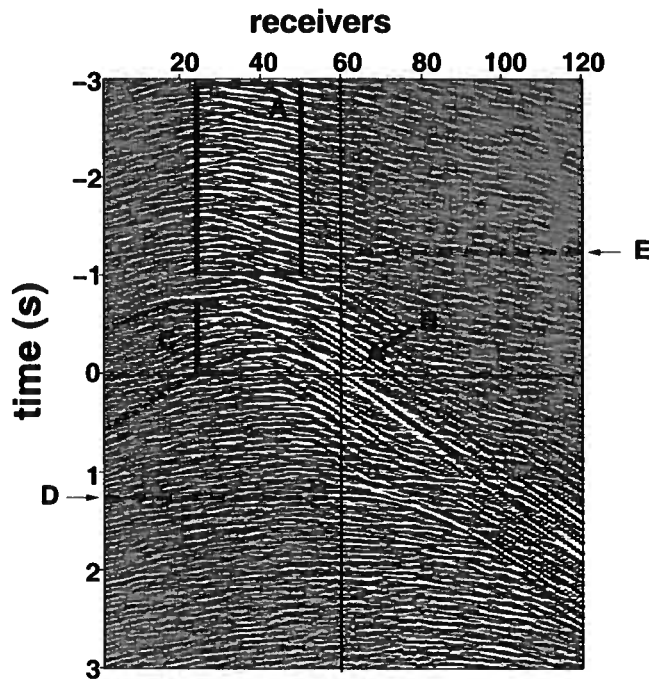Figure 2.26. Virtual source gather for hydrophone with receiver 60 as the virtual source and source panel 5 used for stacking. Linear tapering is applied to the end traces in the correlation gather to attenuate the edge effect artifacts (indicated by C in figure 2.23).

edge effect is to taper the correlation gather or stack the correlation gather over a larger source aperture. Figure 2.26 shows the virtual source gather after applying a linear taper to the last 15 traces on each side in the correlation gather prior to stacking. Application of the taper to the correlation gather has suppressed the edge effect labeled as C.

- Similar to the strong reflection (**D**) at 1.4 s is also a reflection (**E**) at -1.4 s. Figure 2.27 shows two cartoons of the ray paths corresponding to the two reflection events (D and E). The acausal reflection event for negative times (E) is present because downgoing waves that arrive at a receiver to the left of receiver 60 are reflected and then arrive at receiver 60 (figure 2.27(a)). In contrast, the reflection event for positive times (D) occurs because downgoing waves that arrive at receiver 60 are reflected and then arrive at a receiver to the right of receiver 60 (figure 2.27(b)). Both reflection events are incomplete in either offsets because energy is coming from only the sources in source panel 5.

If, instead of stacking over sources in source panel 5, all the sources are used for stacking, the resulting virtual source gather is shown in figure 2.28. The waves forming an
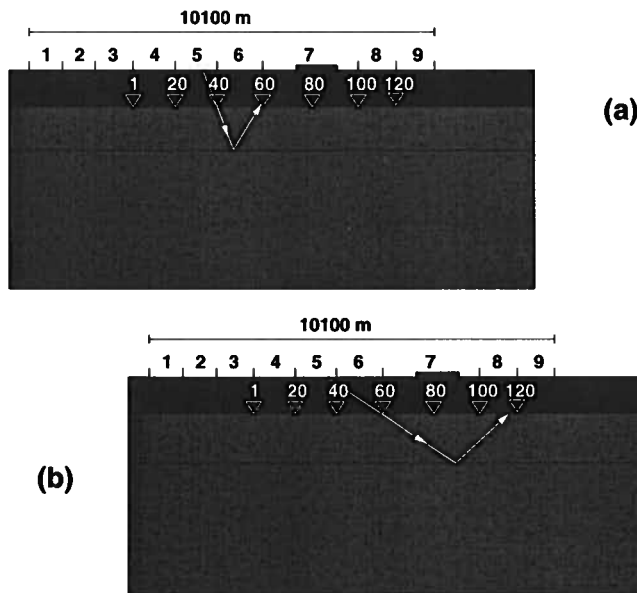
Figure 2.27. Depth section cartoon showing the arrivals that causes the two reflection events D and E shown in figure 2.23. Figure (a) shows the arrival leading to the acausal reflection event (E) and figure (b) shows the arrival leading to the causal reflection (D).

"X" shape, with the two events intersecting at time t=0, correspond to the direct arrivals for both negative and positive offsets (with respect to receiver 60) and times. The free-surface multiples (D and E in figure 2.23) with apexes at ± 1.4 s, are now present for both the negative and positive offsets and times. Artifacts A and C (figure 2.23) are also suppressed because a larger source aperture is used.

Figure 2.29 shows that application of similar tapering to the correlation gather for virtual source gather with receiver 1 as the virtual source leads to suppression of the edge effect that was highlighted with an ellipse in figure 2.21.

The arrow in figure 2.19 indicates the location of the missing shots in source panel 7. A stack over the sources in this panel would give edge effects not only from sources located at the ends of the source aperture but also those from the discontinuity caused by the missing shots. Hence, it is essential to apply tapering to traces close to such discontinuities, along with the traces at the ends of the source aperture.

2.4.2   Spurious Events

Apart from the artifacts caused by sources at the edges of the source aperture, virtual source gathers also contain undesirable arrivals due to incomplete source aperture (unphysical events) and waves propagating through the overburden (physical events). Figure 2.30 shows a three-layer model to illustrate the effect of incomplete source aperture and reflections coming from the overburden and the free-surface. In all the subfigures, the red triangle
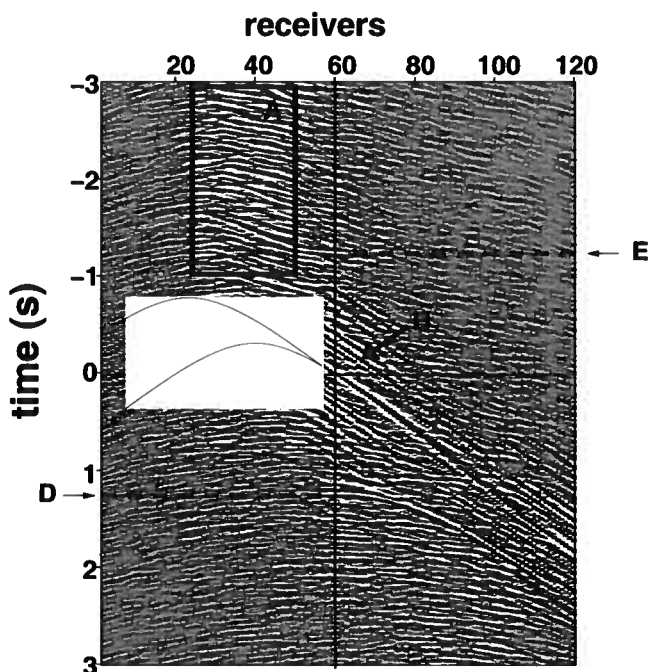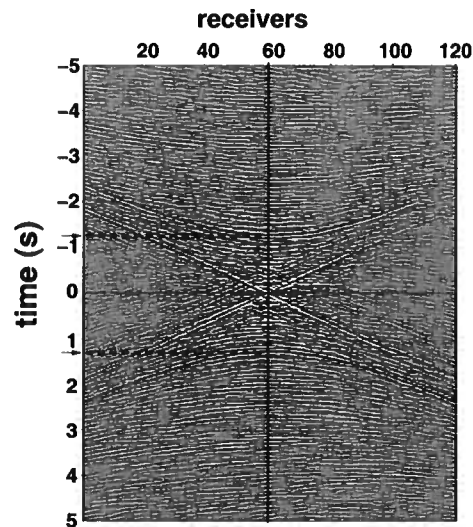
Figure 2.28. Virtual source gather for hydrophone with receiver 60 as the virtual source with all source panels used for stacking. Linear tapering is applied to the end traces in the correlation gather to attenuate the artifacts caused by edge effects. In addition to the direct arrivals, reflection events (shown by the arrows) are clear for both the causal and acausal responses.
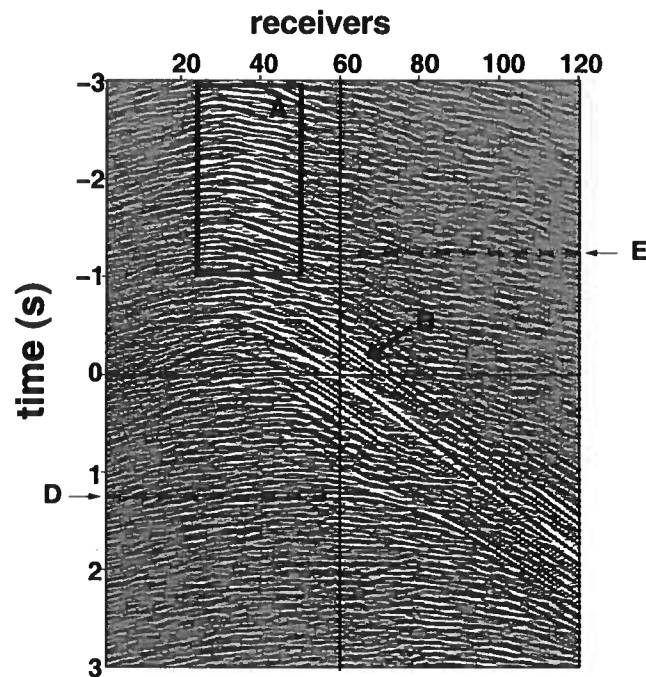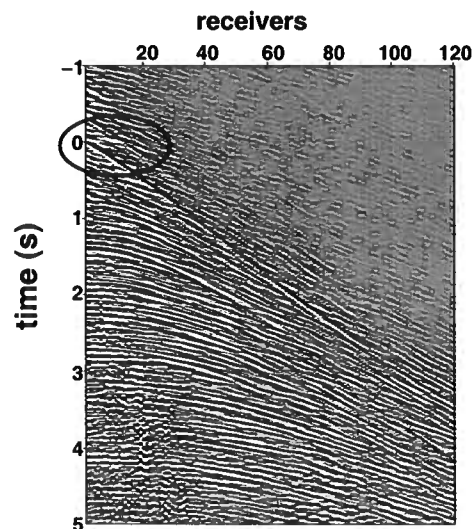

Figure 2.29. Virtual source gather for hydrophone with receiver 1 as the virtual source and source panel 3 used for stacking. Linear tapering is applied at the end traces of the correlation gather to attenuate the edge effect artifacts. The result of tapering is shown by the ellipse as compared to the region highlighted by the ellipse in figure 2.21.
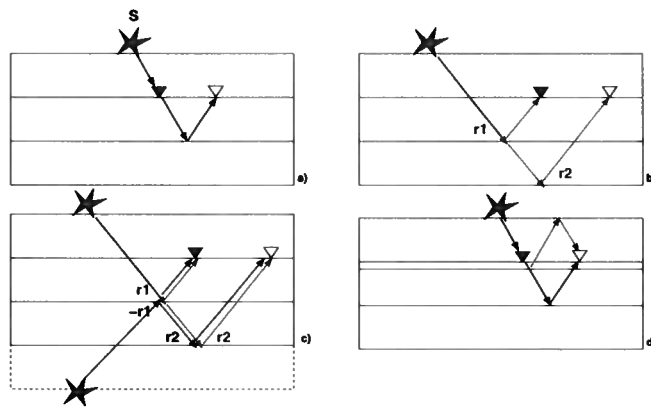
Figure 2.30. Depth section cartoons explaining the need for wavefield separation. 'S' is the source and r1 and r2 are the reflection coefficients at the interfaces. Figure (a) shows the source location that gives the stationary phase contribution for a physical arrival between the virtual source and the receiver. Figure (b) shows the source location that gives stationary phase contribution for a non-physical arrival between the virtual source and the receiver. Figure (c) shows the hypothetical source below the receivers, which if present, would cancel the effect of the non-physical arrival. Figure (d) shows the presence of reflections from the overburden and the free surface multiples.

is the virtual source and the yellow triangle is the receiver. They are both located at depth and physical sources are excited at the surface. Figure 2.30(a) shows the source location along the surface that gives the stationary phase contribution (Wapenaar, et al., 2005; Snieder, et al., 2006a) for a physical arrival between the virtual source and the receivers as shown by the black arrows. By constructive interference of the contributions from all other sources, only this source contributes to the true response between the virtual source and the receiver.

For the source location in figure 2.30(b), the virtual source and the receiver will record the wavefield propagating along the red arrows. Snieder, et al. (2006a) explain that even though the source gives a stationary phase contribution, correlation of the two wavefields does not correspond to any physical arrival between the receivers; hence this source does not contribute to the true response. Such arrivals contribute to spurious events in the virtual source gather. Snieder, et al. (2006a) also show that if a source were placed below the receivers, as shown in figure 2.30(c), the waves propagating along the blue arrows would cancel the contribution of the waves propagating along the red arrows; hence the spurious event would not be a part of the response. In geophysical applications, however, it is impractical to put a source in the subsurface as shown in the cartoon. These unphysical spurious events are, therefore unavoidably present in the virtual source gathers.

Along with the spurious events caused by incomplete source aperture, reflections from the overburden and the free-surface are also a part of the virtual source data (red arrows in figure 2.30(d)). These correspond to undesirable physical arrivals and would also be a part

of the response if a physical source was excited at the virtual source location.

The next chapter demonstrates the use of wavefield separation applied to the virtual source method to overcome some of these implementation issues and suppress the artifacts generated while creating a virtual source gather.

Chapter 3

The virtual source method applied to the Mars field OBC data for time-lapse monitoring

3.1 Summary

The virtual source method requires surface shooting recorded by subsurface receivers placed below the distorting or changing part of the overburden. Redatuming the recorded response to the receiver locations allow the reconstruction of a complete downhole survey as if the sources were also buried at the receiver locations. The ability to redatum the data independent of the knowledge of time-varying overburden velocities makes the virtual source method a valuable tool for time-lapse monitoring. The virtual source method is applied to the Mars field OBC data acquired in the deepwater Gulf of Mexico with 120 multi-component sensors permanently placed on the seafloor. Applying to the virtual source method, a combination of up-down wavefield separation and deconvolution of the correlation gather by the source power spectrum suppresses the influences of changes in the overburden (sea water), thus strengthening the virtual source method for time-lapse monitoring.

3.2 Introduction

Apart from imaging below a complex overburden, the virtual source method is a useful tool for time-lapse monitoring provided that the receivers are placed permanently below the time varying overburden. Time-lapse monitoring is a powerful tool for tracking changes in the subsurface. These changes include geomechanical phenomena associated with the migration of fluids. Conventionally, the changes can be tracked by observing the differences between data from the two seismic surveys obtained over the surveillance period. Apart from changes in the subsurface caused by fluid flow, the difference in the two seismic surveys include variations in the overburden along with the acquisition discrepancies, which are both prominent and undesirable.

The virtual source method is advantageous over the conventional seismic method for time-lapse monitoring at the Mars field (figure 2.17) because with virtual sources generated at each permanently placed receiver location the virtual source gathers obtained are independent of the variation in the overburden as well as acquisition discrepancies for the two surveys. The following section addresses the causes of non-repeatability in the overburden and reasons for using the virtual source method for time-lapse monitoring. The rest of the chapter demonstrates the usefulness of the virtual source method for time-lapse monitoring,

after incorporating wavefield separation and deconvolution of the correlation gather by the source power spectrum.

3.3   Why Virtual Source Method?

Time-lapse seismic monitoring is a useful tool for tracking changes in the subsurface associated with reservoir production. Along with the changes in the data at the reservoir level are prominent undesirable changes in the overburden that mask the changes of interest in the reservoir that one seeks to monitor. For the Mars field, the overburden consists of sea water. The variations in the overburden, therefore, include changes in sea water level, sea surface roughness, sea water temperature and salinity. Redatuming of the data down to the receiver locations using virtual source method makes the survey independent of these variations in the sea water. Other causes of non-repeatability include acquisition discrepancies such as variations in the source location and the source power spectrum. Source power spectrum varies not only for the two surveys but also for each shot location [equation (2.3)]. The virtual source data is, however, independent of the phase spectrum of the source-time function. The power spectrum of the source pulse may differ for different shots as well as for different surveys. In order to remove the effect of varying source power spectrum, the correlation gather is deconvolved by the power spectrum of the source wavelet.

3.4   Conventional Seismic Imaging

Mars field OBC data for the baseline survey was acquired in October-November 2004. The repeat survey was carried out in June 2005. Conventional seismic data refers to the wavefield excited by sources on the sea surface and recorded by the permanently placed sensors on the seafloor. To allow comparison with the seismic images generated after migrating the virtual source data, the conventional seismic data are downward continued to the seafloor using the water velocity. The virtual source method is not applied. The refocused conventional seismic data is migrated, for the years 2004 and 2005 separately, using prestack Kirchoff depth migration. The depth images are then converted to time images (figures 3.1(a) and 3.1(b)) using the Mars field velocity model generated by migration velocity analysis performed on the conventional seismic data. The time t=0 denotes the seafloor level. The gap just below the seafloor is due to blanking applied to the image gathers in order to mute data for which the opening angle at the reflection at large.

Figure 3.1(c) is the difference of the two images. This difference is obtained after locally time-aligning these images to account for any geomechanical changes in the subsurface and to separate changes within the reservoir from its gross movement. There were no production-related subsurface changes between the two surveys over the surveillance period. Therefore the differences [figure 3.1(c)] are mainly due to variations in the overburden and to acquisition discrepancies. After being refocused by the virtual source method at the seafloor, the waves propagate not only through the subsurface [solid rays in figure 3.2(a)], but also through the sea water (dashed rays in figure 3.2(a)). The causes of non-repeatability in the overburden (sea water) include variation in the sea water level, sea
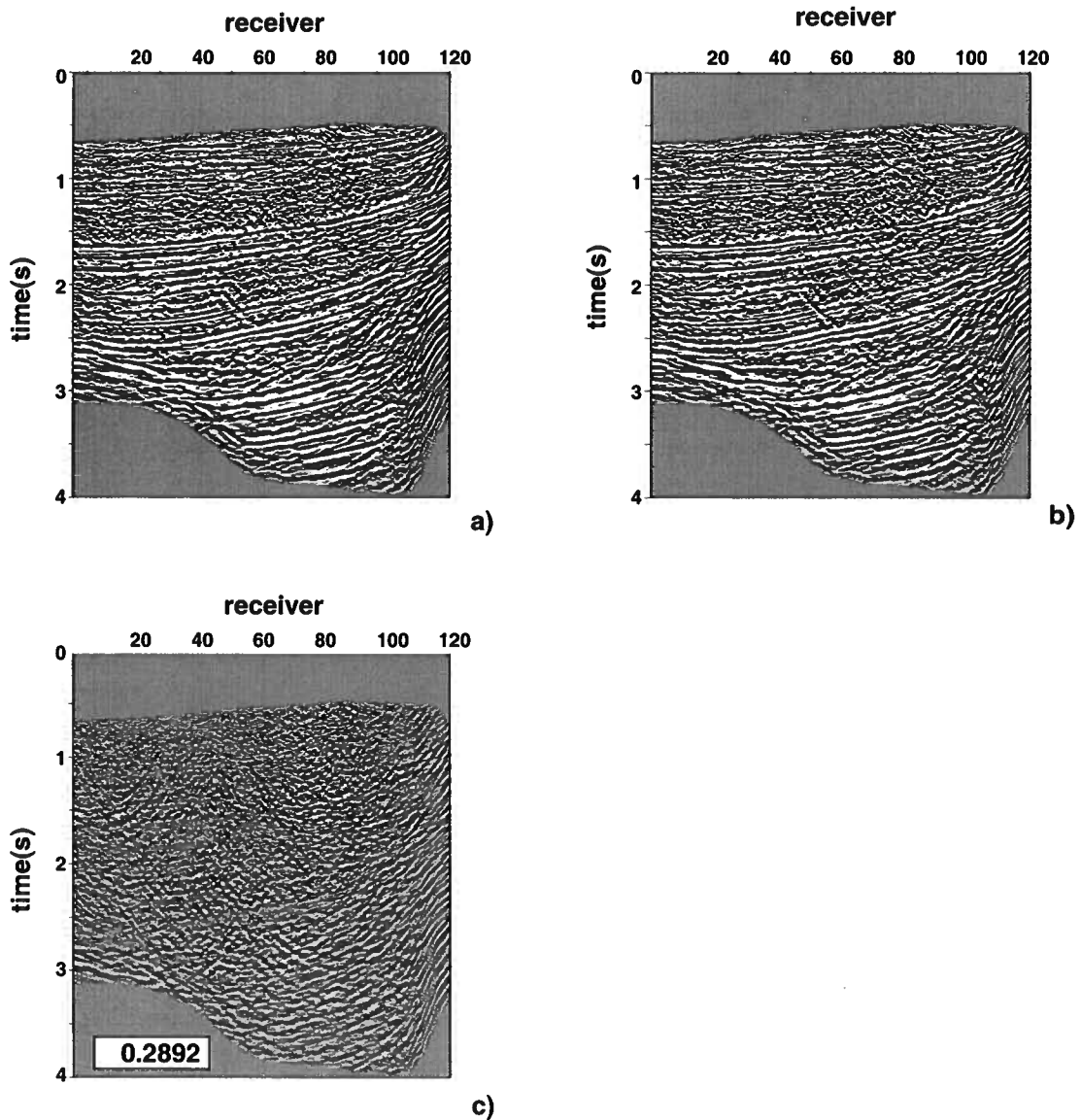
Figure 3.1. Images generated by migrating the conventional seismic data. Figure (a) is the image for the year 2004. Figure (b) is the image for the year 2005. Figure (c) is the difference of the two images, after time alignment, obtained on the same grey scale as figures (a) and (b). The NRMS value is shown in the box in figure (c).
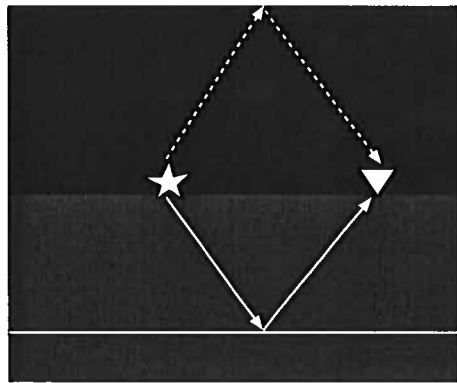
a)
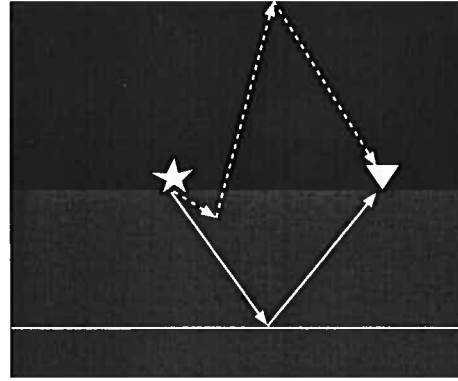
b)
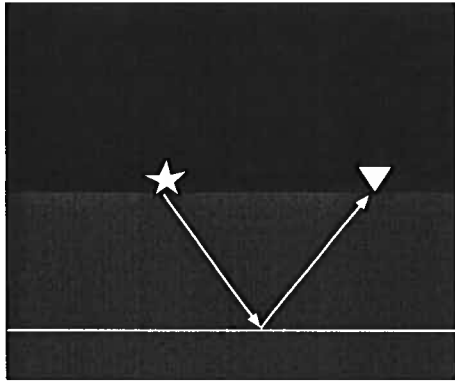
c)
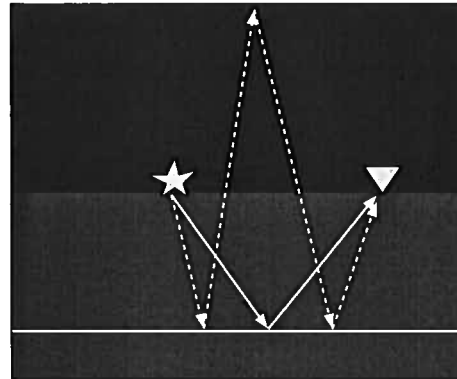
d)

Figure 3.2. Cartoon of the ray paths corresponding to (a) conventional seismic data and virtual source data generated by correlating the total wavefield at the virtual source with the total wavefield at the receivers, (b) virtual source data generated by correlating the direct arrival time-windowed in the total wavefield at the virtual source with the total wavefield at the receivers, (c) data generated by correlating the downgoing waves at the virtual source with the upgoing waves at the receivers. Figure (d) is the cartoon of the ray paths of the multiple that propagates through the overburden even after applying wavefield separation to the virtual source method.

Table 3.1. Comparison of the NRMS values for different seismic images. 'Tot:tot' refers to the virtual source data generated by correlating total wavefield at the virtual source with the total wavefield at the receivers. 'Dir' refers to the direct arrival time-windowed in the total wavefield. 'Down' refers to the downgoing waves. 'up' refers to the upgoing waves. 'Down-dir' refers to the direct arrival time-windowed in the down-going waves. 'decon' refers to the deconvolution of the correlation gather by the source power spectrum. The corresponding figure number is mentioned in the second column.

Seismic image	Figure number	NRMS
Conventional seismic	3.1	0.2892
Tot:tot	3.3	0.3493
Dir:tot	3.4	0.3346
Down:up	3.5	0.2676
Down-dir:up	3.6	0.1770
Down:up:decon	3.8	0.1624
Down-dir:up:decon	3.9	0.1414

surface roughness, sea water temperature and salinity. Apart from the variation in the overburden, non-repeatability is also caused by acquisition discrepancies that include variation in the source location and source power spectrum. Variations in the overburden and acquisition contribute to the prominent undesirable differences observed in figure 3.1(c).

The repeatability is quantified using normalized root mean square amplitude (NRMS) of the difference of the images for the years 2004 and 2005. The NRMS of the difference is defined as

$$NRMS = \sqrt{\frac{< (M - B)^2 >}{< (M^2 + B^2)/2 >}},$$

where 'B' represents the base survey (2004) and 'M' represents the monitor survey (2005). The symbols '<>' represents the average value over the region where NRMS is calculated. Decrease in the value of NRMS indicates improvement in the repeatability.

The NRMS is calculated for the entire seismic image. For the refocused conventional seismic data, the NRMS value is 0.2892. Table 3.1 shows the NRMS of the difference for the conventional seismic image as well as for the virtual source seismic images that will be discussed in the following sections.

3.5   The Virtual Source Method

To generate the virtual source seismic image, different virtual source gathers are generated with every receiver as the virtual source, and instead of migrating the refocused conventional seismic data, the virtual source data generated for the years 2004 and 2005 are migrated using prestack Kirchoff depth migration. The depth image is then converted to a time image using the Mars field velocity model generated by migration velocity analysis on the conventional seismic data.

The simplest approach to generate a virtual source gather is to correlate the total wavefield at the virtual source with the total wavefield at the receivers (Mehta, et al., 2006). The images for the years 2004 and 2005 obtained by migrating virtual source data generated using this simplest approach are shown in figures 3.3(a) and 3.3(b), respectively. The response is dominated by the free-surface multiple because the total wavefields are used, at both the virtual source and the receivers, for correlation. Figure 3.3(c) is the difference of the two images after local time-alignment. In order to highlight the features, the difference image is amplified by a factor of 10 in figure 3.3(d). The differences can be attributed to the waves propagating through the overburden [dashed rays in figure 3.2(a)], which change between the two years because of the variations in the sea water level, sea surface roughness, sea water temperature and salinity. The acquisition discrepancies associated with changes in location of the source between the two years is, however, removed. The variation caused by differences in the source power spectrum [eq. (2.3)], nevertheless, still exists.

The NRMS of the difference for the virtual source data generated by the simplest approach is 0.3493. This value is higher than the NRMS for the conventional seismic image because the pre-processing of conventional seismic data included suppression of the free-surface multiples. In contrast, the virtual source data generated using the simplest approach has the multiples that propagate through the time-varying overburden.

The images generated by the virtual source data [figure 3.3(a)] have lower frequency content than that of the conventional seismic images [figure 3.1(a)]. The difference in frequency content is caused by the receivers and shots being placed along a line whereas the wave-propagation is three dimensional. Snieder, et al. (2006a) show that for such a geometry, the virtual source data need to be multiplied by a factor of $\sqrt{i\omega}$ (ω is the angular frequency), thus restoring the true frequency content. The pre-processing on the raw data involved band-limited spike deconvolution. In the virtual source data, the deconvolution of the correlation gather by the power spectrum of the source wavelet gives a zero-phase band-limited source pulse. Due to this discrepancy, the source-time function for the virtual source data multiplied by $\sqrt{i\omega}$ has a different frequency content compared to that of the conventional seismic data. The discrepancy between the frequency contents of the virtual source data and the conventional seismic data will, therefore, exist even after multiplying the virtual source data with the $\sqrt{i\omega}$ term. Hence, for the virtual source images that follows, we don't apply the $\sqrt{i\omega}$ term.

Figure 3.3. Images generated by migrating the virtual source data. Virtual source gathers are generated by correlating the total wavefield at the virtual source with the total wavefield at the receivers. Figure (a) is the image for the year 2004. Figure (b) is the image for the year 2005. Figure (c) is the difference of the two images, after time alignment, obtained on the same grey scale as figures (a) and (b). Figure (d) is the difference of the image amplified by a factor of 10, on the same grey scale as figures (a) and (b). The NRMS value is shown in the box in figure (d).

3.6   Wavefield Separation

The free-surface multiple are the response from the overburden and hence, are undesirable. They contaminate Figures 3.3(a) and 3.3(b) because we correlate the total wavefield at the virtual source with the total wavefield at the receivers, both of which contain those multiples. The dominant event is a simple reflection from the sea surface and are mainly down-going waves. If, instead of correlating the total wavefields, the down-going waves at the virtual source are correlated with the up-going waves at the receivers, the free-surface multiple along with other overburden reflections can be suppressed (Mehta, et al., 2007b).

Before the wavefield is separated into upgoing and downgoing waves, let us consider the image generated by migrating the virtual source data produced by the current practice. That approach in generating virtual source gather involves correlating the direct arrival time-windowed in the total wavefield at the virtual source with the total wavefield at the receivers (Bakulin and Calvert, 2004, 2006; Calvert, et al., 2004). The images for the years 2004 and 2005 obtained by migrating virtual source data, generated in that way are shown in figures 3.4(a) and 3.4(b), respectively. The free-surface multiple still dominates because instead of using only the upgoing waves at the receiver, the total wavefield is used for correlation. Figure 3.4(c) is the difference of the images for the years 2004 and 2005 and Figure 3.4(d) is the difference image amplified by a factor of 10. Even with windowing the direct arrival for the virtual source data the waves still have propagated upward through the overburden after reflecting from the near-seafloor [dashed rays in figure 3.2(b)]; hence, discrepancies associated with changes between the two years in sea water level, sea surface roughness, sea water temperature, salinity and source power spectrum still exist.

The NRMS of the difference for the virtual source images generated by this approach is 0.3346. Similar to the simplest approach, this value is higher than the NRMS for the conventional seismic image because the pre-processing of conventional seismic data included suppression of the multiples. In contrast, the virtual source data generated by simply windowing the direct arrival at the virtual source still have some multiples propagating through the time-varying overburden.

In order to make the virtual source data independent of the overburden, following the approach by Mehta, et al., 2007b, the virtual source gathers are generated by correlating the downgoing waves at the virtual source with the upgoing waves at the receivers. Figure 3.5(a) and 3.5(b) are the images for the years 2004 and 2005, respectively, obtained by migrating virtual source data generated after wavefield separation into upgoing and downgoing waves. Because the free-surface multiple, after reflecting from the free-surface, is dominantly downgoing waves, correlation of downgoing waves at the virtual source with the upgoing waves at the receivers suppresses the free-surface multiple and highlights, for example reservoir events at around 3.5 s. The difference of the images [figure 3.5(c)] for the years 2004 and 2005, amplified in figure 3.5(d), is less noisy compared to the differences in figures 3.4(d) and 3.3(d).

The NRMS of the difference image after up-down wavefield separation reduced to 0.2676 (Table 3.1). The improved match in results for the two years compared to that for the simplest approach and use of just the windowed direct arrival at the virtual source
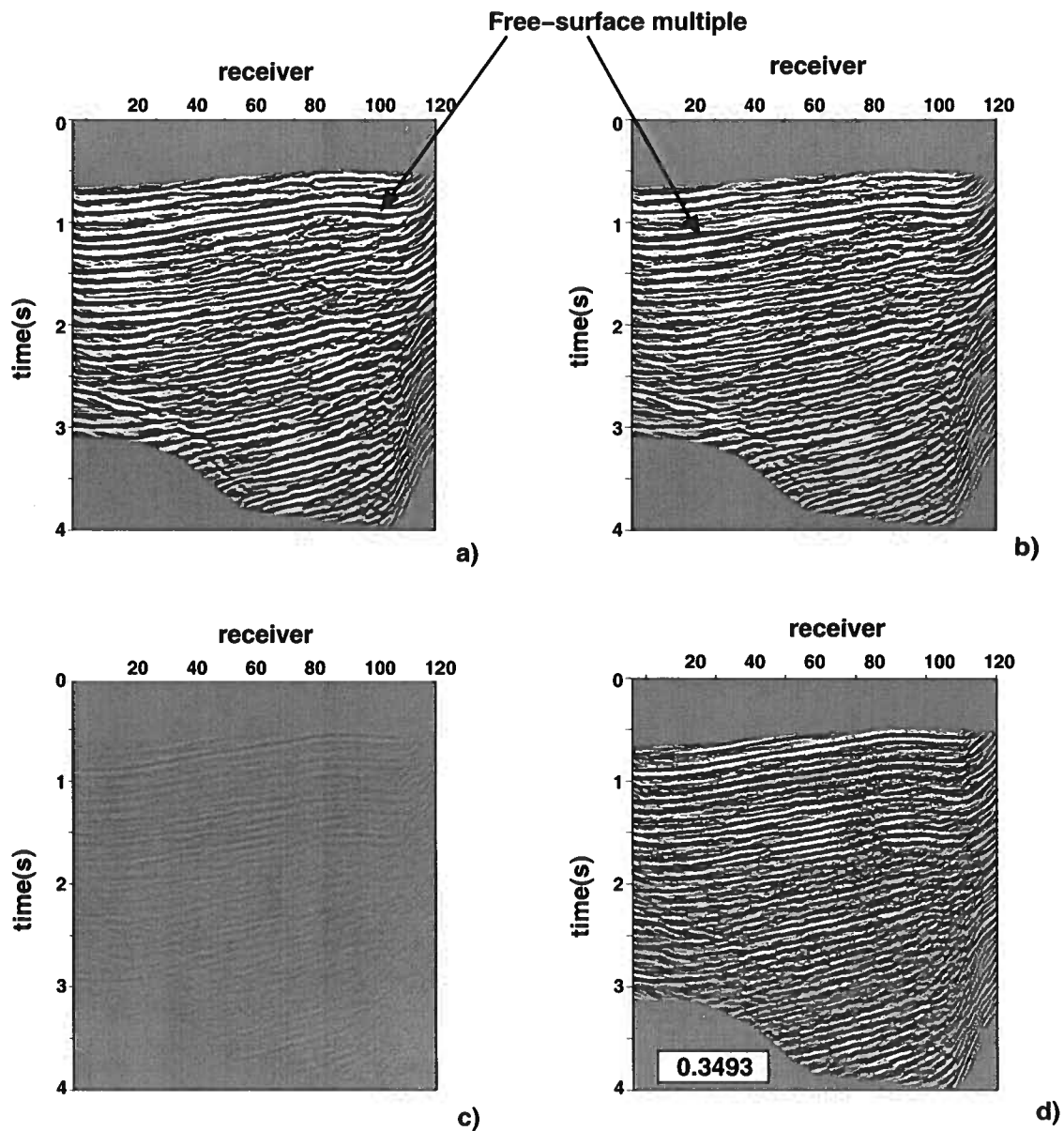
Figure 3.4. Images generated by migrating the virtual source data. Virtual source gathers are generated by correlating the direct arrival time-windowed in the total wavefield at the virtual source with the total wavefield at the receivers. Figure (a) is the image for the year 2004. Figure (b) is the image for the year 2005. Figure (c) is the difference of the two images, after time alignment, obtained on the same grey scale as figures (a) and (b). Figure (d) is the difference of the images amplified by a factor of 10, on the same grey scale as figures (a) and (b). The NRMS value is shown in the box in figure (d).

Figure 3.5. Images generated by migrating the virtual source data. Virtual source gathers are generated by correlating the downgoing waves at the virtual source with the upgoing waves at the receivers. Figure (a) is the image for the year 2004. Figure (b) is the image for the year 2005. Figure (c) is the difference of the two images, after time alignment, obtained on the same grey scale as figures (a) and (b). Figure (d) is the difference of the images amplified by a factor of 10, on the same grey scale as figures (a) and (b). The NRMS value is shown in the box in figure (d).

supports the improvement in repeatability after up-down wavefield separation. This improvement results because the waves now are those that propagate predominantly through the subsurface [solid rays in figure 3.2(c)]. Wavefield separation applied to the virtual source method has suppressed the first-order multiples propagating through the overburden, hence making the virtual source image less sensitive to overburden-related changes. The difference image still has some low-amplitude coherent events. These events could be the weaker amplitude multiples that are downgoing at the virtual source, upgoing at the receivers and yet still have propagated through the overburden (dashed rays in figure 3.2(d)). These multiples cannot be suppressed even by applying wavefield separation to the virtual source method.

Other sources of discrepancies in the time-lapse virtual source data can be further reduced by time-windowing the direct arrival in the downgoing waves at the virtual source, instead of using all of the downgoing waves. Time-windowing the direct arrival in the downgoing waves imposes the virtual source to be a P-wave source, hence suppressing the non-repeatability in the shear waves. The images for the years 2004 and 2005 obtained by migrating the resulting virtual source data are shown in figures 3.6(a) and 3.6(b), respectively, and the differences are shown in figures 3.6(c) and 3.6(d). Compared to the images generated using the refocused conventional seismic data (figures 3.1(a) and 3.1(b)), the images generated by the virtual source data preserves all the coherent reflectors and are less noisy.

Using up-down wavefield separation and windowing of the direct arrival at the virtual source has reduced the NRMS of the difference image just to 0.1770 (Table 3.1). Although the variation in the shear waves is suppressed, the second-order multiples that propagate through the time-varying overburden (dashed rays in figure 3.2(d)) still exist.

Application of wavefield separation to the virtual source method reduces the NRMS values, hence improving the repeatability. Improvement in the virtual source method by wavefield separation applied to the Mars field accounts for the variation in the sea water level, sea surface roughness, sea water temperature, salinity and source location. The variation in the source power spectrum [eq. (2.3)], however, still exist in all the above images. The next section address the correction for the variation of the source power spectrum.

3.7   Source Power Spectrum Variation

The correlation of the wavefields recorded by a given pair of receivers [eq. (2.3)] contains the power spectrum of the source pulse. To suppress the influence of the source power spectrum, and in particular its variation, the correlated data (correlation gather) must be deconvolved by the source power spectrum, presuming that it is known or can be well approximated (Derode, et al., 2003; Schuster, et al., 2004; Snieder, 2004; Wapenaar, 2004; Wapenaar, et al., 2005). Typically, the source pulse varies not only between the two surveys but also among shots in a single survey. Since air guns are used as sources, variation in the source pulse is mainly due to changes in the air bubble, assuming that pre-processing of the two data sets attempted to equalize the source pulses. The equalization of the source
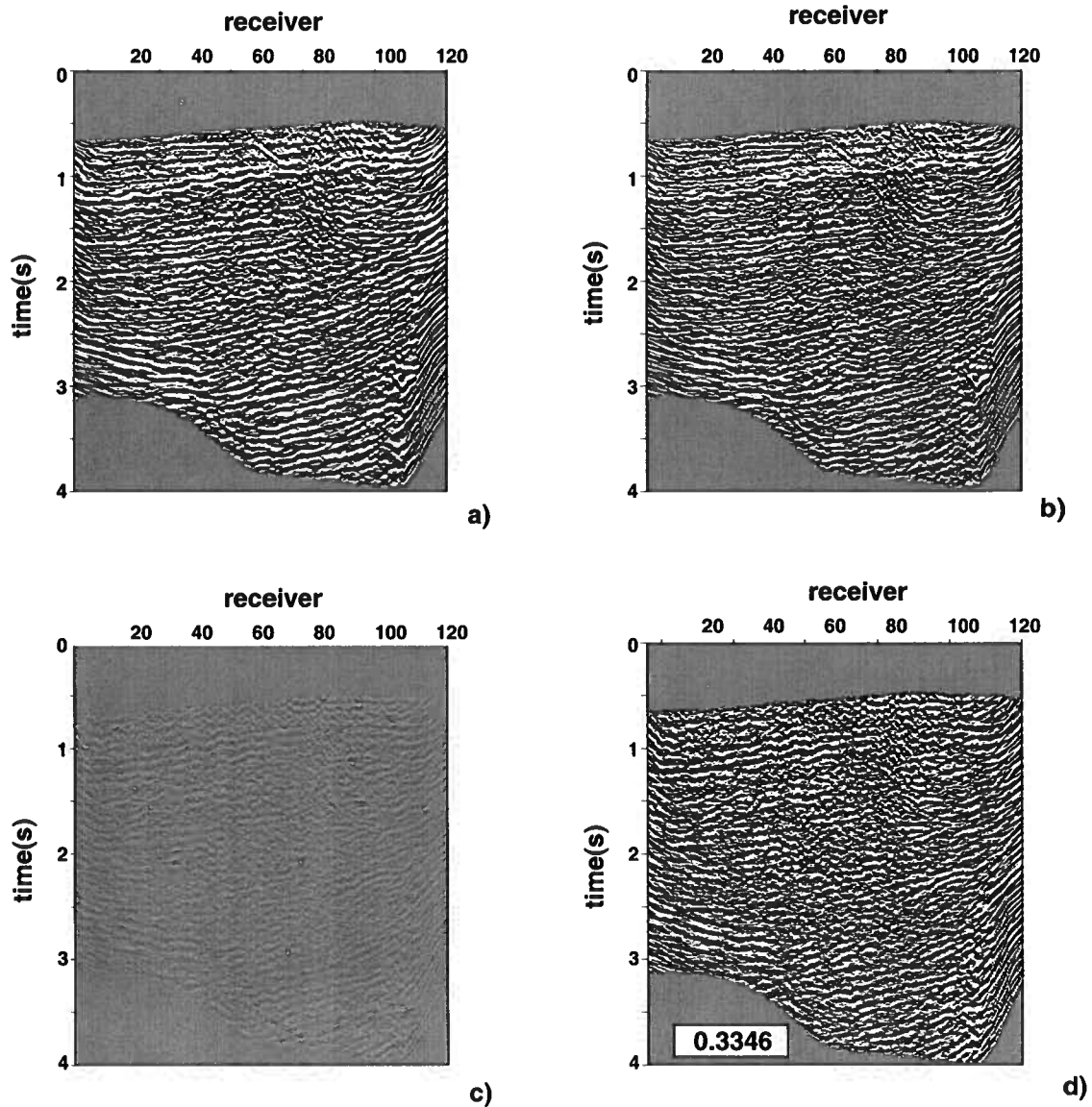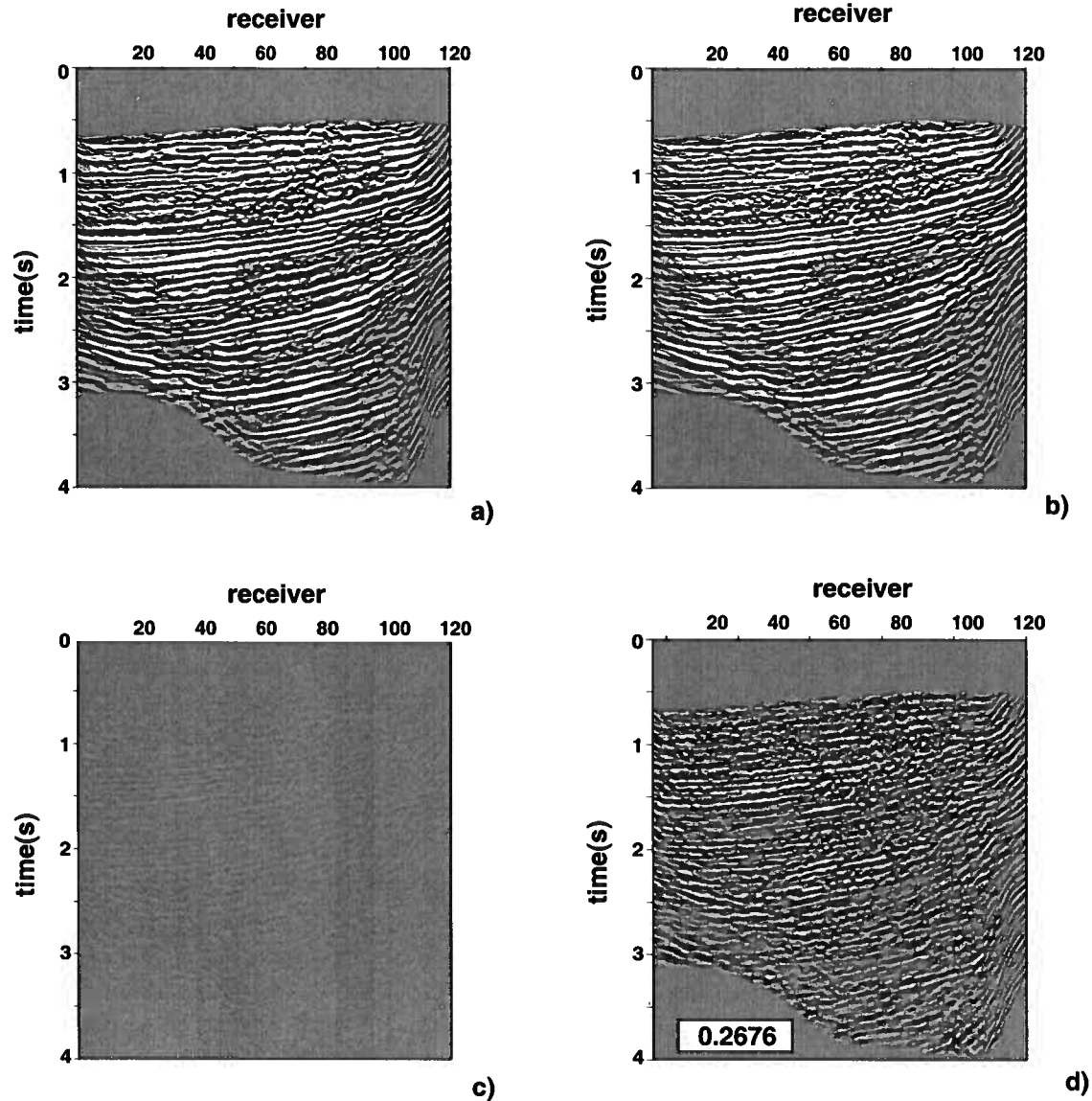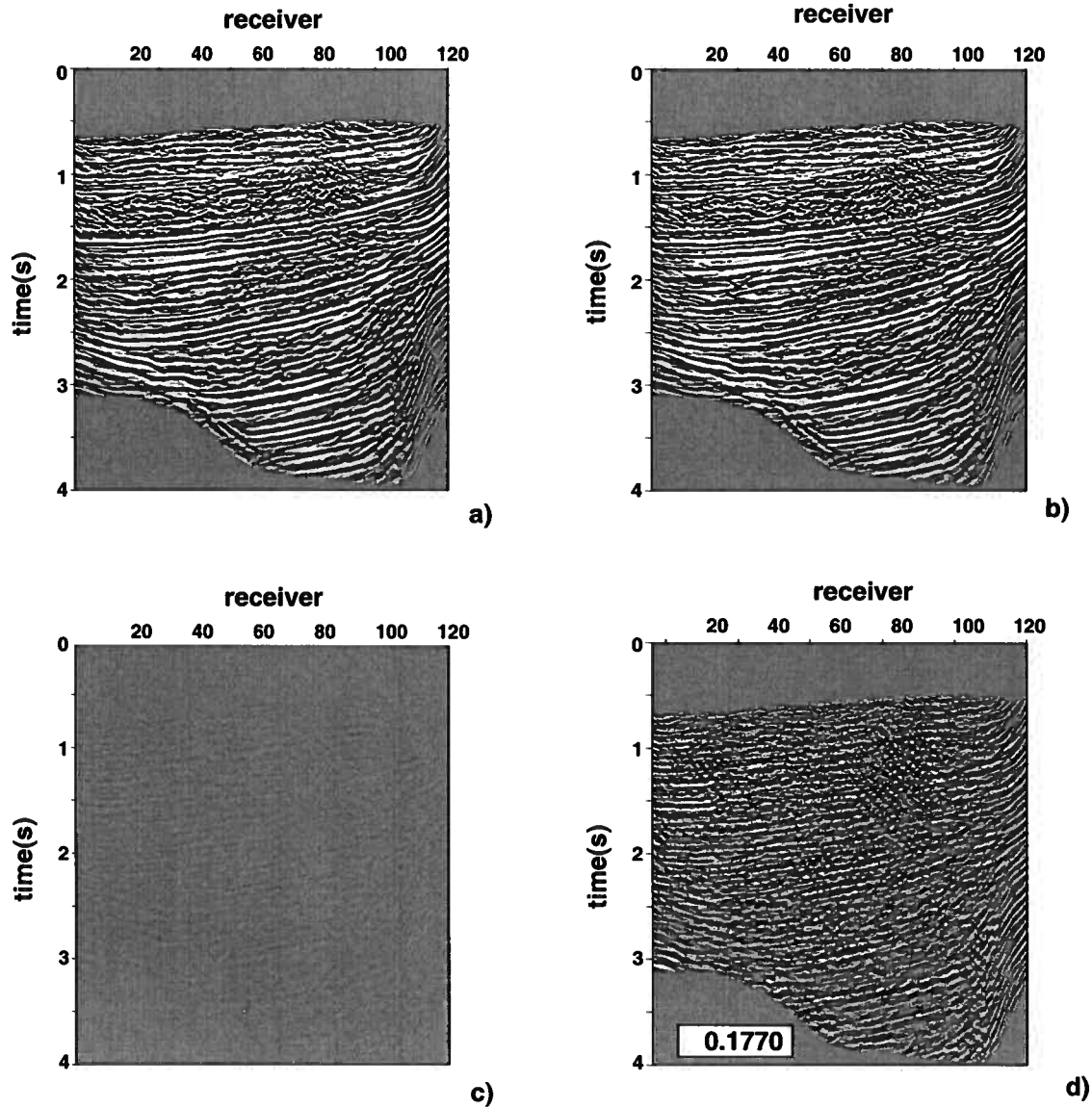
Figure 3.6. Images generated by migrating the virtual source data. Virtual source gathers are generated by correlating the direct arrival time-windowed in the downgoing waves at the virtual source with the upgoing waves at the receivers. Figure (a) is the image for the year 2004. Figure (b) is the image for the year 2005. Figure (c) is the difference of the two images, after time alignment, obtained on the same grey scale as figures (a) and (b). Figure (d) is the difference of the images amplified by a factor of 10, on the same grey scale as figures (a) and (b). The NRMS value is shown in the box in figure (d).

pulse was done as follows. Small-offset traces were taken from each shot and the waves, in a time window of 400 ms around the direct arrival, were aligned. The length of the time window was chosen to be 400 ms to include the bubble. These aligned traces were then averaged, after which designative filters were derived to turn these responses into band-limited delta functions. The same procedure was applied to both the surveys to obtain the same desired band-limited delta function. This conventional pre-processing aimed to remove variations in the bubble sequence but was not sensitive enough to remove them completely.

The source power spectrum corresponds, in the time domain, to the auto-correlation of the source wavelet. The auto-correlation of the source wavelet present in the correlation gather varies from one shot to another because of changes in the residual bubble sequence. The variation of the auto-correlation of the source pulse (for receiver 90) as a function of source location for the years 2004 and 2005 is shown in figures 3.7(a) and 3.7(b), respectively. Each of the two figures is the auto-correlation of the direct arrival time-windowed in the downgoing waves at receiver 90 for all the source locations. Downgoing waves are used for correlation to avoid any near-seafloor reflection interfering with the auto-correlation of the source pulse. The auto-correlation of the source pulse varies not only between the two surveys but also between each source location. The event close to ± 0.35 s is attributable to the residual bubble. Apart from the residual bubble, curved events are present for both causal and acausal times. These curved events correspond to the interference of reflected and refracted waves with the direct arrival for later times and larger offsets. Figure 3.7(c) is the difference in the auto-correlation of the source pulse for the years 2004 and 2005. The difference in the main lobe (close to time t=0) is negligible, suggesting that pre-processing adequately equalized the primary source pulses. The curved events also appear to diminish in the difference. The event occurring around ± 0.35 s, however, is the difference in the residual bubble and is pronounced and consistent for every source location. This consistent difference could be due to the variation in the water temperature between the two surveys; the base survey was carried out in October and the repeat survey in June. Use of different air gun sources for the two surveys, different air gun pressures, different actual depths of source arrays (both surveys used the same nominal source depth), and discrepancies in the sea surface roughness could be other possible reasons for the systematic variation in the residual bubble.

The imprint of varying source power spectrum on the virtual source data can be removed by deconvolving each trace of the correlation gather by the power spectrum of the corresponding source. This is equivalent to applying a filter that represents the inverse of the source power spectrum. The convolution of the filter with the source power spectrum is referred to as *self-decon*. Figure 3.7(d) is the difference of self-decons for the years 2004 and 2005. Apart from the curved events representing the interference of other events with the direct arrival, the contribution of the systematic residual bubble variation is well suppressed. Hence, deconvolving the correlation gather by the source power spectrum suppresses the source power spectrum variations.

Migrated images, for the years 2004 and 2005, generated after applying both wavefield separation and deconvolution of the correlation gather by the source power spectrum are
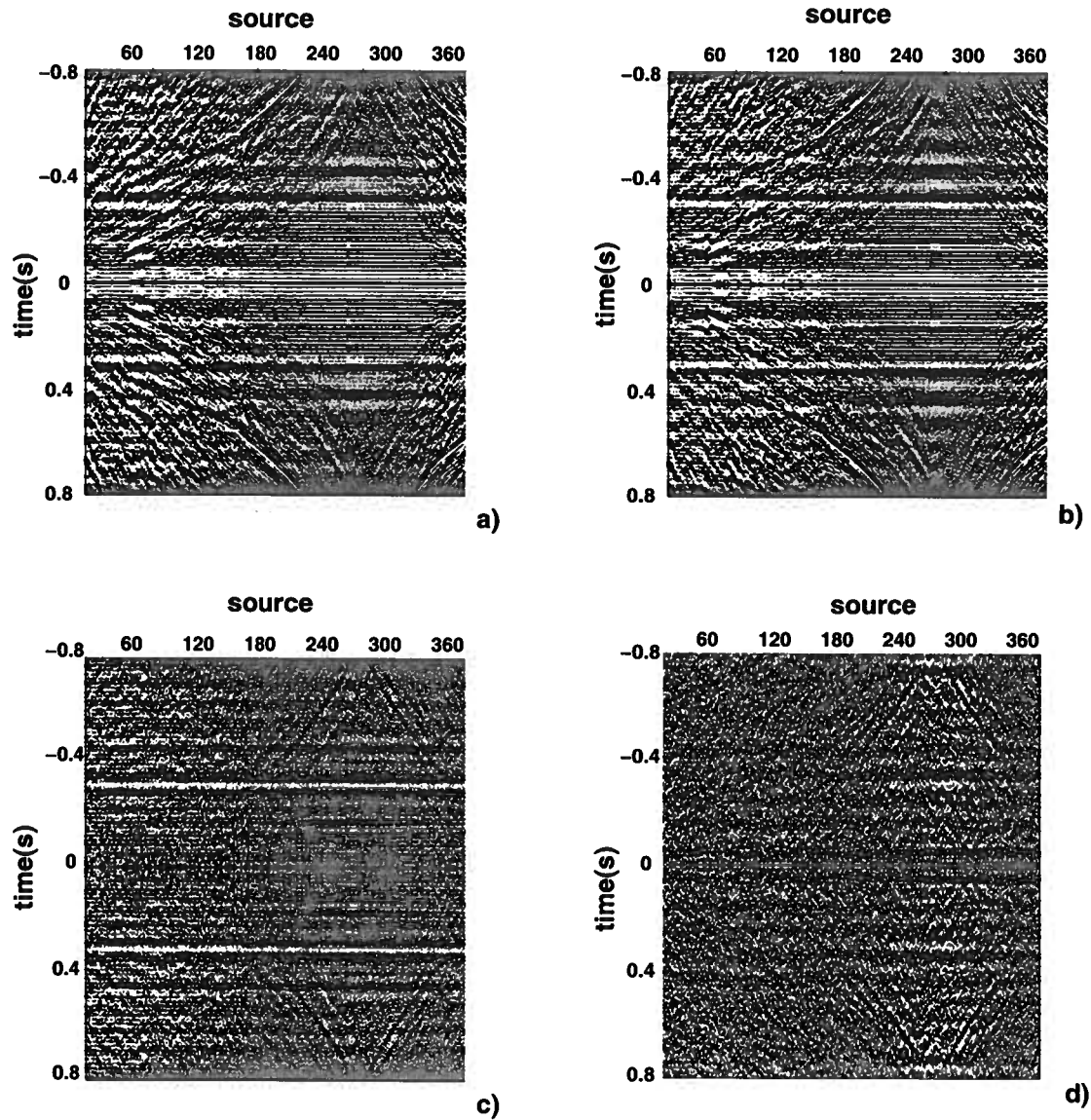
Figure 3.7. Variation of the auto-correlation of the source pulse corresponding to receiver 90 as a function of source location for 2004 (a) and 2005 (b). Figure (c) is the difference of the gathers in (a) and (b), obtained on the same grey scale as Figures (a) and (b). Figure (d) is the difference of the self-decons (convolution of the source power spectrum and filter that represents the inverse of the source power spectrum) for the years 2004 and 2005, on the same grey scale as figures (a) and (b).

Figure 3.8. Images generated by migrating the virtual source data. Virtual source gathers are generated by correlating the downgoing waves at the virtual source with the upgoing waves at the receivers, followed by deconvolving the source power spectrum before stacking. Figure (a) is the image for the year 2004. Figure (b) is the image for the year 2005. Figure (c) is the difference of the two images, after time alignment, obtained on the same grey scale as figures (a) and (b). Figure (d) is the difference of the images amplified by a factor of 10, on the same grey scale as figures (a) and (b). The NRMS value is shown in the box in figure (d).

shown in figures 3.8(a) and 3.8(b) respectively, with differences shown in figures 3.8(c) and 3.8(d). The virtual source data for these images are generated by correlating the downgoing waves at the virtual source with the upgoing waves at the receivers. The correlation gather is then deconvolved by the source power spectrum and stacked over the physical sources. The improvement in the repeatability by combining up-down separation and deconvolution of the correlation gather with the auto-correlation of the source-time function is evident by the decrease in the NRMS to 0.1624 (Table 3.1).

The repeatability can be further improved by combining up-down separation, time-windowing of the direct arrival and deconvolution. The images in figures 3.9 are obtained by migrating the virtual source data generated by combining up-down separation, time-windowing of the direct arrival, and deconvolution. The NRMS, after combining up-down separation, time-windowing the direct arrival and deconvolution, reduces from 0.1624 without windowing to 0.1414.

Combination of up-down separation, time-windowing the direct arrival and deconvolution with the source power spectrum thus, improves the repeatability of the images created with the virtual source data. This makes the virtual source method a useful tool for time-lapse monitoring where the goal is to image changes just in the subsurface beneath the sources and the receivers. Up-down separation suppresses the first-order multiples from the time-varying overburden. Time-windowing the direct arrival in the downgoing waves imposes a P-wave virtual source, hence suppressing the overburden-related variations in the shear waves. Finally, deconvolution of the correlation gather by the source power spectrum further suppresses the non-repeatability caused by variation in the source power spectrum. The progressively diminishing values of NRMS in the sequence of tests supports our observation of improvement in time-lapse monitoring by applying wavefield separation and deconvolution to the virtual source method.

For the Mars field OBC data, the estimation of the source-time function was possible because the source was impulsive (air gun). For applications such as earthquake data and other passive seismic recordings, however, the source-time function is long and hence difficult to estimate. For such applications, the deconvolution of the correlation gather by the source power spectrum becomes difficult. In order to avoid dealing with the source-time function, a preferred tool for seismic interferometry is deconvolution (Snieder and Şafak, 2006; Vasconcelos and Snieder, 2006; Vasconcelos and Snieder, 2007a; Vasconcelos and Snieder, 2007b; Vasconcelos and Snieder, 2007c; Vasconcelos, et al., 2007a; Vasconcelos, et al., 2007b). The next chapter focuses on the use of deconvolution to estimate the near-surface properties and characterize mode conversion.
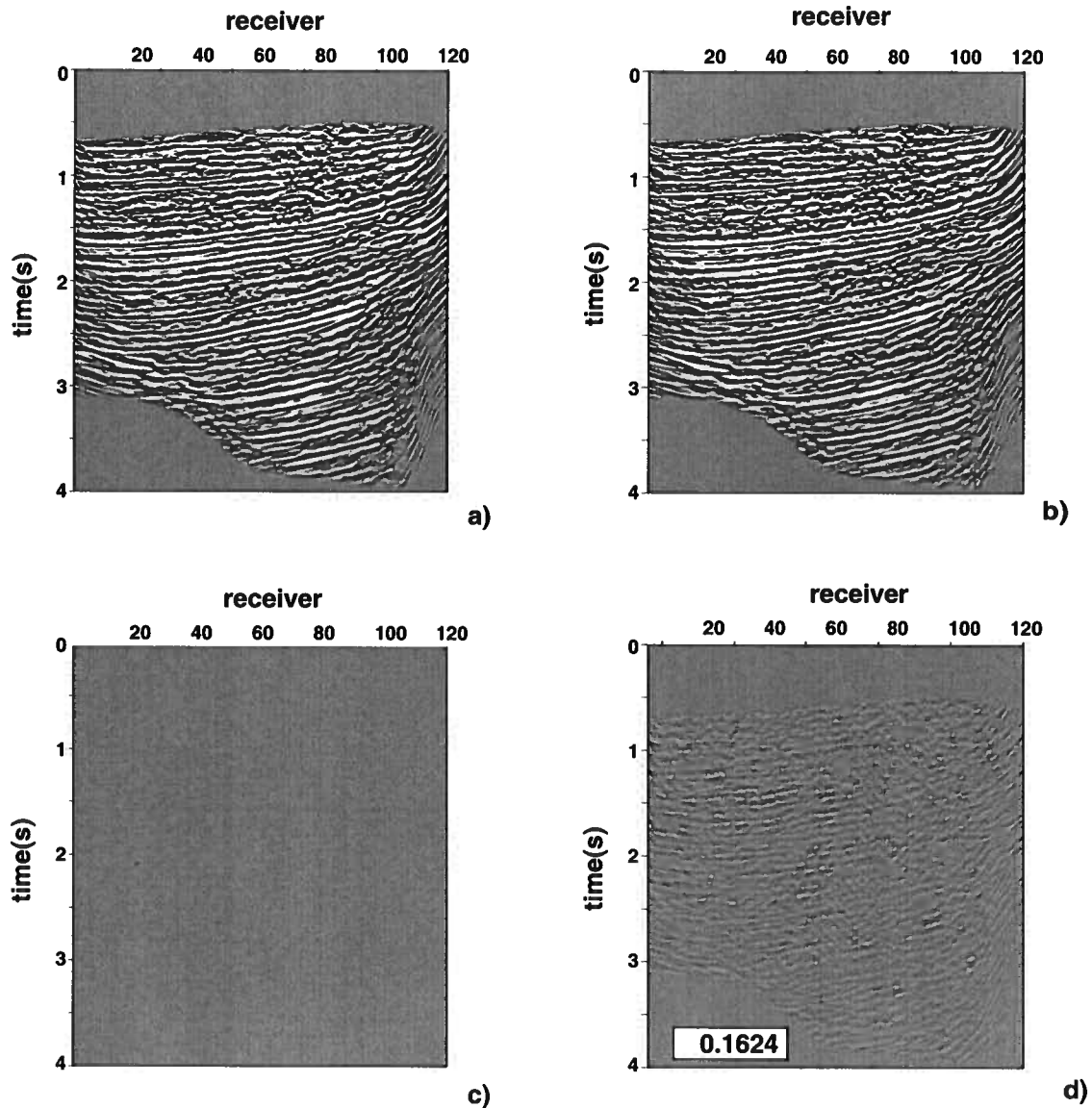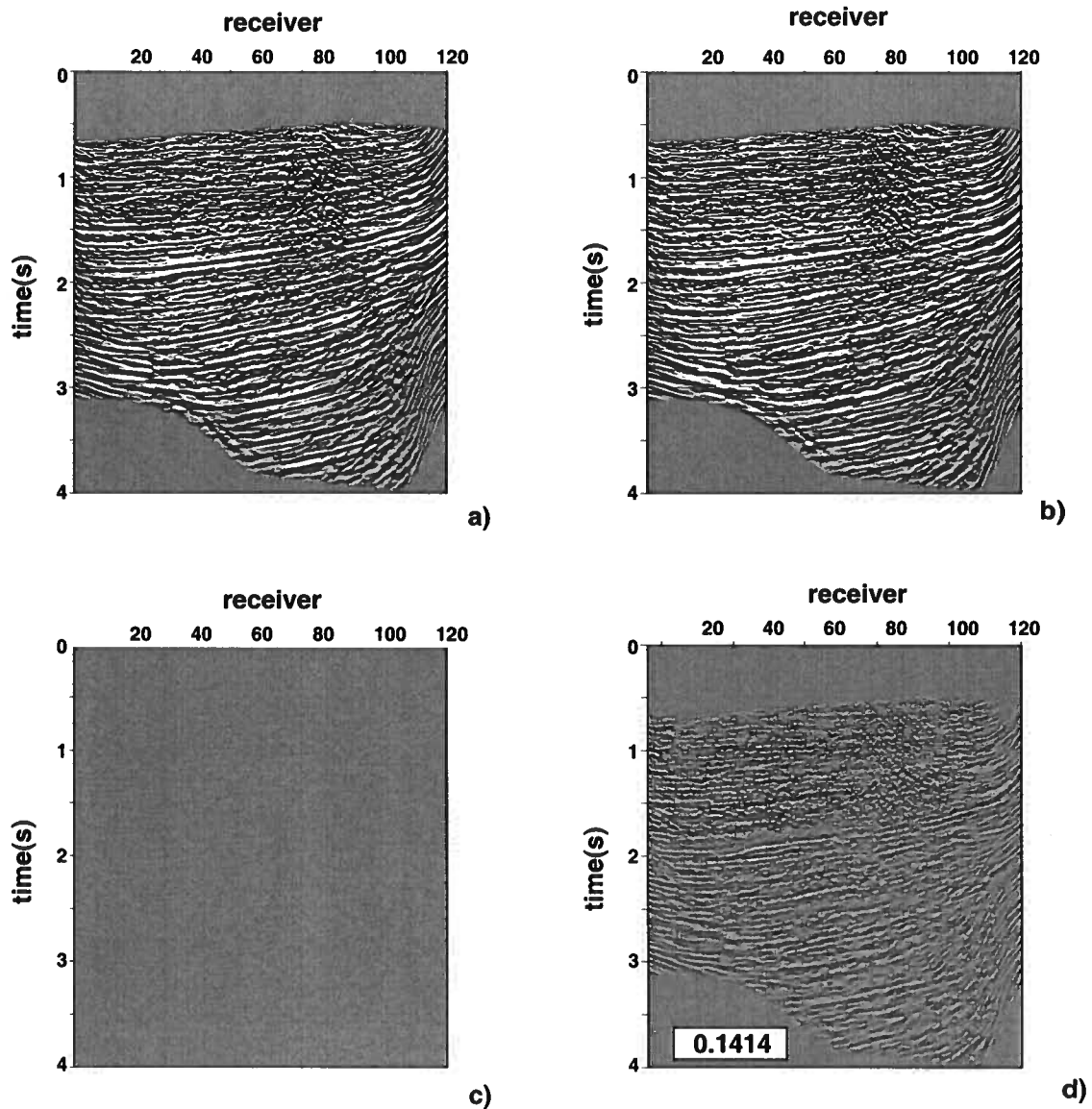
Figure 3.9. Images generated by migrating the virtual source data. Virtual source gathers are generated by correlating the direct arrival time-windowed in the downgoing waves at the virtual source with the upgoing waves at the receivers, followed by deconvolving the source power spectrum before stacking. Figure (a) is the image for the year 2004. Figure (b) is the image for the year 2005. Figure (c) is the difference of the two images, after time alignment, obtained on the same grey scale as figures (a) and (b). Figure (d) is the difference of the images amplified by a factor of 10, on the same grey scale as figures (a) and (b). The NRMS value is shown in the box in figure (d).

Chapter 4

Improving the virtual source method by wavefield separation

4.1 Summary

The virtual source method has a few challenges, related to the implementation issues such as limited acquisition aperture and reflections/multiples coming from the overburden. Some of these challenges can be overcome by separating the wavefield into upgoing and downgoing waves, hence improving the quality of virtual source data. First, it suppresses the artifacts associated with the limited acquisition aperture typically used in practice. Second, it helps reconstruct a response in the absence of downgoing reflections and multiples from the overburden. These improvements in removing the artifacts due to limited acquisition aperture and overburden-related multiples are illustrated on a synthetic dataset of a complex layered model modeled after the Fahud field in Oman, and on OBC data acquired in the Mars field in the deepwater Gulf of Mexico.

4.2 Introduction

The simplest approach to generating virtual source gathers is to correlate the total wavefield recorded at the virtual source location with the total wavefield recorded at the receivers (Mehta, et al., 2006). The resulting virtual source gather includes the complete response between the virtual source and the receiver. Theory states that true response between a given pair of receivers is obtained by correlating the wavefields recorded at the two receivers and stacking the correlation gather over sources enclosing the two receivers. As discussed in the previous chapter, however, for geophysical applications there are challenges in the form of implementation issues such as incomplete source aperture and the downgoing reflections and multiples from the overburden. This chapter demonstrates the usefulness of wavefield separation to overcome some of them.

The current practice to generate a virtual source gather is to correlate the time-windowed direct arrival in the total wavefield recording at the virtual source with the total wavefield at the receivers (Bakulin and Calvert, 2004, 2006; Calvert, et al., 2004). This approach suppresses some of the unwanted responses as compared to the simplest approach. Neither the simplest approach (correlating the total wavefields at both the virtual source and the receivers) nor the current practice (correlating the direct arrival in the total wavefield at the virtual source with the total wavefield at the receivers) gives the true

subsurface response. Apart from the spurious events due to incomplete source aperture, for both the simplest approach and the current practice, reflections from the overburden and the free-surface are present in the virtual source data. These unwanted responses obscure the target reflections.

Up-down wavefield separation shows promise for improving the virtual source data quality by suppressing the artifacts due to incomplete source aperture, and the reflections coming from the overburden and the free-surface. Similar up-down wavefield separation is done by Snieder, et al. (2006b) in a different context applied to structural engineering. The following section illustrates this improvement using a layered synthetic model.

Apart from imaging below complex overburden, seismic interferometry is also a powerful tool for time-lapse monitoring with permanently placed receivers. The final section illustrates the improvement in the virtual source method using wavefield separation for the Mars field OBC data. Wavefield separation helps suppress the strong reflection from the sea-surface, hence unraveling the reflection response. Chapter 4 demonstrates how wavefield separation improves the repeatability for time-lapse monitoring by making the response independent of variations in the sea water level, sea surface roughness, sea water temperature, salinity, source location, and source signature.

4.3   Synthetic Modeling

Figure 4.1 shows the vertical profiles of the P- and the S-wave velocities used for synthetic simulation by reflectivity modeling (Schmidt and Tango, 1986). The density varies between 2100 to 2500 kg/m^3. 161 sources (vertical forces) are placed, every 10 m, on the surface and 41 receivers are placed, every 10 m, in a horizontal well at a depth of 250 m. The objective is to create virtual sources along the horizonal well to suppress the distorting effects of the near-surface overburden (above 200 m), when trying to image the reservoir layers labeled 1 through 4. The complex overburden (i.e. the region above the receivers) consists of layers with extremely high velocity contrasts typical of the Middle East, and here modeled after the Fahud field in Oman.

If ideal redatuming is to be performed with seismic interferometry then the reconstructed response corresponds to a buried virtual source at any of the receivers. This response will contain reflections from the overburden layers as well as the free-surface multiples.

Bakulin and Calvert (2004, 2006) showed how time-windowing the direct arrival before correlation can eliminate some of the overburden reflections. This makes the virtual source radiate predominantly downwards and provides cleaner response from deep target reflectors. Their approach, however, cannot suppress the downgoing reflections and multiples from the overburden. This chapter focuses on completely eliminating from the virtual source data all the first-order reflections and multiples related to the overburden.

The virtual source data is benchmarked against the "ground truth" response computed for a new model where a physical source is placed at the virtual source location and all the overburden above the well is replaced by a homogeneous half-space with the same velocities as for the original model just below the receivers (figure 4.1).
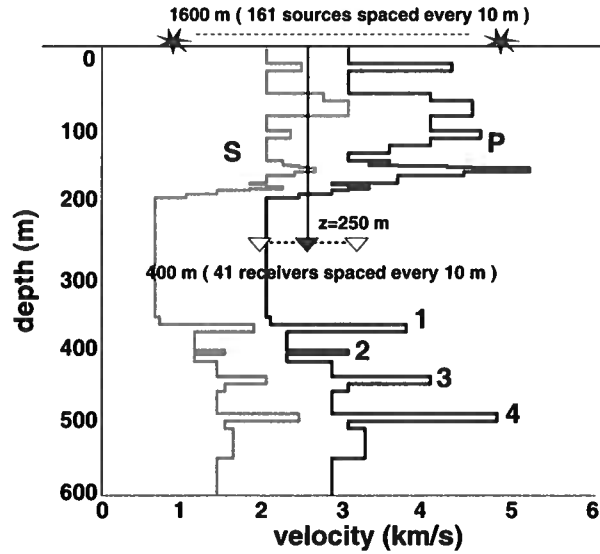
Figure 4.1. P- and S-wave velocity profiles and the acquisition geometry for synthetic model inspired by Middle East field Fahud. 161 sources are spaced every 10 m on the surface and 41 receivers are placed on a horizontal well at a depth of 250 m. Receiver spacing is 10 m.
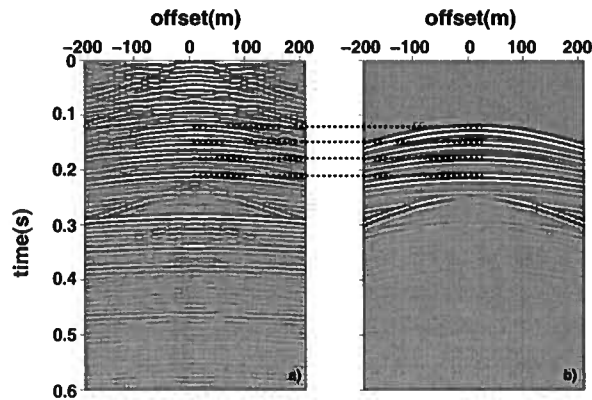
Figure 4.2. Figure (a) shows the virtual source gather generated by correlating the total wavefield at the virtual source (receiver 21) with the total wavefield at the receivers. Figure (b) shows the shot gather generated by placing a physical source (vertical force) at the virtual source location (receiver 21) and a homogeneous half space above it. In Figure (b), the laterally propagating shear waves have been removed.
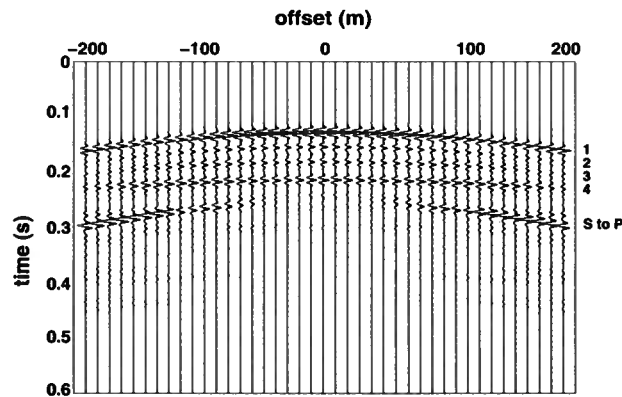
Figure 4.3. Ground truth response generated by putting a physical source (vertical force) at the virtual source location (receiver 21). The laterally propagating shear waves have been removed.

Receiver 21 (middle receiver), highlighted in red in figure 4.1, is selected to be the virtual source. This virtual source gather should be equivalent to the response obtained by placing a physical source at the location of receiver 21 for the new model. Figure 4.2 shows a comparison of the two responses. Figure 4.2(a) shows the virtual source gather generated by correlating the total wavefield at the virtual source location (receiver 21) with the total wavefield at the receivers. Figure 4.2(b) shows the wavefield response of the receivers to a physical source (vertical force) at the virtual source location, after removing the laterally propagating shear waves. The laterally propagating shear waves are removed by using only the upgoing energy at the receivers. This response will be referred to as the ground truth response. In addition to the four P-P reflection events corresponding to the high-velocity features, labeled 1 through 4 in figure 4.1, which are present in both types of gather, the virtual source gather contains numerous other events.

For easier comparison the ground truth response is replotted as shown in figure 4.3. The four P-P reflections labeled 1 through 4 and an S to P conversion is observed. Further analysis is, however, restricted to P-waves only. Figure 4.4 shows the virtual source gather, plotted in red, on top of the ground truth, plotted in black. As mentioned earlier, apart from the agreement in the reflection events, numerous other events exist in the virtual source gathers. Some of them are of physical nature (overburden-related response) and some are unphysical (artifacts arising from limited source aperture), but both represent unwanted responses where the goal is to obtain only reflections from the subsurface. The next section focuses on demonstrating how wavefield separation suppresses both types of undesired response.

Figure 4.4. Black lines show the ground truth response. Red lines show the virtual source gather generated by correlating the total wavefield at the virtual source (receiver 21) with the total wavefield at the receivers.

4.4   Wavefield Separation

The final section in the previous chapter illustrated, using a three-layered depth-section cartoon (figure 2.30), the reasons for the spurious events due to limited source aperture and the energy coming from the overburden. Apart from the four P-P reflections, the numerous other events in figure 4.4 are the spurious events due to limited source aperture and the reflections/multiples coming from the overburden.

These spurious events can be suppressed using wavefield separation. As shown in figure 2.30(b), the wavefield propagating along the red arrows is recorded by the virtual source and the receivers as upgoing waves. If the wavefield at the virtual source is restricted to be only downgoing, these spurious events can be suppressed.

Even though the waves at the virtual source are only downgoing, the reflections from the overburden and the free-surface, propagating along the ray path as shown by the red arrows in figure 2.30(d), will also be recorded as a part of the virtual source data. These correspond to physical arrivals and would be a part of the response if a physical source was present at the virtual source location. The effect of these arrivals can be suppressed by restricting the waves at the receivers to be only upgoing. Hence, the true subsurface response can be obtained by correlating the downgoing energy at the virtual source location with the upgoing energy at the receivers. The idea is similar to Noah's deconvolution as suggested by Riley and Claerbout (1976), an approach to generate seismograms in the absence of the free-surface effects by deconvolving the upgoing waves with the downgoing waves. If such separation is achievable without distortions, it may represent an improvement over the current practice of time-windowing the direct arrival at the virtual source location and correlating that with the total wavefield at the receivers (Bakulin and Calvert, 2004, 2006; Calvert, et al., 2004). The following two subsections focus on generating the virtual

Figure 4.5. Black lines show the ground truth response. Red lines show the virtual source gather generated by correlating the time-windowed direct arrival at the virtual source (receiver 21) with the total wavefield at the receivers.

source data after separating the recorded wavefield by a) time-windowing the direct arrival in the total wavefield, and b) separating the recorded wavefield into upgoing and downgoing waves.

4.4.1   Windowing in Time

Figure 4.5 shows the virtual source gather (in red) generated by correlating the time-windowed direct arrival in the total wavefield at the virtual source with the total wavefield at the receivers. The time-windowed direct arrival is obtained by placing a time gate of 40 ms around the direct arrival. In comparison to the ground truth response (in black), the four reflection events are still preserved. As compared to figure 4.4 a lot of spurious events are suppressed. The suppression results from restricting the energy at the virtual source location to be mostly downgoing P-wave energy (in the form of direct arrival). Time-windowing the direct arrival thus improves the virtual source gather, although a better wavefield separation approach is to decompose the wavefield into upgoing and downgoing waves.

4.4.2   Up-down Separation

As demonstrated by the cartoons in figure 2.30, the desired subsurface response is obtained by correlating the downgoing energy at the virtual source location with the upgoing energy at the receivers. Instead of time-windowing the direct arrival, the wavefields are separated into upgoing and downgoing waves and then used for correlation. Figure 4.6 shows the virtual source gather (in red) generated by correlating the downgoing waves at the virtual source with the upgoing waves at the receivers. The spurious events are suppressed
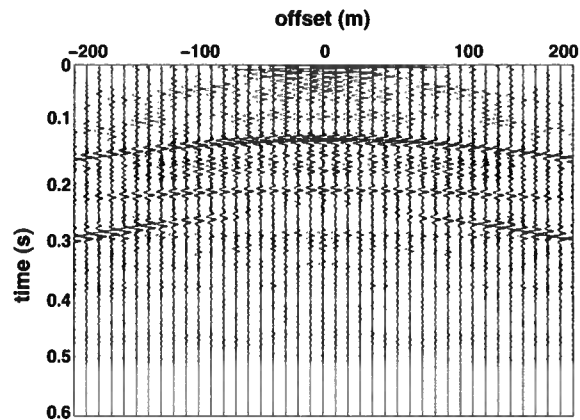
Figure 4.6. Black lines show the ground truth response. Red lines show the virtual source gather generated by correlating the downgoing waves at the virtual source (receiver 21) with the upgoing waves at the receivers.
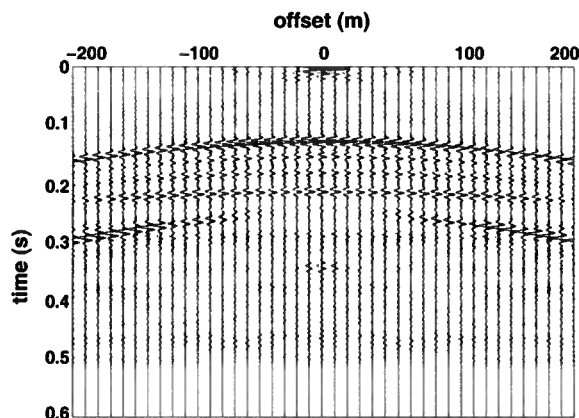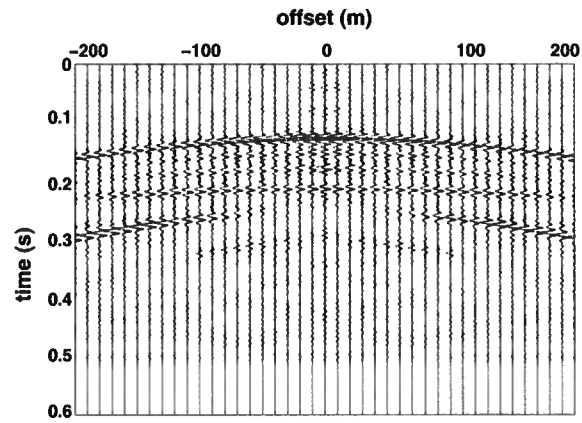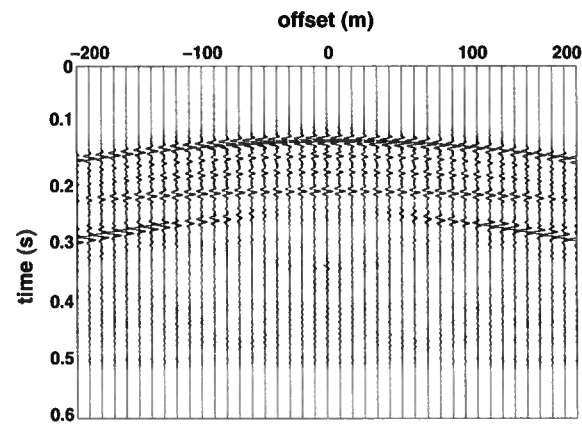

Figure 4.7. Black lines show the ground truth response. Red lines show the virtual source gather generated by correlating the direct arrival time-windowed in the downgoing waves at the virtual source (receiver 21) with the upgoing waves at the receivers.

because only the downgoing waves at used at the virtual source for correlation. Similarly, the downgoing reflections and multiples from the overburden are also suppressed by using only the upgoing energy at the receivers. The virtual source gather closely matches the ground truth response. Hence, wavefield separation is indeed a promising tool for suppressing the spurious events and the downgoing reflections and multiples from the overburden, in the process of generating the virtual source gather.

The up-down separation and time-windowing can also be combined to generate the virtual source gather as shown in figure 4.7. This virtual source gather is generated by correlating the direct arrival time-windowed in the downgoing waves at the virtual source location with the upgoing waves at the receivers. For this synthetic model it shows a improvement over figure 4.6 because the subsurface below the horizontal well is pretty homogeneous except the four reflectors.

For field data this improvement will become prominent once the recorded wavefield is separated into upgoing and downgoing waves. For the synthetic modeling, the modeling program separated the wavefield into upgoing and downgoing waves. For the field data, however, the sensors record the total wavefield. This recorded wavefield can be separated into upgoing and downgoing waves using a well known technique known as the dual-sensor summation (Ball and Corrigan, 1996; Barr and Sanders, 1989; Barr, et al., 1996; Barr, 1997; Barr, et al., 1997; Canales and Bell, 1996; Dragoset and Barr, 1994; Jiao, et al., 1998; Loewenthal, 1994; Loewenthal and Robinson, 2000; Paffenholz and Barr, 1995; Robinson, 1999; Soubaras, 1996), provided the wavefield is recorded by both the hydrophone and the vertical component geophone. According to dual-sensor summation, if both the hydrophone (H) and vertical component geophone (Z) records at the same sensor location, the sum H+Z yields the upgoing energy and the difference H-Z the downgoing energy. Before applying this to field data, let us compare the exact downgoing and upgoing waves, for our synthetic model with the waves separated by the H-Z and H+Z approximations respectively.

Figure 4.8 shows the exact downgoing waves for the raw data (plotted in black) and obtained from H-Z (plotted in red). Similarly, figure 4.9 shows the exact upgoing waves for the raw data (plotted in black) and from H+Z (plotted in red). In each plot the wavefields obtained in two different ways are practically identical, suggesting that despite being strictly valid for zero-offset data in horizontally layered media, dual-sensor summation technique provides a reasonable separation of the wavefield into upgoing and downgoing waves for all offsets at hand.

4.5   Field Example: Redatuming Ocean Bottom Seismic at Mars

In this section, the improvement in the virtual source gathers due to wavefield separation is demonstrated using the data recorded for seismic monitoring in the Mars field (figure 2.17) located in the deepwater Gulf of Mexico. Sea level, water velocity and shot locations vary between repeat acquisitions even though receivers remain permanently placed on the seafloor. These acquisition discrepancies and time-varying overburden creates a problem for seismic monitoring aimed to detect the amplitude changes related to field depletion. The virtual source method allows us to redatum OBC data to the seafloor without knowing
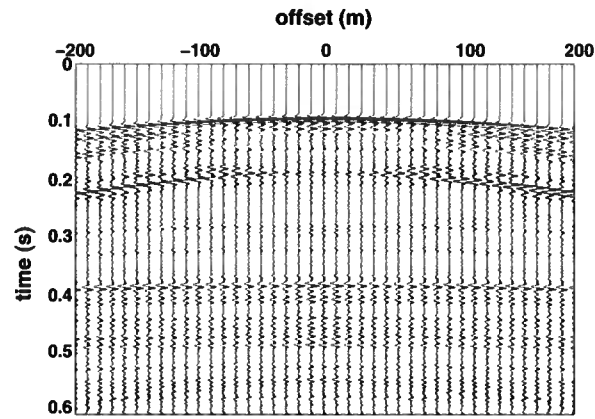
Figure 4.8. Comparison of the exact downgoing waves (black lines) with the H-Z approximation (red lines).
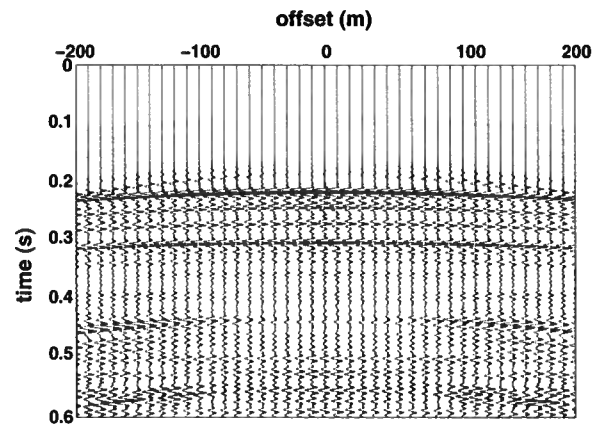
Figure 4.9. Comparison of the exact upgoing waves (black lines) with the H+Z approximation (red lines).
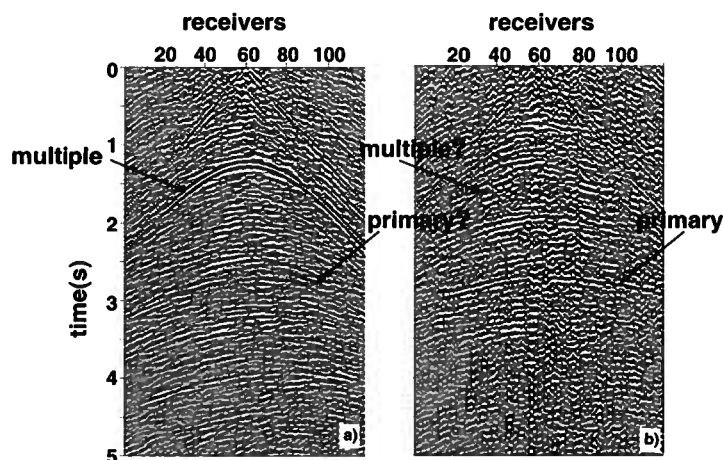
Figure 4.10. Virtual source gathers generated with receiver 60 as the virtual source. Figure (a) shows the virtual source gather generated by correlating the total wavefields at both the virtual source and receiver locations. Figure (b) shows the virtual source gather generated by correlating the downgoing waves at the virtual source location with the upgoing waves at the receivers. The label "multiple" refers to the reflection from the free-surface (overburden) and the label "primary" refers to the reflection from the subsurface. The label "primary?" and "multiple?" refers to the absence of the respective event.

any of the overburden-related variations. Redatumed data should correspond to fixed (virtual) source and fixed receiver and hence, exhibit greatly improved repeatability between surveys. This was shown by Bakulin and Calvert (2006) for synthetic and real data of repeated vertical seismic profiles (VSP) acquired over time-varying overburden.

For the synthetic model, the improvement is observed in the virtual source gathers by up-down wavefield separation. For the Mars field data, the dual-sensor summation technique is used for the separation of the wavefield into upgoing and downgoing waves. These separated upgoing and downgoing waves are then used to generate the improved virtual source gathers.

Before summing and differencing the hydrophone and the vertical geophone, it is essential to calibrate the vertical geophone to the hydrophone because there could be coupling variations and/or amplifier gain differences in the hydrophone and the vertical component geophone. The calibration of the vertical geophone to the hydrophone is done as follows. The first step is to align the first arrivals of hydrophone and vertical geophone for small offset traces using the geometry and correlation. The first arrivals are then averaged over the hydrophone and the vertical geophone separately so as to average out any contribution from reflectors near the seafloor. The hydrophone records the wavefield that can be represented as : $D*(1+R)$ where D is the direct arrival and R is the water bottom reflection coefficient. In contrast, the vertical geophone records $D*(-1+R)$. In the time gate below

Figure 4.11. Virtual source gathers generated with receiver 60 as the virtual source. Figure (a) shows the virtual source gather generated by correlating the direct arrival time-windowed in the total wavefield at the virtual source with the total wavefield at the receiver locations. Figure (b) shows the virtual source gather generated by correlating the direct arrival time-windowed in the downgoing waves at the virtual source location with the upgoing waves at the receivers. The label "multiple" refers to the reflection from the free-surface (overburden) and the label "primary" refers to the reflection from the subsurface. The label "primary?" and "multiple?" refers to the absence of the respective event.

the direct arrival and above the free-surface reflection, the data should be upgoing. Using this information, a scalar value is determined per vertical geophone and applied to the hydrophone before doing the dual-sensor summation.

The geometry of figure 2.17 shows that the receivers record waves arriving at non-normal incidence. The angle of incidence depends on the source-receiver offset. For angle of incidence θ, instead of H+Z, the downgoing waves are strictly given by H+Z/$\cos\theta$. Similarly, H-Z/$\cos\theta$ strictly describes the upgoing waves. As demonstrated by figures 4.8 and 4.9, H+Z and H-Z are, however, good approximations for the upgoing and downgoing waves respectively.

For the Mars field OBC data, receiver 60 (middle receiver) is selected as the virtual source and the correlation gather is stacked over all the sources. Figure 4.10(a) shows the virtual source gather, for the hydrophone component, generated by correlating the total wavefield recorded at the virtual source location with the total wavefield at the receivers. The most prominent reflection is the reflection from the sea-surface, labeled as "multiple" in the figure. The arrow with the "primary?" mark is the location where the strongest true reflection is expected from the subsurface, but is absent. Hence, even for a simple overburden, correlating the total wavefields gives a virtual source gather dominated by the reflection from the sea-surface.

Using the hydrophone and the vertical component geophone recording and the dual-sensor summation technique the upgoing and downgoing waves are separated at all receivers. If instead of correlating the total wavefields, the downgoing waves at the virtual source are correlated with the upgoing waves at the receivers, the virtual source gather obtained is shown in figure 4.10(b). The free-surface multiple is suppressed (highlighted by the arrow and "multiple?" mark). The reflections from the deeper subsurface are now visible and the strongest one is highlighted by an arrow and labeled as "primary." Even though the reflections from the subsurface are visible, the virtual source gather is still noisy.

Figure 4.11(a) shows the virtual source gather obtained by the current practice (Bakulin and Calvert, 2004, 2006; Calvert, et al., 2004): correlating the time-windowed direct arrival in the total wavefield at the virtual source location with the total wavefield at the receivers. The time-windowed direct arrival is obtained by placing a time gate of 400 ms around the direct arrival. Correlating the time-windowed direct arrival makes the virtual source gather cleaner but the strongest reflection is still the free-surface multiple (labeled as "multiple"). To further improve the virtual source gather quality, the up-down separation is combined with the time-windowing approach. As shown in figure 4.11(b), if the direct arrival, time-windowed in the downgoing waves at the virtual source location, is correlated with the upgoing waves at the receiver, the virtual source gather is cleaner and the true subsurface response (highlighted by the arrow and labeled as "primary") is clearly visible in the absence of the free-surface multiples. The free-surface multiple (labeled as "multiple?") is attenuated because only the upgoing energy are used for correlation at the receivers. The early-time reflections are crisper in figure 4.11(b) than in figure 4.11(a) because time-windowing the direct arrival in the downgoing waves is a cleaner approach. By time-windowing the direct arrival in the downgoing waves any contamination of the upgoing waves, that may have be present while time-windowing the direct arrival in the total wavefield, is suppressed.

The virtual source gather shown in figure 4.11(b) contains an incoherent jitter in the near offset around 3 to 4 s. In figure 4.10(a) this incoherent jitter does not show up when the full wavefield of the hydrophone is used for correlation. This incoherent jitter is the result of the wave scattering near the soft sea bottom. These scattered and mode-converted waves are sensed by the vertical component and show up in the virtual source gather when the vertical component is included for up-down wavefield separation. Schalkwijk, et al. (2003) studied a similar decomposition of multicomponent ocean-bottom seismic waves into downgoing and upgoing energy. They explain this jitter as the cross-coupling of the vertical component with the horizontal components, and they show that these events deteriorate the decomposition result if they are not removed. Schalkwijk, et al. (1999) proposed to remove the cross-coupling by optimally subtracting the horizontal velocity components from the vertical component.

The combination of wavefield separation and time-windowing, hence, produces the best of the responses [figure 4.11(b)], as predicted by synthetic modeling. While wavefield separation restricts the radiation pattern of the virtual source to be strictly downward, additional time-window imposes a P-wave virtual source and thus improves signal-to-noise ratio by eliminating unwanted shear-wave energy from the virtual source. This unwanted late energy might be used to generate virtual shear sources (Bakulin and Calvert, 2005).
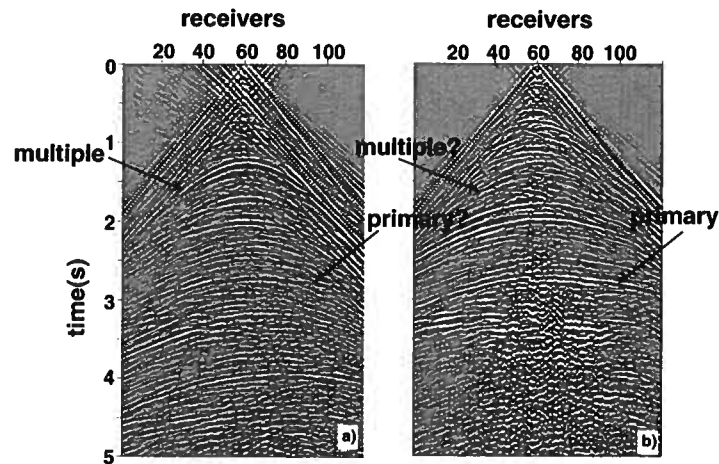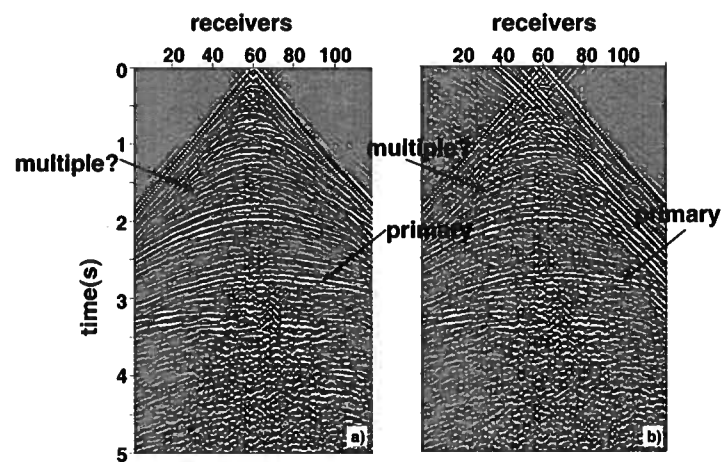
Figure 4.12. Virtual source gathers generated with receiver 60 as the virtual source. Figure (a) shows the virtual source gather generated by correlating the direct arrival time-windowed in the downgoing waves at the virtual source location with the upgoing waves at the receivers. Figure (b) shows the virtual source gather generated by summing the virtual source gathers generated for hydrophone and vertical component geophone : each of which is generated separately by correlating the direct arrival time-windowed in the total wavefield at the virtual source location with the total wavefield at the receivers. The label "multiple" refers to the reflection from the free-surface (overburden) and the label "primary" refers to the reflection from the subsurface. The label "multiple?" refers to the absence of the free-surface multiple.

Dual-sensor summation is strictly valid for zero-offset data over horizontally layered media. Therefore in many practical instances of large offsets or complex overburden structure in two or three dimensions it may fail to deliver separated wavefields with undistorted phase as required for virtual source generation. In cases such as for borehole observations below near surface, an alternative approach can be attempted to unravel an improved reflection response of the subsurface. First, one can generate two virtual source datasets using the current practice, i.e. correlating the direct arrival, time-windowed in the total wavefield at the virtual source (VS), with the total wavefield at the receivers, both for the hydrophone (VS_H) and vertical component geophone (VS_Z) separately, and then extract the upgoing waves $(VS_H + VS_Z)$ for the downhole survey using dual-sensor summation with the virtual source data. Figure 4.12(b), generated by such an alternative approach, reveals a gather similar in quality to our best response as depicted in figure 4.12(a) [same as figure 4.11(b)]. In figure 4.12(b), however, are distortions in early times and near the direct arrival because of time-windowing in the total wavefield instead of time-windowing in the downgoing waves. As shown before, wavefield separation in the process of generating the virtual source gathers indeed gives the true subsurface response. This alternative approach with wavefield separation after generating the virtual source data, however, also gives reasonable reflection response and can be improved further by suitable combination of three component (3-C) sources and 4-C geophones, i.e. by generating an elastic (vector) virtual source.

The up-down wavefield separation applied to the virtual source method suppresses the downgoing reflections and multiples from the overburden shown in the figure 2.30. There are, however, waves that propagate downwards from the virtual source, reflect from the subsurface, propagate through the overburden and reflect back into the subsurface and are then sensed by the receivers as upgoing waves. Such downgoing reflections and multiples from the overburden are present in the virtual source data even after applying wavefield separation to the virtual source method.

The next chapter demonstrates the usefulness of the virtual source method for time-lapse monitoring, especially after incorporating wavefield separation. By incorporating wavefield separation in the virtual source method, the sources of non-repeatability due to the time-varying overburden and acquisition discrepancy is suppressed. The next chapter also focuses on the importance of deconvolving the correlation gather by the source power spectrum, to suppress the variations in the source signature.

Chapter 5

Deconvolution interferometry to extract near-surface properties for a lossy layered medium

5.1 Summary

The virtual source method estimates the Green's function between a pair of receivers by using correlation. When the two wavefields recorded by the receivers are correlated, the resultant wavefield contains the power spectrum of the source-time function convolved with the estimate of the Green's function between the receivers. For an impulse source, the correlation gather can be deconvolved by the source power spectrum. When the source-time function is, however, long and difficult to estimate (e.g., earthquake or other passive seismic recording), deconvolution becomes a preferred seismic interferometric tool. When the recorded wavefields are deconvolved, instead of being correlated, the resultant wavefield is independent of the source-time function. In this chapter, deconvolution is applied to earthquake waves recorded in a borehole to extract the near-surface properties such as 1-D velocity profile. Furthermore, a connection is established between the deconvolved waveforms and the elements of the propagator matrix. Using the same earthquake recording, a P-to-S mode conversion is characterized by extending the application of the receiver function to downhole measurements.

5.2 Introduction

The virtual source method uses correlation as a tool for estimating the Green's function between a pair of receivers. Instead of correlation, deconvolution can also be used as a seismic interferometric tool (Snieder and Şafak, 2006; Vasconcelos and Snieder, 2006; Elgamal et al., 1995; Kawakami and Haddadi, 1998; Haddadi and Kawakami, 1998a; Haddadi and Kawakami, 1998b; Kawakami and Oyunchimeg, 2003; Vasconcelos and Snieder, 2007a; Vasconcelos and Snieder, 2007b; Vasconcelos and Snieder, 2007c; Vasconcelos, et al., 2007a; Vasconcelos, et al., 2007b), especially when the source-time function is too long and difficult to estimate. Snieder and Şafak (2006) used deconvolution as a seismic interferometric tool to extract the building response from the incoherent motion of the building. Snieder, et al. (2006b) showed that the deconvolved waves are also the solution of the same wave equation but with different boundary conditions.

Following the work of Snieder and Şafak (2006), this chapter focuses on the application of deconvolution to earthquake recording in a borehole in order to extract near-surface

properties. Near-surface properties are useful in quantifying seismic hazards. These properties are important for applications such as civil engineering and groundwater detection. The variability of near-surface properties is caused by changes in porosity, permeability, fractures, fluids, compaction, diagenesis and metamorphism (Toksöz et al., 1976). Lateral and temporal variations in near-surface properties is a major cause of poor repeatability of the source radiation pattern (Aritman, 2001), and hence reduces the repeatibility of time-lapse surveys. Knowledge of these near-surface properties is, hence, crucial for time-lapse monitoring. The local near-surface properties are also required to determine the free-surface reflectivity, which is useful to perform wavefield decomposition (Dankbaar, 1985; Wapenaar, et al., 1990). Estimation of the near-surface properties for a lossless homogeneous medium using propagator matrix and wave equation inversion is shown for SH waves by Trampert, et al. (1993) and for P-SV waves by van Vossen, et al. (2004).

Here I apply deconvolution to borehole recording of earthquake data to estimate the near-surface properties. Deconvolution of the incoherent waveforms recorded by the sensors at different depths in the borehole with the recording at the surface result in waves that propagate upward and downward along the array. These waves obtained by deconvolution can be used to estimate near-surface properties such as 1-D P- and S-wave velocity profiles. To get the near-surface properties using deconvolution, it is required to have recording in a borehole with two or more downhole sensors. This method is limited to linear systems and hence cannot be applied in the presence of non-linearity.

Following the study by van Vossen, et al. (2004), I establish a connection between the waveforms obtained after deconvolution and the elements of the propagator matrix. Further, the analysis is extended to a lossy layered medium for the special case of normal incidence.

In the process of deconvolution applied to different components, I observe a P-to-S mode conversion. The receiver function, defined as the spectral ratio of the radial component and the vertical component (Phinney, 1964; Langston, 1977; Ammon, 1991; Sheehan, et al., 1995; Dueker and Sheehan, 1998; Ramesh, et al., 2002; Gilbert, et al., 2003; Wilson and Aster, 2003; Wilson, et al., 2005), is a useful tool for characterizing converted waves. The ratio of the radial spectrum to the vertical spectrum depends on the structure beneath the surface (Phinney, 1964; Wilson, et al., 2005), notably in the presence of discontinuities. As the earthquake body waves travel through the earth, they produce a sequence of reflections, refractions, and conversions (e.g. from P to S waves) at discontinuities and rapid transition zones separating regions of differing seismic impedance. The receiver function emphasizes P-to-S converted phases from such interfaces while removing source complexity through the deconvolution of radial component seismograms by corresponding vertical component seismograms (Wilson, et al., 2005). Receiver functions applied to the surface data are routinely used to obtain detailed crustal and upper mantle structure (e.g., Clouser and Langston, 1995).

In the final section, I extend the application of the receiver function to downhole measurements in order to characterize the P-to-S mode conversion observed in the borehole recording of the earthquake waves.
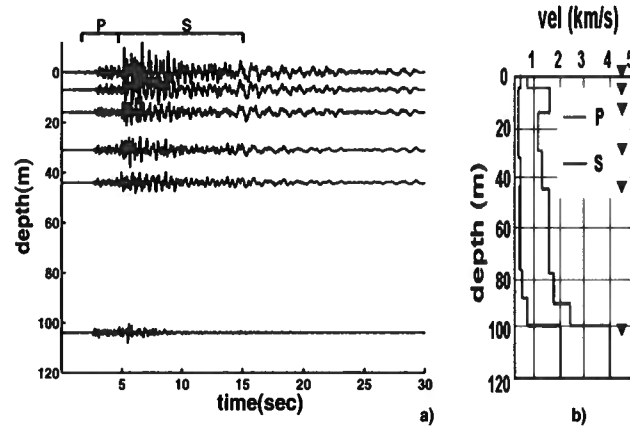
Figure 5.1. Figure (a) shows the acceleration recording of the radial component of the ground motion recorded by the Treasure Island array near San Francisco during the Richmond earthquake in 1994. The array consists of six 3-component sensors located at depths of 0, 7, 16, 31, 44, 104 m. The time windows used for time-windowing the P-waves (1.0 to 4.5 seconds) and the S-waves (4.5 to 15.0 seconds) is shown on the top. Figure (b) shows the 1-D velocity profile of the subsurface (Graizer and Shakal, 2004) down to 120 m. The triangles show the locations of the downhole sensors.

5.3 Earthquake Data Recorded by Treasure Island Array

Downhole arrays of triaxial accelerometers have been installed in California by the California Strong Motion Instrumentation Program (CSMIP). A geotechnical array, known as the Treasure Island array (Shakal, et al., 2004), was installed in San Francisco Bay by CSMIP in co-operation with other agencies (Graizer, et al., 2000). The array was installed in 1992 in an area that experienced liquefaction during the Loma Prieta earthquake in 1989. It recorded waveforms excited by an earthquake on 06/26/94 at 08:42:50.31 (UTC). The earthquake occurred near Richmond, CA and hence, in this paper, is referred to as the Richmond earthquake. It was a 4.0 magnitude earthquake with focal depth of 6.6 km and epicentral distance of 12.6 km from the sensors in the borehole. The downhole Treasure Island array had six 3-component sensors located at different depths, with the deepest one at a depth of 104 m. Each of the sensors is located in a different borehole separated by a horizontal distance of 3 m. Graizer, et al. (2000) analyzed these data to study site amplification as a function of depth. Figure 5.1(a) shows the radial component of the acceleration recording of the raw data. Figure 5.1(b) shows the P- and the S-wave velocity profile down to the deepest sensor. The triangles indicate the depths at which the sensors are located. In this study, the analysis is restricted to the body waves that arrive in the time windows in figure 5.1(a) that are labeled as 'P' and 'S'.

Figure 5.2. Upgoing and downgoing waves obtained by deconvolving the waveforms in the S-wave time-window of the transverse component of each of the sensors with the waveforms in the S-wave time-window of the transverse component of the sensor on the surface [equation (5.2)]. The sloping dashed lines show the traveltime curve of the upgoing and the downgoing S-waves computed from the S-wave velocity (β) model from Graizer and Shakal (2004).

5.4   Deconvolution and Propagator Matrix

Deconvolution of two signals $A(\omega)$ and $B(\omega)$ is, in the frequency domain, given by

$$D(\omega) = \frac{A(\omega)}{B(\omega)}. \qquad (5.1)$$

The deconvolution would be unstable because of zeros of the spectrum of $B(\omega)$. To avoid this instability, a regularized deconvolution can be given by

$$D(\omega) = \frac{A(\omega)B^*(\omega)}{|B(\omega)|^2 + \epsilon}, \qquad (5.2)$$

where the asterisk denotes complex conjugate and ϵ refers to a constant added at the denominator to prevent the instability of the equation (5.1). For our analysis ϵ is chosen to be 1% of the average spectral power of $B(\omega)$.

For the Richmond earthquake data, the waveforms recorded at each of the sensors are deconvolved with the waveforms recorded by the sensor on the surface. Since all three components of the ground motion are recorded at the Treasure Island array, deconvolution is applied to all three components. For the analysis of the three components, the waves arriving in the P- and the S- wave time-windows are deconvolved separately. Figure 5.1(a) shows the time-windows used for defining P waves (1.0 to 4.5 s) and S waves (4.5 to 15.0 s) before applying seismic interferometry.

Figure 5.2 shows the transverse component of the waveforms after deconvolving the waves in the S-wave time-window of the transverse component at each level with the waves
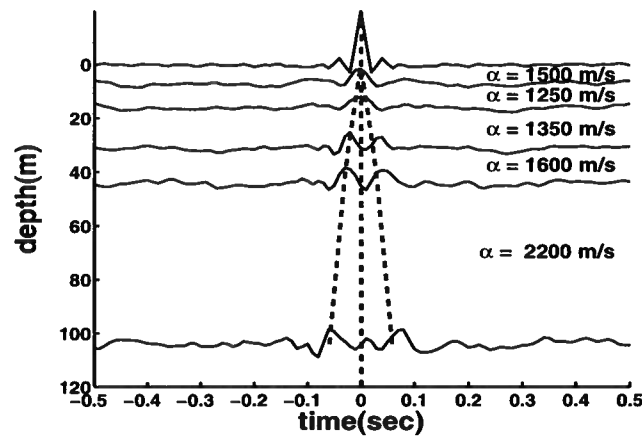
Figure 5.3. Upgoing and downgoing waves obtained by deconvolving the waveforms recorded by the vertical component of each of the sensors with the waveforms recorded by the vertical component of the sensor on the surface [equation (5.2)]. The sloping dashed lines show the traveltime curve of the upgoing and the downgoing P-waves computed from the P-wave velocity (α) model from Graizer and Shakal (2004).

in the S-wave time-window of the transverse component at the surface. The deconvolved waves show an upgoing and a downgoing wave. In order to highlight the waveforms at deeper sensors, the trace amplitudes are normalized with the maximum. Graizer and Shakal (2004) show the 1-D profile of the P-wave velocity and the S-wave velocity at the Treasure Island array location using suspension logging and classical downhole measurements (performed by the USGS), as shown in figure 5.1(b). In figure 5.2, the traveltime curve (sloping dashed lines) is also shown for upgoing and downgoing S-waves inferred from the velocity models of figure 5.1(b). Different slopes of the traveltime curve at different depths result from changes in the shear wave velocity at these depths. This suggests that the structure around the Treasure Island array is heterogeneous. The traveltime curve agrees with the upgoing and the downgoing wave obtained by deconvolution.

For the vertical component, deconvolution is applied to the waves in both the P- and the S-wave time-window. Figure 5.3 shows the waveforms after deconvolving the waves recorded at each of the sensors with the waves recorded at the sensor on the surface. Similar to figure 5.2, there is an upgoing and a downgoing wave, but they propagate with velocity higher than that of the deconvolved waves in figure 5.2. The traveltime curve (sloping dashed lines) is shown for upgoing and downgoing P-waves inferred from this model using the 1-D velocity profile for P-waves shown in figure 5.1(b). These traveltimes agree with the upgoing and the downgoing wave obtained by deconvolution.

Similar to the transverse component, deconvolution of the waves recorded by the radial component at each of the sensors with the waves recorded at the sensor on the surface also results in an upgoing and a downgoing wave. When the waves in the S-wave time-window are used for deconvolution, it results in an upgoing and a downgoing S-wave shown in
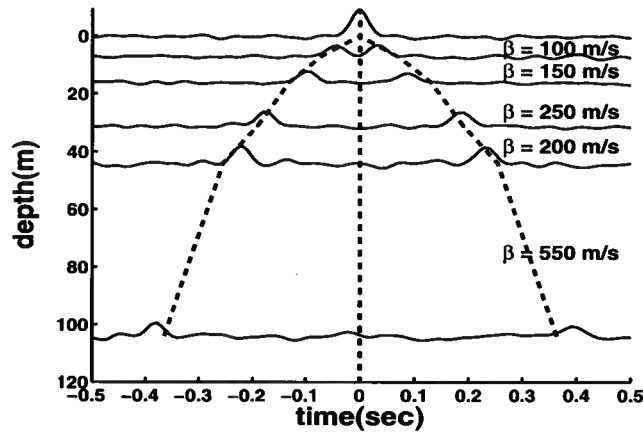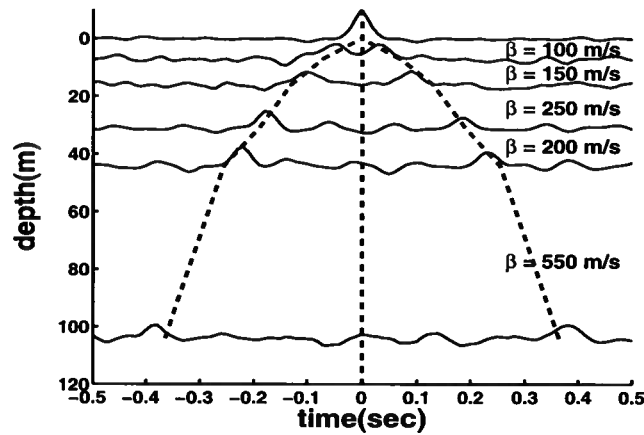
Figure 5.4. Upgoing and downgoing waves obtained by deconvolving the waveforms in the S-wave time-window of the radial component of each of the sensors with the waveforms in the S-wave time-window of the radial component of the sensor on the surface [equation (5.2)]. The sloping dashed lines show the traveltime curve of the upgoing and the downgoing S-waves computed from the S-wave velocity (β) model from Graizer and Shakal (2004).

figure 5.4. The sloping dashed lines that represents the S-wave traveltime curve agrees well with these upgoing and downgoing waves. The agreement of the traveltime curve with the wave propagation obtained by deconvolution for all the three components suggest that deconvolution can be used to extract near-surface properties such as 1-D P- and S-wave velocity profile.

The P- and S-wave velocities are extracted by deconvolving the waves recorded by a given component at different depths with the same component recording at the surface ($z=0$). Deconvolution of waves recorded at different depths with the sensor located at a different depth ($z\neq0$) also gives upgoing and downgoing waves propagating with P- or S-wave velocity, depending on the component and the time-window (Snieder, et al., 2006b). Similar analysis for multiple recordings at the borehole sensors can be used to get better confidence in the results and estimate on the uncertainty in the 1-D P- and the S-wave velocity. Along with the velocity estimation using the traveltimes, comparison of the amplitudes of the upgoing and the downgoing wave at the same depth can be used to estimate the quality factor, a measure of seismic attenuation.

5.4.1   Analysis with Propagator Matrix

The signal obtained by correlating two waveforms recorded at different receivers represents the filtered version of the sum of causal and acausal Green's function that characterizes the wave propagation between the two receivers (Lobkis and Weaver, 2001; Derode, et al., 2003; Schuster, et al., 2004; Shapiro and Campillo, 2004; Snieder, 2004; Wapenaar, 2004; Shapiro, et al., 2005; Wapenaar, et al., 2005; Snieder, et al., 2006a). If instead, the two

signals are deconvolved, as in our analysis of the Richmond earthquake data, what do the resultant waveforms represent? To address this question, the connection between the upgoing and the downgoing waves obtained by deconvolution and propagator matrix analysis for SH waves is shown by Trampert, et al. (1993). For a general layered medium with one of the sensors in a borehole (depth z) and another one at the free-surface (z=0), the displacement-stress vector for an SH wave at a depth z is expressed as matrix multiplication of the propagator matrix with the displacement-stress vector at the free-surface (z=0) (Aki and Richards, 2002). Since the traction at the free-surface is zero, this matrix multiplication can be written as

$$\begin{pmatrix} u_y(z,\omega) \\ \sigma_{yz}(z,\omega) \end{pmatrix} = P^{SH}(z,0) \begin{pmatrix} u_y(z=0,\omega) \\ 0 \end{pmatrix}. \tag{5.3}$$

This is a system of two equations. The first equation can be solved for the SH propagator matrix element as

$$P_{11}^{SH}(z,0) = \frac{u_y(z,\omega)}{u_y(z=0,\omega)}. \tag{5.4}$$

The right hand side of equation (5.4) represents deconvolution in frequency domain. Hence, for SH waves, deconvolution of the waveforms recorded at a depth with the waveforms recorded at the surface gives the P_{11} element of the propagator matrix (Trampert, et al., 1993). Does this also hold true for the P-SV waves? To answer this, let us consider the frequency domain analysis using propagator matrices by van Vossen, et al. (2004). Since one of the sensors is at the free-surface, the tractions at that sensor vanish. Using this property, they combine the $PSV_{(4*4)}$ and $SH_{(2*2)}$ propagator matrices to give

$$\begin{pmatrix} u_x(z,\omega) \\ u_y(z,\omega) \\ u_z(z,\omega) \end{pmatrix} = P(z,0) \begin{pmatrix} u_x(z=0,\omega) \\ u_y(z=0,\omega) \\ u_z(z=0,\omega) \end{pmatrix}, \tag{5.5}$$

where

$$P(z,0) = \begin{pmatrix} P_{11}^{PSV}(z,0) & 0 & iP_{12}^{PSV}(z,0) \\ 0 & P_{11}^{SH}(z,0) & 0 \\ -iP_{21}^{PSV}(z,0) & 0 & P_{22}^{PSV}(z,0) \end{pmatrix}. \tag{5.6}$$

In equation (5.6), $P_{ij}^{PSV/SH}$ stands for ij-element of the $PSV_{(4*4)}$ or $SH_{(2*2)}$ propagator matrix. A derivation of combining the P-SV and the SH propagator matrices to give equation (5.6) is shown in Appendix A.

In Appendix B a derivation is shown of the expressions given by van Vossen, et al. (2004) to express the propagator matrix elements in the measured displacements. The analysis of van Vossen et al. (2004) is, however, limited to a homogeneous lossless medium. To establish the connection between the deconvolved waveforms obtained from the Richmond earthquake and the elements of the propagator matrix, I extend their analysis to a lossy medium.

In the presence of attenuation (Johnston and Toksöz, 1981) the propagator matrix

elements for a homogeneous medium can be expressed as (Aki and Richards, 2002)

$$
\begin{aligned}
P_{11}^{SH}(z,0) &= \exp[i\omega q_s z - \xi_s z] + \exp[-i\omega q_s z + \xi_s z] \\
&= 2\cos[(\omega q_s + i\xi_s)z],
\end{aligned}
\tag{5.7}
$$

$$
\begin{aligned}
P_{11}^{PSV}(z,0) &= 2\beta^2 p^2 [\cos \omega q_p z \cosh \xi_p z - i \sin \omega q_p z \sinh \xi_p z] \\
&+ (1 - 2\beta^2 p^2)[\cos \omega q_s z \cosh \xi_s z - i \sin \omega q_s z \sinh \xi_s z] \\
&= 2\beta^2 p^2 \cos[(\omega q_p + i\xi_p)z] + (1 - 2\beta^2 p^2)\cos[(\omega q_s + i\xi_s)z],
\end{aligned}
\tag{5.8}
$$

$$
\begin{aligned}
iP_{12}^{PSV}(z,0) &= \frac{p}{q_p}(1 - 2\beta^2 p^2)[\cos \omega q_p z \sinh \xi_p z - i \sin \omega q_p z \cosh \xi_p z] \\
&- 2\beta^2 p q_s [\cos \omega q_s z \sinh \xi_s z - i \sin \omega q_s z \cosh \xi_s z] \\
&= \frac{-ip}{q_p}(1 - 2\beta^2 p^2) \sin[(\omega q_p + i\xi_p)z] + 2i\beta^2 p q_s \sin[(\omega q_s + i\xi_s)z],
\end{aligned}
\tag{5.9}
$$

$$
\begin{aligned}
-iP_{21}^{PSV}(z,0) &= \frac{-p}{q_s}(1 - 2\beta^2 p^2)[\cos \omega q_s z \sinh \xi_s z - i \sin \omega q_s z \cosh \xi_s z] \\
&- 2\beta^2 p q_p [\cos \omega q_p z \sinh \xi_p z - i \sin \omega q_p z \cosh \xi_p z] \\
&= \frac{ip}{q_s}(1 - 2\beta^2 p^2) \sin[(\omega q_s + i\xi_s)z] - 2i\beta^2 p q_p \sin[(\omega q_p + i\xi_p)z],
\end{aligned}
\tag{5.10}
$$

$$
\begin{aligned}
P_{22}^{PSV}(z,0) &= 2\beta^2 p^2 [\cos \omega q_s z \cosh \xi_s z - i \sin \omega q_s z \sinh \xi_s z] \\
&+ (1 - 2\beta^2 p^2)[\cos \omega q_p z \cosh \xi_p z - i \sin \omega q_p z \sinh \xi_p z] \\
&= 2\beta^2 p^2 \cos[(\omega q_s + i\xi_s)z] + (1 - 2\beta^2 p^2)\cos[(\omega q_p + i\xi_p)z],
\end{aligned}
\tag{5.11}
$$

where ω is the angular frequency, β the S-wave velocity, p the horizontal slowness, q_p the vertical slowness for P-waves, q_s the vertical slowness for S-waves, ξ_p the imaginary part of the vertical wavenumber for P-waves, and ξ_s the imaginary part of the vertical wavenumber for S-waves.

As shown in equations (5.7) through (5.11), for a lossy medium, both the vertical and the horizontal wavenumbers are complex. Complex horizontal wavenumber implies that the horizontal slowness and hence the velocity is complex and frequency-dependent. The associated dispersion is caused by the causality constraint in a lossy medium (Aki and Richards, 2002).

In the absence of attenuation, the propagator matrix elements are real. Therefore, P_{11}^{PSV}, P_{11}^{SH}, and P_{22}^{PSV} are real and iP_{12}^{PSV} and iP_{21}^{PSV} are imaginary. In Appendix B is shown how van Vossen, et al. (2004) use this to solve equation (5.5) for the propagator matrix elements. In the presence of attenuation, however, the propagator matrix elements are complex and hence cannot be determined from these three equations. More information is required to express elements of the propagator matrix as a function of the measured displacements. An important parameter in the expressions of the propagator matrix elements
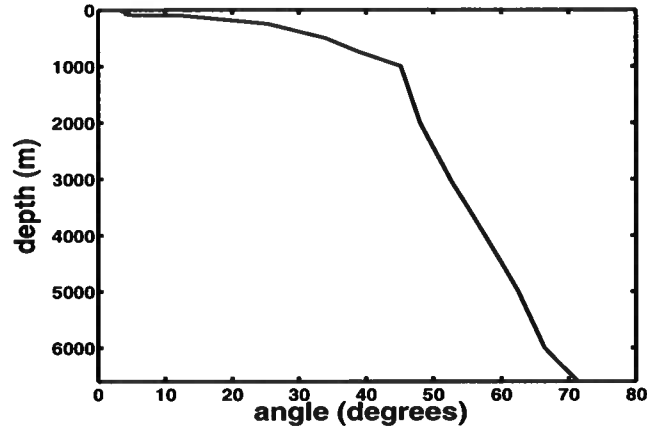
Figure 5.5. Angle of incidence as a function of depth.

is the horizontal slowness p, which depends on the angle of incidence. Using the velocity structure of the subsurface down to the hypocenter of the earthquake (Wald, et al., 1991), figure 5.5 shows the angle of incidence as a function of the depth. This figure shows that the waves arrive at the surface at near-normal incidence ($4°$). For normal incidence ($\theta \approx 0°$), the cross-terms P_{12}^{PSV} and P_{21}^{PSV} in the propagator matrix vanish.

$$P_{12}^{PSV}(z,0) \quad = \quad P_{21}^{PSV}(z,0) = 0. \tag{5.12}$$

Substituting equation (5.12) into equation (5.5) gives the following simplified linear system of equations:

$$\begin{pmatrix} u_x(z,\omega) \\ u_y(z,\omega) \\ u_z(z,\omega) \end{pmatrix} = \begin{pmatrix} P_{11}^{PSV}(z,0) & 0 & 0 \\ 0 & P_{11}^{SH}(z,0) & 0 \\ 0 & 0 & P_{22}^{PSV}(z,0) \end{pmatrix} \begin{pmatrix} u_x(z=0,\omega) \\ u_y(z=0,\omega) \\ u_z(z=0,\omega) \end{pmatrix}. \tag{5.13}$$

Solving the system of equation in (5.13) gives the propagator elements in terms of displacements.

$$P_{11}^{SH}(z,0) = \frac{u_y(z,\omega)}{u_y(z=0,\omega)}; \quad P_{11}^{PSV}(z,0) = \frac{u_x(z,\omega)}{u_x(z=0,\omega)}; \quad P_{22}^{PSV}(z,0) = \frac{u_z(z,\omega)}{u_z(z=0,\omega)}. \tag{5.14}$$

The first equation is the same as equation (5.4). The other two equations show that for vertically incident P-SV waves, the propagator matrix elements can be obtained by applying deconvolution. This holds true for an attenuative medium in just a special case of normal incidence. For the Treasure Island data, deconvolution is applied to get the upgoing and the downgoing waves. Equation (5.14) show that these deconvolved waves correspond to the

propagator matrix elements. In this analysis, one of the sensors is always at the free-surface where traction vanishes. If instead the waves recorded at a given depth are deconvolved with the waves recorded at a different depth ($z \neq 0$), the traction values are nonzero and should be incorporated in the analysis.

5.4.2   Extension to a Layered Medium

The connection between the waveforms obtained after deconvolution and the propagator matrix elements for a lossy homogeneous medium is established. The propagator matrix analysis can be extended to a layered medium. In this subsection I demonstrate the propagator matrix analysis for a medium consisting of two layers, which can be extended to a multi-layered medium. For the two-layer case with one of the sensors at a depth z and another one on the free-surface, the displacement and stress for an SH wave at a depth z is expressed as matrix multiplication of the product of propagator matrices corresponding to the two layers with the displacement and stress values at the free-surface ($z=0$) (Aki and Richards, 2002). Since the traction at the free-surface is zero, this matrix multiplication can be written as

$$\begin{pmatrix} u_y(z,\omega) \\ \sigma_{yz}(z,\omega) \end{pmatrix} = \begin{pmatrix} S_{11} & S_{12} \\ S_{21} & S_{22} \end{pmatrix} \begin{pmatrix} R_{11} & R_{12} \\ R_{21} & R_{22} \end{pmatrix} \begin{pmatrix} u_y(z=0,\omega) \\ 0 \end{pmatrix}, \qquad (5.15)$$

where the matrices $\mathbf{S}$ and $\mathbf{R}$ are the SH propagator matrices for each layer. The propagator matrices are multiplied to get

$$\begin{pmatrix} u_y(z,\omega) \\ \sigma_{yz}(z,\omega) \end{pmatrix} = \begin{pmatrix} (SR)_{11} & (SR)_{12} \\ (SR)_{21} & (SR)_{22} \end{pmatrix} \begin{pmatrix} u_y(z=0,\omega) \\ 0 \end{pmatrix}, \qquad (5.16)$$

which has the same form as equation (A.1) for SH waves. If $\mathbf{P}$ and $\mathbf{Q}$ are the P-SV propagator matrices for the two layers, expression for P-SV waves has the same form as equation (A.3). These SH and P-SV propagator matrices can be combined, as shown in Appendix A, to give

$$\begin{pmatrix} u_x(z,\omega) \\ u_y(z,\omega) \\ u_z(z,\omega) \end{pmatrix} = \begin{pmatrix} (PQ)_{11} & 0 & i(PQ)_{12} \\ 0 & (SR)_{11} & 0 \\ -i(PQ)_{21} & 0 & (PQ)_{22} \end{pmatrix} \begin{pmatrix} u_x(z=0,\omega) \\ u_y(z=0,\omega) \\ u_z(z=0,\omega) \end{pmatrix}, \qquad (5.17)$$

where

$$(SR)_{ij} = \sum_{k=1}^{2} S_{ik} R_{kj}, \qquad (5.18)$$

$$(PQ)_{ij} = \sum_{k=1}^{4} P_{ik} Q_{kj}. \qquad (5.19)$$

The combined matrix has the same form as equation (A.8) in Appendix A. Similar to the case of a homogeneous medium, for a lossless medium the diagonal elements are real and the off-diagonal elements are imaginary. Following the analysis in Appendix B, equation (5.17) can be solved for the propagator matrix elements that correspond to a combination of the propagator matrix elements for each layer as shown in equations (5.18) and (5.19).

For a lossy medium, the propagator matrix elements in equation (5.17) are complex valued. This makes it impossible to solve equation (5.17) for the five elements of the propagator matrix. For the homogeneous case an assumption of normal incidence simplifies the underdetermined system in equation (5.5). For normal incidence, the P-SV propagator matrix for a homogeneous layer simplifies to

$$
P^{PSV} = \begin{pmatrix} P_{11} & 0 & P_{13} & 0 \\ 0 & P_{22} & 0 & P_{24} \\ P_{31} & 0 & P_{33} & 0 \\ 0 & P_{42} & 0 & P_{44} \end{pmatrix}.
\tag{5.20}
$$

If the P-SV propagator matrix is used for vertically incident waves shown in equation (5.20) for multiplication, the terms $(PQ)_{12}$ and $(PQ)_{21}$ in equation (5.17) vanish. Hence, the system of equations simplifies to

$$
\begin{pmatrix} u_x(z,\omega) \\ u_y(z,\omega) \\ u_z(z,\omega) \end{pmatrix} = \begin{pmatrix} (PQ)_{11} & 0 & 0 \\ 0 & (SR)_{11} & 0 \\ 0 & 0 & (PQ)_{22} \end{pmatrix} \begin{pmatrix} u_x(z=0,\omega) \\ u_y(z=0,\omega) \\ u_z(z=0,\omega) \end{pmatrix},
\tag{5.21}
$$

where, for a two layer case, the diagonal terms of the matrix in equation (5.21) simplify, because of normal incidence, to

$$
\begin{aligned}
(PQ)_{11} &= P_{11}Q_{11} + P_{13}Q_{31}, \\
(SR)_{11} &= S_{11}R_{11} + S_{12}R_{21}, \\
(PQ)_{22} &= P_{22}Q_{22} + P_{24}Q_{42}.
\end{aligned}
\tag{5.22}
$$

Hence, for vertically incident waves in a layered medium, the propagator matrix similar to equation (5.13) can be obtained by combining the P-SV and SH propagator matrices, each of which is a combination of the corresponding propagator matrices for each layer, as shown in equation (5.22). If each of the layers is homogeneous and incidence is normal, the resultant matrix is diagonal and hence can be solved for the combination of the propagator matrix elements even in the presence of attenuation. Deconvolution applied to the waveforms recorded in a layered medium thus results in the propagator matrix elements of the matrix obtained by combining the P-SV and the SH matrices of the layered medium.

5.5 Characterizing Converted Waves using the Downhole Receiver Function

The waves in the S-wave time-window of the radial component at each sensor when deconvolved with the sensor on the surface results in an upgoing and a downgoing S-wave
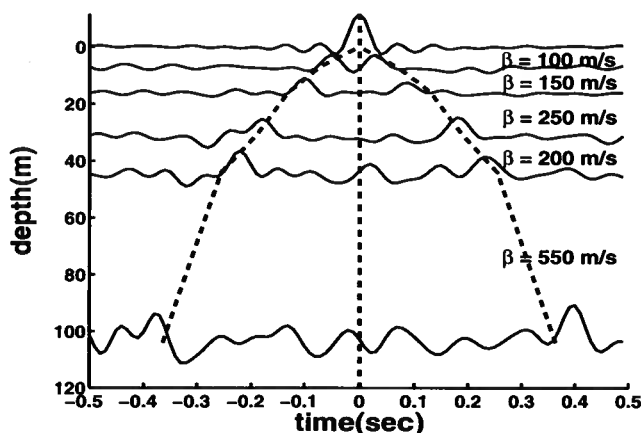
Figure 5.6. Upgoing and downgoing waves obtained by deconvolving the waveforms in the P-wave time-window of the radial component of each of the sensors with the waveforms in the P-wave time-window of the radial component of the sensor on the surface [equation (5.2)]. Interestingly, the sloping dashed lines show the traveltime curve of the upgoing and the downgoing S-waves computed from the S-wave velocity model from Graizer and Shakal (2004).

(figure 5.4). Figure 5.6 shows the waveforms obtained after deconvolving the waves in the P-wave time-window of the radial component at each sensor with the sensor on the surface. Interestingly, instead of propagating with the P-wave velocity, the deconvolved waves propagate with the S-wave velocity. One possible explanation for this interesting result is that there is a P-to-S conversion at a depth below the downhole array. The conversion would cause the waves before the primary S-wave in figure 5.1(a) to contain the P to S converted wave. The recordings in figure 5.1(a) show that both the incoming P and S waves are incoherent. The lack of coherency is caused by scattering along the path from the earthquake to the array. The same scattering could lead to the possible mode conversion observed.

The receiver functions (Phinney, 1964; Langston, 1977; Ammon, 1991; Sheehan, et al., 1995; Dueker and Sheehan, 1998; Ramesh, et al., 2002; Gilbert, et al., 2003; Wilson and Aster, 2003; Wilson, et al., 2005) are computed for the borehole recording of the earthquake waves to diagnose the upgoing P to S converted wave. The receiver function in a borehole is defined as the deconvolution of the waves recorded by the radial component at each of the sensor location with the waves recorded by the vertical component at the same sensor location. In the frequency domain, it is the spectral ratio of the radial component recorded at each of the sensor location in a borehole and the vertical component at the same sensor location.

Figure 5.7 shows receiver functions computed at each sensor location for the downhole data. Each trace is the deconvolution of the waves recorded by the radial component at a given depth by the waves recorded by the vertical component at the same depth. The
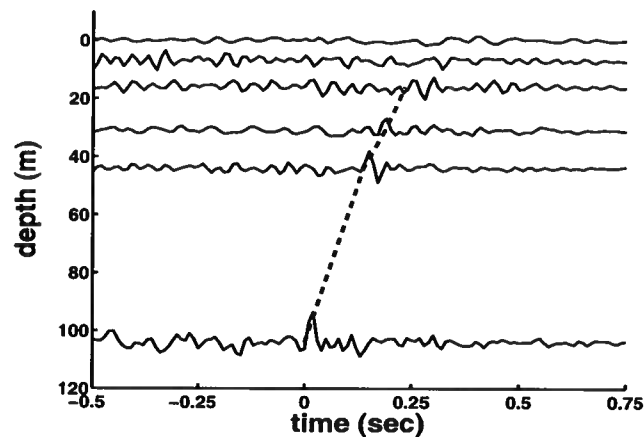
Figure 5.7. Receiver function, defined as the spectral ratio of the data recorded by the radial component with the data recorded by the vertical component at the same level. Each of the traces represent the deconvolution of the radial component at that specific sensor with the data recorded at the corresponding vertical component. The dashed line, computed from the P- and the S-wave velocity model of Graizer and Shakal (2004), shows the traveltime curve for a P to S converted wave with the conversion point just below the deepest sensor.

receiver functions show a distinct upgoing wave. The dashed line indicates the traveltime curve of the upgoing P-to-S converted wave calculated from the P- and the S-wave velocity model shown in figure 5.1(b) (Graizer and Shakal, 2004), assuming a P-to-S conversion at a depth just below the deepest sensor (104 m). The agreement of the upgoing wave in the receiver function and this traveltime curve support the hypothesis of a pronounced P-to-S conversion. Arrival of the pulse close to time t=0 at 104 m indicates that the conversion occurred just below the deepest sensor in the borehole. Graizer and Shakal (2004) show that the geology close to the depth of 104 m changes from unconsolidated sediments to Franciscan Bedrock Sandstone and Shale. The drastic variation in geology causes an increase in the P- and the S-wave velocity around this depth (as shown in figure 5.1(b)), hence resulting in the strong conversion.

In the next subsection, I use a synthetic model to support the idea of using receiver function to characterize the upgoing P-to-S converted wave for borehole data.

5.5.1   Analysis using Synthetic Model

The basic premise of the receiver function is that the vertical component is a reasonable representation of the incident wave. A borehole recording contains not only the incident waves from the earthquake (upgoing waves) but also reflections off the free-surface (downgoing waves). Hence, for the borehole sensors the receiver functions contain a complex series of phases with their timing and moveout determined by sensor depth and relative P- and S-wave traveltimes to the surface. To show that the first arrival in receiver function
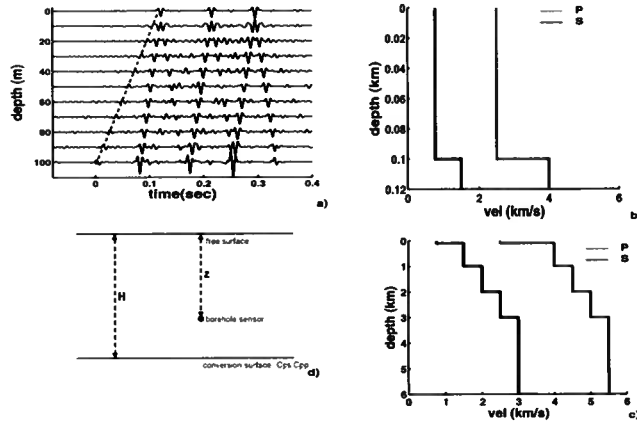
Figure 5.8. Figure (a) shows the receiver function computed for the synthetic model. The earlier arrival highlighted with the dashed line is the P-to-S converted wave. All the waves with other phases arrive at later times. Figure (b) shows the velocity profile down 100 m and figure (c) shows the velocity profile down to the source depth (6000 m). Figure (d) shows the cartoon of the model consisting of a homogeneous half space above an interface at a depth H. Borehole sensors are located in the homogeneous half space at a depth of z from the free-surface. The conversion coefficients at the conversion surface are denoted as C_{ps} and C_{pp}.

characterizes the P-to-S converted wave, I compute the receiver function for the synthetic model shown in figure 5.8(d). Borehole sensors are assumed to be placed from the surface (z=0) down to z=100 m spaced every 10 m. The velocity profiles down to the deepest receiver (100 m) and down to the source depth (6000 m) are shown in figures 5.8(b) and 5.8(c), respectively. The source is at a horizontal distance of 1000 m from the sensors.

The receiver function, in frequency domain, is given by

$$
\begin{aligned}
\frac{u_x(z,\omega)}{u_z(z,\omega)} &= \frac{C_{ps}e^{i\nu_\beta(H-z)} + \sum_j A_j e^{i\phi_j}}{C_{pp}e^{i\nu_\alpha(H-z)} + \sum_k B_k e^{i\psi_k}} \\[2mm]
&= \frac{C_{ps}e^{i\nu_\beta(H-z)}\left[1 + \frac{\sum_j A_j e^{i\phi_j}}{C_{ps}e^{i\nu_\beta(H-z)}}\right]}{C_{pp}e^{i\nu_\alpha(H-z)}\left[1 + \frac{\sum_k B_k e^{i\psi_k}}{C_{pp}e^{i\nu_\alpha(H-z)}}\right]} \\[2mm]
&= \frac{C_{ps}}{C_{pp}}e^{i(H-z)(\nu_\beta-\nu_\alpha)}\left[1 + \frac{\sum_j A_j e^{i\phi_j}}{C_{ps}e^{i\nu_\beta(H-z)}}\right]\left[1 + \frac{\sum_k B_k e^{i\psi_k}}{C_{pp}e^{i\nu_\alpha(H-z)}}\right]^{-1}, \\[2mm]
&= \frac{C_{ps}}{C_{pp}}e^{i(H-z)(\nu_\beta-\nu_\alpha)}\left[1 + \frac{\sum_j A_j e^{i\phi_j}}{C_{ps}e^{i\nu_\beta(H-z)}}\right]\left[\sum_{n=0}^{\infty}(-1)^n\left(\frac{\sum_k B_k e^{i\psi_k}}{C_{pp}e^{i\nu_\alpha(H-z)}}\right)^n\right],
\end{aligned}
$$

$$(5.23)$$

where

$$\phi_j > \nu_\beta(H - z),$$
$$\psi_k > \nu_\alpha(H - z). \tag{5.24}$$

H is the depth of the conversion surface, ν_β is the vertical wavenumber for S-waves and ν_α is the vertical wavenumber for P-waves. C_{ps} and C_{pp} are the P-S conversion coefficient and P-P transmission coefficient at the conversion surface. The first term of the receiver function [equation (5.23)] characterizes the P-to-S converted wave. The terms $A_j e^{i\phi_j}$ and $B_j e^{i\psi_j}$ denote waves that arrive after the P-to-S converted wave. Examples of these waves are the surface-reflected P-waves, multiple reflections and wave conversion between the free-surface and the velocity discontinuity. The receiver function for the synthetic model is shown in figure 5.8(a). Since the waves corresponding to terms $A_j e^{i\phi_j}$ and $B_j e^{i\psi_j}$ arrive at later times (as shown in figure 5.8(a)), the phase of these arrivals satisfies the inequalities in equation (5.24). These later arriving waves are present in the receiver function applied to the downhole data (figure 5.8(a)). The first arrival in the receiver functions applied to downhole data, however, characterizes the upgoing P-to-S converted wave and is highlighted by the dashed line.

Hence, the receiver function applied to borehole data contains a series of phases given by equation (5.23) that are difficult to interpret. The first arrival, however, represents the upgoing P-to-S converted wave.

Chapter 6

Discussions and Future Work

The virtual source method is a valuable tool for imaging and monitoring below the complex and time-varying overburden, without the knowledge of overburden velocities and near-surface changes. The virtual source data are generated by correlating the wavefield recorded at a reference receiver, which acts as the virtual source, with the wavefield recorded at all the other receivers and stacking the resultant correlation gather over the physical sources. The correlation gathers are useful for quality control and for assessing the source spacing and the physical sources that give a stationary phase contribution while stacking.

The maximum allowable source spacing to prevent spatial aliasing increases with increase in depth of receivers, increase in velocity above the downhole receivers, and decrease in the reflector depth. Similar to conventional seismic data, for the virtual source method the maximum allowable receiver spacing depends on the velocity below the downhole receivers, and the deepest reflector. The physical sources giving stationary phase contribution can be identified as extremas in the correlation gather.

While generating the virtual source data, tapering applied to the traces at the ends of the source aperture before stacking the correlation gather suppresses the edge effects caused by abrupt truncation of the stack over sources. The edge effects can be diagnosed using the traveltime difference curve for the sources at the two ends of the aperture. Artifacts due to the side-lobes of the auto-correlation of the source-time function can in principle be removed by deconvolving all the traces in the correlation gather with the power spectrum of the source signal before stacking over the sources. Other artifacts encountered in the generation of the virtual source gather include unphysical events due to incomplete source aperture and reflections and multiples coming from the overburden.

Wavefield separation helps improve the virtual source method by removing the limited acquisition aperture related spurious events and overburden-related multiples. Instead of correlating total wavefields as suggested by theory, in practical cases it is more beneficial to correlate the downgoing waves at the virtual source with the upgoing waves at the receivers. Selecting the downgoing waves at the virtual source suppresses the spurious events caused by incomplete acquisition aperture, by restricting the radiation pattern of the virtual sources to downward direction only. Using upgoing waves at the receivers eliminates the reflections from the overburden and the free-surface. Additional time-windowing of the direct arrival in the downgoing response allows restriction of the virtual source radiation pattern to predominantly P-waves and avoids contamination by shear wave energy. Combination of the the up-down wavefield separation and time-windowing the direct arrival in the downgoing waves, hence, provides a response in the absence of downgoing reflections

and multiples from the overburden.

The virtual source method is also a powerful tool for time-lapse monitoring provided that the receivers are placed below the time-varying overburden. Along with the subsurface changes, acquisition discrepancies between the base and the monitor survey include variation in the source location and source power spectrum. Other prominent undesirable changes include variations in the overburden such as changes in the sea water level, sea surface roughness, sea water temperature and salinity.

Wavefield separation applied to the virtual source method suppresses the reflections coming from the overburden, hence making the virtual source data independent of the overburden changes and variation in the source location. Time-windowing the direct arrival in the downgoing waves suppresses non-repeatability in the shear waves. Deconvolution of the correlation gather by the source power spectrum suppresses the variation in source power spectrum. Variations caused by the waves that are downgoing at the virtual source, upgoing at the receivers, and propagate through the overburden, however, still exist.

Deconvolution of the correlation gather by the source power spectrum is possible when the source is an impulse. For applications such as earthquake data as well as drill-bit seismic, estimation of the source-time function is difficult. For such cases, deconvolution is a preferred tool for seismic interferometry. When the wavefield recorded by two receivers are deconvolved the source-time function drops out making the resultant deconvolved signal independent of the source signature.

Deconvolution as a tool for seismic interferometry, applied to data recorded in 1-D by the Treasure Island array, results in a superposition of upgoing and downgoing P- and S-waves. This makes it a valuable tool in estimating the 1-D velocity profile along the recording array. Application of deconvolution to various components of the data results in waves propagating with either P- or S-wave velocity, and depends on the interval used for time-windowing before applying deconvolution. For both the transverse and radial components, deconvolution of the waves in the S-wave time-window results in the upgoing and downgoing waves with S-wave velocity. Deconvolution applied to the vertical component results in upgoing and downgoing waves with the P-wave velocity. Finally, I have established a connection of the resultant upgoing and downgoing waves with the propagator matrix elements. This type of analysis is possible even in the presence of attenuation as long as the waves arrive at normal incidence. The propagator matrix analysis extends to a layered medium. The analysis holds even for a layered medium in the presence of attenuation for the special case of normal incidence.

A P-to-S mode conversion is observed when deconvolution is applied to the waves in the P-wave time-window of the radial component. Deconvolution applied to the waves in the P-wave time-window of the radial component interestingly results in an upgoing and a downgoing wave propagating with the S-wave velocity. This is possible when the arrivals before the primary S-wave contain S-waves generated by P to S conversion. The receiver function applied to downhole data and synthetic modeling thereafter supports this observation of the mode conversion just below the deepest sensor in the borehole.

6.1 Future Work

The application of the virtual source method to the field data for time-lapse monitoring is in this work restricted to a homogeneous water layer as the overburden. For a complex overburden that varies more dramatically with time, however, the improvement in the time-lapse virtual source data will be more prominent than that in the time-lapse marine seismic data.

Correlation gather is a useful tool for estimating the maximum allowable source spacing and the sources that give the stationary phase contribution. The analysis in this work is demonstrated for a homogeneous water layer as the overburden. For a complicated overburden, the correlation gather could have multiple local maximas indicating the source locations giving stationary phase contributions. Complicated overburden helps the virtual source method in increasing the effective aperture due to scattering. It could also hinder the method if scattering results in lack of illumination at a given receiver location that could act as the virtual source.

For complicated time-varying overburden, wavefield separation using dual-sensor summation also becomes difficult because dual-sensor summation uses hydrophone and vertical component geophone to separate the upgoing and the downgoing waves strictly for normal incidence. For such complex overburden, separation of the wavefield in the virtual source data domain might be better than that in the raw data domain. Separation of the wavefield (into upgoing and downgoing waves) using dual sensor summation applied to the virtual source data may not result in reliable summation if the waves arrive at the receivers at large incidence angles. In such cases, instead of H+Z and H-Z, H+Z/$\cos\theta$ and H-Z/$\cos\theta$ gives better representation of the upgoing and downgoing waves respectively, where θ is the incidence angle at which the waves arrive at the receivers.

The up-down wavefield separation requires the vertical component geophone and the hydrophone. Use of the radial and the transverse component recordings can also be used appropriately to separate P and S waves. A combination of such wavefield separation can allow us to create a P- or an S-wave virtual source that can be either downward or upward radiating depending on the application.

Apart from using the dual-sensor summation technique, other methods such as f-k (frequency-wavenumber) analysis can also be used to separate waves propagating along the receiver array, provided that the receiver array is dipping. Vasconcelos et al. (2007b) used f-k analysis for wavefield separation applied to deconvolution interferometry.

The up-down wavefield separation applied to the virtual source data suppresses the first-order multiple coming from the overburden. Higher order multiples from the overburden, however, exists and cannot be suppressed by up-down wavefield separation. Such arrivals can be suppressed from the virtual source data by an inversion approach, where the objective is to create an impulse at the virtual source location using all the downgoing energy in the overburden.

The theory of seismic interferometry is not limited to the wave equation. Recent work by Wapenaar (Wapenaar and Slob, 2006; Slob and Wapenaar, 2007) and Snieder (Snieder, et al., 2007) have shown that it can be extended to diffused wavefields by using sources in a

volume instead of sources on the surface, thus extending the application of interferometry to applications such as electromagnetic exploration and pore pressure estimation.

References

Aki, K., & Richards, P. G. 2002. Quantitative Seismology. *University Science Books*, Sausalito, 2nd edition.

Ammon, C. J. 1991. The isolation of receiver effects from teleseismic P waveforms. *Bulletin of Seismological Society of America*, **81(6)**, 2504-2510.

Aritman, B. C. 2001. Repeatability study of seismic source signatures. *Geophysics*, **66**, 1811-1817.

Artman, B. 2006. Imaging passive seismic data. *Geophysics*, **71**, SI177-SI187.

Bakulin, A., & Calvert, R. 2004. Virtual source: new method for imaging and 4D below complex overburden. *74th Annual Meeting, SEG, Expanded Abstracts*, 2477-2480.

Bakulin, A., & Calvert, R. 2005. Virtual Shear Source: a new method for shear-wave seismic surveys. *75th Annual Meeting, SEG, Expanded Abstracts*, 2633-2636.

Bakulin, A., & Calvert, R. 2006. The virtual source method: theory and case study. *Geophysics*, **71**, SI139-SI150.

Ball, V., & Corrigan, D. 1996. Dual-sensor summation of noisy ocean-bottom data. *66th Annual Meeting, SEG, Expanded Abstracts*, 28-31.

Barr, F. J., & Sanders, J. I. 1989. Attenuation of Water-Column Reverberations using pressure and velocity detectors in a water-bottom cable. *59th Annual Meeting, SEG, Expanded Abstracts*, 653-656.

Barr, F. J., Paffenholz, J., & Rabson, W. 1996. The dual-sensor ocean-bottom cable method: Comparative geophysical attributes, quantitative geophone coupling analysis and other recent advances. *66th Annual Meeting, SEG, Expanded Abstracts*, 21-22.

Barr, F. J. 1997. Dual-sensor OBC technology. *The Leading Edge*, **16**, 45-52.

Barr, F. J., Chambers, R. E., Dragoset, W., & J. Paffenholz. 1997. A comparison of methods for combining dual-sensor ocean-bottom cable traces. *67th Annual Meeting, SEG, Expanded Abstracts*, 67-70.

Bender, C. M., & Orszag, S. A. 1978. Advanced Mathematical Methods for Scientists and Engineers. *McGraw-Hill Book Company*.

Blomgren, P., Papanicolaou, G., & Zhao, H. 2002. Super-resolution in time-reversal acoustics. *Journal of Acoustical Society of America*, **111**, 230-248.

Borcea, L., Tsogka, C., Papanicolaou. G., & Berryman, J. 2002. Imaging and time-reversal in random media. *Inverse Problems*, **18**, 1247-79.

Borcea, L., Papanicolaou, G., & Tsogka, C. 2003. Theory and applications of time reversal and interferometric imaging. *Inverse Problems*, **19**, S139-S164.

Calvert, R. W., Bakulin, A., & Jones, T. C. 2004. Virtual Sources, a new way to remove overburden problems. *66th Annual Meeting, EAGE, Expanded Abstracts*, P234.

Canales, L., & Bell, M. L. 1996. Ghost attenuation using dual sensor cable data. *66th Annual Meeting, SEG, Expanded Abstracts*, 1591-1594.

Clouet, J. F., & Fouque, J. P. 1997. A time-reversal method for an acoustical pulse propagating in randomly layered media. *Wave Motion*, **25**, 361-368.

Clouser, R. H., & Langston, C. A. 1995. Effect of sinusoidal interfaces on teleseismic P-wave receiver functions. *Geophysical Journal International*, **123**, 541-558.

Curtis, A., Gerstoft, P., Sato, H., Snieder, R., & Wapenaar K. 2006. Seismic interferometry - turning noise into signal. *The Leading Edge*, **25**, 1082-1092.

Dankbaar, J. W. M. 1985. Separation of P- and S-waves. *Geophysical Prospecting*, **33**, 970-986.

Derode, A., Lacrose, E., Campillo, M., & Fink, M. 2003. How to estimate the Green's function for a heterogeneous medium between two passive sensors? Application to acoustic waves. *Applied Physics Letters*, **83**, 3054-3056.

Draganov, D., Wapenaar, K., & Thorbecke, J. 2006. Seismic interferometry: Reconstructing the earth's reflection response. *Geophysics*, **71(4)**, SI61-SI70.

Dragoset, W., & Barr, F. J. 1994. Ocean-bottom cable dual-sensor scaling. *64th Annual Meeting, SEG, Expanded Abstracts*, 857-860.

Dueker, K. G., & Sheehan, A. F. 1998. Mantle discontinuity structure beneath the Colorado Rocky Mountains and High Plains. *Journal of Geophysical Research*, **103**, 7153-7169.

Elgamal, A. W., Zeghal, M., Tang, H. T., & Stepp, J. C. 1995. Lotung Downhole Array, I: Evaluation of site dynamic properties. *Journal of Geotechnical Engineering*, **121(4)**, 350-362.

Fink, M. 1993. Time reversal mirrors. *Journal of Physics D: Applied Physics*, **26**, 1333-1350.

Fink, M. 1999. Time-reversed acoustics *Scientific American*, November 1999, 67-93.

Gilbert, H. J., Sheehan, A. F., Dueker, K. G., & Molnar, P. 2003. Receiver functions in the western United States, with implications for upper mantle structure and dynamics. *Journal of Geophysical Research*, **108(B5)**, 2229, doi:10.1029/2001JB001194.

Graizer, V., Cao, T., Shakal, A., & Hipley, P. 2000. Data from downhole arrays instrumented by the California Strong Motion Instrumentation Program in studies of site amplification effects. *Proceedings of the 6th International Conference on Seismic Zonation*, Palm Springs, California.

Graizer, V., & Shakal, A. 2004. Analysis of some of CSMIP strong-motion geotechnical array recordings. *Proceedings of the International Workshop for Site Selection, Installation and Operation of Geotechnical Strong-Motion Arrays: Workshop 1, Inventory of Current and Planner Arrays*, 14 and 15 October 2004, COSMOS, SCEC and USC.

Haddadi, H. R., & Kawakami, H. 1998. Modeling wave propagation by using normalized input-output minimization (NIOM) method for multiple linear systems. *Journal of Structural, Mechanical and Earthquake Engineering*, 15(1), 29s-39s.

Haddadi, H. R., & Kawakami, H. 1998. Characteristics of Vertical Component Strong Ground Motion by NIOM (Normalized Input-Output Minimization) Method. *Proceedings of 10th Japan Symposium of Earthquake Engineering*, 1187-1192.

Haider, M. A., Mehta, K. J., & Fouque, J. P. 2004. Time-reversal numerical simulations for randomly layered media. *Waves in Random Media*, 14, 185-198.

Jiao, J., Trickett, S., & Link, B. 1998. Robust summation of dual-sensor ocean-bottom cable data. *68th Annual Meeting, SEG, Expanded Abstracts*, 1421-1424.

Johnston, D. H., & Toksöz, M. N. 1981. Definitions and Terminology. *Geophysics Reprint Series No.2: Seismic Wave Attenuation*, 1-5.

Karl, J. H. 1989. An Introduction to Digital Signal Processing. *Academic Press*, San Diego, CA, ISBN 0-12-398420-3.

Kawakami, H., & Haddadi, H. R. 1998. Modeling wave propagation by using normalized input-output minimization (NIOM). *Soil Dynamics and Earthquake Engineering*, 17, 117-126.

Kawakami, H., & Oyunchimeg, M. 2003. Normalized input-output minimization analysis of wave propagation in buildings. *Engineering Structures*, 25, 1429-1442.

Korneev, V., & Bakulin, A. 2006. On the fundamentals of the virtual source method. *Geophysics*, 71, A13-A17.

Langston, C. A. 1977. Corvallis, Oregon, crustal and upper mantle receiver structure from teleseismic P-waves and S-waves. *Bulletin of Seismological Society of America*, 67, 713-724.

Larose, E., Margerin, L., Derode, A., van Tiggelen, B., Campillo, M., Shapiro, N., Paul, A., Stehly, L., & Tanter, M. 2006. Correlation of random wavefields: an interdisciplinary review. *Geophysics*, 71, SI11-SI21.

Lobkis, O. I., & Weaver, R. L. 2001. On the emergence of the Green's function in the correlations of a diffuse field. *Journal of Acoustical Society of America*, **110**, 3011-3017.

Loewenthal, D. 1994. On dual field measurements using geohydrophones. *64th Annual Meeting, SEG, Expanded Abstracts*, **13**, 861-864.

Loewenthal, D., & Robinson, E. A. 2000. On unified dual fields and Einstein deconvolution. *Geophysics*, **65**, 293-303.

Mehta, K., & Snieder, R. 2006. Time reversed imaging for perturbed media. *American Journal of Physics*, **74**, 224-231.

Mehta, K., Snieder, R., Calvert, R., & Sheiman, J. 2006. Virtual source gathers and attenuation of free-surface multiples using OBC data : implementation issues and a case study. *76th Annual Meeting, SEG, Expanded Abstracts*, 2669-2673.

Mehta, K., & Snieder, R. 2007. Source spacing for the virtual source method. *The Leading Edge*, In preparation.

Mehta, K., Snieder, R., & Graizer, V. 2007. Extraction of near-surface properties for a lossy layered medium using the propagator matrix. *Geophysical Journal International*, **169**, 271-280.

Mehta, K., Bakulin, A., Sheiman, J., Calvert, R., & Snieder, R. 2007. Improving virtual source method by wavefield separation. *Geophysics*, Accepted.

Mehta, K., Snieder, R., & Graizer, V. 2007. Downhole receiver function: a case study. *Bulletin of Seismological Society of America*, In Revision.

Mehta, K., Sheiman, J., Snieder, R., & Calvert, R. 2007. Virtual source method applied to Mars OBC data for time-lapse monitoring. *Geophysics*, In Revision.

Paffenholz, J., & Barr, F. J. 1995. An improved method for deriving water-bottom reflectivities for processing dual-sensor ocean-bottom cable data. *65th Annual Meeting, SEG, Expanded Abstracts*, 987-990.

Parvulescu, A. 1995. Matched-signal("MESS") processing by the ocean. *Journal of Acoustical Society of America*, **98(2)**, 943-960.

Petrashen, G. I., & Nakhamkin, S. A. 1973. Continuation of wave fields in exploration seismology (Prodolzhenie volnovykh polei v zadachach seismorazvedki): Nauka (in Russian).

Phinney, R. A. 1964. Structure of the Earth's Crust from Spectral Behavior of Long-Period Body Waves. *Journal of Geophysical Research*, **69(14)**, 2997-3017.

Poletto, F., & Miranda, F. 2004. Seismic while drilling: Fundamentals of Drill-Bit Seismic for Exploration. *Pergamon-Elsevier, Amsterdam, The Netherlands*.

Ramesh, D. S., Kind, R., & Yuan, X. 2002. Receiver function analysis of the North American crust and upper mantle. *Geophysical Journal International*, **150**, 91-108.

Riley, D. C., & Claerbout, J. F. 1976. 2-D multiple reflections. *Geophysics*, **41**, 592-620.

Robinson, E. A. 1999. Seismic Inversion and Deconvolution. Part B: Dual-sensor technology. *Pergamon-Elsevier, Amsterdam, The Netherlands.*

Sabra, K. G., Gerstoft, P., Roux, P., & Kuperman, W. A. 2005. Extracting time-domain Green's function estimates from ambient seismic noise. *Geophysics Research Letters*, **32**, L03310, doi:10.1029/2004GL021862.

Schalkwijk, K. M., Wapenaar, C. P. A., & Verschuur, D. J. 1999. Application of two-step decomposition to multicomponent ocean-bottom data: Theory and Case Study. *Journal of Seismic Exploration*, **8**, 261-278.

Schalkwijk, K. M., Wapenaar, C. P. A., & Verschuur, D. J. 2003. Adaptive decomposition of multicomponent ocean-bottom seismic data into downgoing and upgoing P- and S-waves. *Geophysics*, **68(3)**, 1091-1102.

Schmidt, H., & Tango, G. 1986. Efficient global matrix approach to the computation of synthetic seismograms. *Geophysical Journal of Royal Astronomical Society*, **84**, 331-359.

Schuster, G. T., Yu, J., Sheng, J., & Rickett, J. 2004. Interferometric/daylight seismic imaging. *Geophysical Journal International*, **157** 838-852.

Shakal, A., Hipley, P., & Graizer, V. 2004. CSMIP Instrumented Geotechnical Arrays. *Proceeding of the International Workshop for Site Selection, Installation and Operation of Geotechnical Strong-Motion Arrays: Workshop 1, Inventory of Current and Planned Arrays*, 14 and 15 October 2004, Los Angeles.

Shapiro, N. M., & Campillo, M. 2004. Emergence of broadband Rayleigh waves from correlations of the ambient seismic noise. *Geophysics Research Letters*, **31**, L07614, doi10.1029/2004GL019491.

Shapiro, N. M., Campillo, M., Stehly, L., & Ritzwoller, M. H. 2005. High-resolution surface-wave tomography from ambient seismic noise. *Science*, **307**, 1615-1618.

Sheehan, A. F., Abers, G. A., Jones, C. H., & Lerner-Lam, A. L. 1995. Crustal thickness variations across the Colorado Rocky Mountains from teleseismic receiver functions. *Journal of Geophysical Research*, **100**, 20391-20404.

Sheriff, R. E. 1999. Encyclopedia Dictionary of Exploration Geophysics. *Society of Exploration Geophysicists.*

Slob, E., & Wapenaar, K. 2007. Electromagnetic Green's function retrieval by cross-correlation and cross-convolution in media with losses. *Geophysical Research Letters*, **34**, L05307, doi:10.1029/2006GL029097.

Snieder, R. 2004. Extracting the Green's function from the correlation of coda waves: A derivation based on stationary phase. *Physics Review E*, **69**, 046610.

Snieder, R., Wapenaar, K., & Larner, K. 2006. Spurious multiples in interferometric imaging of primaries. *Geophysics*, **71**, SI65-SI78.

Snieder, R., Sheiman, J., & Calvert, R. 2006. Equivalence of the virtual source method and wavefield deconvolution in seismic interferometry. *Physics Review E*, **73**, 066620.

Snieder, R., & Şafak, E. 2006. Extracting the building response using seismic interferometry; theory and application to the Millikan Library in Pasadena, California. *Bulletin of Seismological Society of America*, **96(2)**, 586-598.

Snieder, R., Wapenaar, K., & Wegler, U. 2007. Unified Greens function retrieval by cross-correlation; connection with energy principles, *Physical Review E.*, **75**, 036103.

Soubaras, R. 1996. Ocean bottom hydrophone and geophone processing. *66th Annual Meeting, SEG, Expanded Abstracts*, 24-27.

Toksöz, M. N., Cheng, C. H., & Timur, A. 1976. Velocities of seismic waves in porous rocks *Geophysics*, **41**, 621-645.

Trampert, J., Cara, M., & Frogneux, M. 1993. SH propagator matrix and Q_s estimates from borehole- and surface-recorded earthquake data. *Geophysical Journal International*, **112**, 290-299.

van Vossen, R., Trampert, J., & Curtis, A. 2004. Propagator and wave-equation inversion for near-receiver material properties. *Geophysical Journal International*, **157**, 796-812.

van Wijk, K. 2006. On estimating the impulse response between receivers in a controlled ultrasonic experiment. *Geophysics*, **71**, SI79-SI84.

Vasconcelos, I., & Snieder, R. 2006. Interferometric imaging by deconvolution: Theory and numerical examples. *75th Annual Meeting, SEG, Expanded Abstracts*, 2416-2419.

Vasconcelos, I., & Snieder, R. 2007. Representation theorems and Green's function retrieval in perturbed acoustic media. *Physics Review E.*, In preparation.

Vasconcelos, I., & Snieder, R. 2007. Interferometry by deconvolution – Theory and numerical examples. *Physics Review E.*, In preparation.

Vasconcelos, I., & Snieder, R. 2007. Interferometry by deconvolution – Application to drill-bit seismic imaging. *Geophysics*, In preparation.

Vasconcelos, I., Snieder, R., Taylor, S. T., Sava, P., Chavarria, J. A., & Malin, P. 2007. High Resolution Imaging of the San Andreas Fault at Depth. *Geophysical Research Letters*, In preparation.

Vasconcelos, I., Snieder, R., & Hornby, B. 2007. Imaging with internal multiples from subsalt VSP data: examples of target-oriented interferometry. *Geophysics*, In preparation.

Wald, D. J., Helmberger, D. V., & Heaton, T. H. 1991. Rupture Model of the 1989 Loma Prieta earthquake from the inversion of strong-motion and broadband teleseismic data. *Bulletin of the Seismological Society of America*, **81(5)**, 1540-1572.

Wapenaar, C. P. A, Herrmann, P., Verschuur, D. J., & Berkhout, A. J. 1990. Decomposition of multicomponent seismic data into primary P- and S-wave responses. *Geophysical Prospecting*, **38**, 633-661.

Wapenaar, C.P.A. 1992. The Infinite Aperture Paradox. *Journal of Seismic Exploration*, **1**. 325-336.

Wapenaar, K. 2004. Retrieving the elastodynamic Green's function of an arbitrary inhomogeneous medium by cross-correlation. *Physics Review Letters*, **93**, 254301.

Wapenaar, K., Fokkema, J., & Snieder, R. 2005. Retrieving the Green's function by crosscorrelation: a comparison of approaches. *Journal of Acoustical Society of America*, **118**, 2783-2786.

Wapenaar, K., & Fokkema, J. 2006. Green's function representations for seismic interferometry. *Geophysics*, **71(4)**, SI33-SI46.

Wapenaar, K., & Slob, E. 2006. Unified Green's function retrieval by crosscorrelation. *Physical Review Letters*, **97**, 234301.

Wilson, D., Aster, R., Ni, J., Grand, S., West, M., Gao, W., Baldridge, W. S., & Semken, S. 2005. Imaging the seismic structure of the crust and upper mantle beneath the Great Plains, Rio Grande Rift, and Colorado Plateau using receiver functions. *Journal of Geophysical Research*, **110**, B05306, doi : 10.1029/2004JB003492.

Wilson, D., & Aster, R. 2003. Imaging crust and upper mantle seismic structure in the southwestern United States using teleseismic receiver functions. *The Leading Edge*, 232-237.

Yilmaz, O. 2001. Seismic Data Analysis. *SEG*, **vol. 1**.

Appendix A

Derivation of combining the propagator matrices

The displacement and stress for an SH wave at a depth z can be expressed as matrix multiplication of the propagator matrix and the values at the free surface ($z=0$) (Aki and Richards, 2002). Since the traction at the free surface is zero, we can write the multiplication as

$$\left(\begin{array}{c} u_y(z,\omega) \\ \sigma_{yz}(z,\omega) \end{array} \right) = P^{SH}(z,0) \left(\begin{array}{c} u_y(z=0,\omega) \\ 0 \end{array} \right) \tag{A.1}$$

$$\Rightarrow u_y(z,\omega) = P_{11}^{SH}(z,0)u_y(z=0,\omega). \tag{A.2}$$

A similar expression for the P-SV system is given by

$$\left(\begin{array}{c} u_x(z,\omega) \\ iu_z(z,\omega) \\ \sigma_{xz}(z,\omega) \\ i\sigma_{zz}(z,\omega) \end{array} \right) = P^{PSV}(z,0) \left(\begin{array}{c} u_x(z=0,\omega) \\ iu_z(z=0,\omega) \\ 0 \\ 0 \end{array} \right) \tag{A.3}$$

$$\Rightarrow u_x(z,\omega) = P_{11}^{PSV}(z,0)u_x(z=0,\omega) + iP_{12}^{PSV}(z,0)u_z(z=0,\omega), \tag{A.4}$$

$$iu_z(z,\omega) = P_{21}^{PSV}(z,0)u_x(z=0,\omega) + iP_{22}^{PSV}(z,0)u_z(z=0,\omega). \tag{A.5}$$

Equations (A.2), (A.4) and (A.5) can be combined to give the following system of equations:

$$\begin{aligned} u_y(z,\omega) &= P_{11}^{SH}(z,0)u_y(z=0,\omega), \\ u_x(z,\omega) &= P_{11}^{PSV}(z,0)u_x(z=0,\omega) + iP_{12}^{PSV}(z,0)u_z(z=0,\omega), \\ u_z(z,\omega) &= -iP_{21}^{PSV}(z,0)u_x(z=0,\omega) + P_{22}^{PSV}(z,0)u_z(z=0,\omega). \end{aligned} \tag{A.6}$$

This system of equations can be re-written in matrix form as

$$\left(\begin{array}{c} u_x(z,\omega) \\ u_y(z,\omega) \\ u_z(z,\omega) \end{array} \right) = P(z,0) \left(\begin{array}{c} u_x(z=0,\omega) \\ u_y(z=0,\omega) \\ u_z(z=0,\omega) \end{array} \right), \tag{A.7}$$

where

$$P(z,0) = \left(\begin{array}{ccc} P_{11}^{PSV}(z,0) & 0 & iP_{12}^{PSV}(z,0) \\ 0 & P_{11}^{SH}(z,0) & 0 \\ -iP_{21}^{PSV}(z,0) & 0 & P_{22}^{PSV}(z,0) \end{array} \right) \tag{A.8}$$

is the propagator matrix relating the displacements at a depth z with the displacements at the free surface $(z=0)$.

Appendix B

Solving for the propagator matrix elements in terms of displacements

For a homogeneous lossless medium, following are the expressions for the elements of SH and P-SV propagator matrices, as obtained from Aki and Richards (2002) and simplified to agree with the expressions given by van Vossen, et al. (2004).

$$
\begin{aligned}
P_{11}^{SH}(z,0) &= 2\cos(i\nu z) \\
&= 2\cos(\omega q_s z),
\end{aligned}
\tag{B.1}
$$

$$
\begin{aligned}
P_{11}^{PSV}(z,0) &= 1 + \frac{2\mu}{\omega^2\rho}\left[2k^2\sinh^2\left(\frac{\gamma z}{2}\right) - (k^2+\nu^2)\sinh^2\left(\frac{\nu z}{2}\right)\right] \\
&= 2\beta^2 p^2 \cos[\omega(q_p z)] + (1 - 2\beta^2 p^2)\cos[\omega(q_s z)],
\end{aligned}
\tag{B.2}
$$

$$
\begin{aligned}
P_{12}^{PSV}(z,0) &= \frac{k\mu}{\omega^2\rho}\left[(k^2+\nu^2)\frac{\sinh\gamma z}{\gamma} - 2\nu\sinh\nu z\right] \\
&= \left(\frac{-p(1-2\beta^2 p^2)}{q_p}\right)\sin[\omega q_p z] + 2\beta^2 p q_s \sin[\omega q_s z] \\
\Rightarrow iP_{12}^{PSV}(z,0) &= \frac{-ip}{q_p}(1-2\beta^2 p^2)\sin[\omega q_p z] + 2i\beta^2 p q_s \sin[\omega q_s z],
\end{aligned}
\tag{B.3}
$$

$$
\begin{aligned}
P_{21}^{PSV}(z,0) &= \frac{k\mu}{\omega^2\rho}\left[(k^2+\nu^2)\frac{\sinh\nu z}{\nu} - 2\gamma\sinh\gamma z\right] \\
\Rightarrow -iP_{21}^{PSV}(z,0) &= \frac{ip}{q_s}(1-2\beta^2 p^2)\sin[\omega q_s z] - 2i\beta^2 p q_p \sin[\omega q_p z],
\end{aligned}
\tag{B.4}
$$

$$
\begin{aligned}
P_{22}^{PSV}(z,0) &= 1 + \frac{2\mu}{\omega^2\rho}\left[2k^2\sinh^2\left(\frac{\nu z}{2}\right) - (k^2+\nu^2)\sinh^2\left(\frac{\gamma z}{2}\right)\right] \\
\Rightarrow P_{22}^{PSV}(z,0) &= 2\beta^2 p^2 \cos[\omega(q_s z)] + (1 - 2\beta^2 p^2)\cos[\omega(q_p z)],
\end{aligned}
\tag{B.5}
$$

where k is horizontal wavenumber, μ is shear modulus and ρ is density. ν is the vertical wavenumber for S-waves and γ is the vertical wavenumber for P-waves ($\nu = \omega q_s$ and $\gamma = \omega q_p$). In the absence of attenuation, both ν and γ are real valued.

As shown by van Vossen, et al. (2004), for lossless medium, we can solve eq. (A.7) for the components of the propagator matrix. To solve for the propagator matrix elements, we start with eq. (A.7) re-written as

$$
\begin{pmatrix} u_x(z,\omega) \\ u_y(z,\omega) \\ u_z(z,\omega) \end{pmatrix} = \begin{pmatrix} P_{11}^{PSV}(z,0) & 0 & iP_{12}^{PSV}(z,0) \\ 0 & P_{11}^{SH}(z,0) & 0 \\ -iP_{21}^{PSV}(z,0) & 0 & P_{22}^{PSV}(z,0) \end{pmatrix} \begin{pmatrix} u_x(z=0,\omega) \\ u_y(z=0,\omega) \\ u_z(z=0,\omega) \end{pmatrix}. \quad \text{(B.6)}
$$

Since the diagonal elements are real and the off-diagonal elements are imaginary, the system of equations in eq. (B.6) can be expressed as

$$
\begin{aligned}
Re(u_x(z,\omega)) + iIm(u_x(z,\omega)) &= P_{11}^{PSV}(z,0)[Re(u_x(z=0,\omega)) + iIm(u_x(z=0,\omega))] + \\
&\quad iP_{12}^{PSV}(z,0)[Re(u_z(z=0,\omega)) + iIm(u_z(z=0,\omega))], \\
Re(u_z(z,\omega)) + iIm(u_z(z,\omega)) &= -iP_{21}^{PSV}(z,0)[Re(u_x(z=0,\omega)) + iIm(u_x(z=0,\omega))] + \\
&\quad P_{22}^{PSV}(z,0)[Re(u_z(z=0,\omega)) + iIm(u_z(z=0,\omega))].
\end{aligned}
$$

$$\text{(B.7)}$$

In order to solve for the propagator matrix elements, we equate the real and imaginary parts to give the following equations:

$$
\begin{aligned}
Re(u_x(z,\omega)) &= P_{11}^{PSV}(z,0)Re(u_x(z=0,\omega)) - P_{12}^{PSV}(z,0)Im(u_z(z=0,\omega)), \\
Im(u_x(z,\omega)) &= P_{11}^{PSV}(z,0)Im(u_x(z=0,\omega)) + P_{12}^{PSV}(z,0)Re(u_z(z=0,\omega)), \\
Re(u_z(z,\omega)) &= P_{21}^{PSV}(z,0)Im(u_x(z=0,\omega)) + P_{22}^{PSV}(z,0)Re(u_z(z=0,\omega)), \\
Im(u_z(z,\omega)) &= -P_{21}^{PSV}(z,0)Re(u_x(z=0,\omega)) + P_{22}^{PSV}(z,0)Im(u_z(z=0,\omega)).
\end{aligned}
$$

$$\text{(B.8)}$$

Solving this system of equations for the elements of propagator matrix gives

$$P_{11}^{SH}(z,0) = \frac{u_y(z,\omega)}{u_y(z=0,\omega)},$$

$$P_{11}^{PSV}(z,0) = \frac{Re(u_x(z,\omega))Re(u_z(z=0,\omega)) + Im(u_x(z,\omega))Im(u_z(z=0,\omega))}{Re(u_x(z=0,\omega))Re(u_z(z=0,\omega)) + Im(u_x(z=0,\omega))Im(u_z(z=0,\omega))},$$

$$P_{12}^{PSV}(z,0) = \frac{i[Re(u_x(z=0,\omega))Im(u_x(z,\omega)) - Im(u_x(z=0,\omega))Re(u_x(z,\omega))]}{Re(u_x(z=0,\omega))Re(u_z(z=0,\omega)) + Im(u_x(z=0,\omega))Im(u_z(z=0,\omega))},$$

$$P_{21}^{PSV}(z,0) = \frac{-i[Re(u_z(z=0,\omega))Im(u_z(z,\omega)) - Im(u_z(z=0,\omega))Re(u_z(z,\omega))]}{Re(u_x(z=0,\omega))Re(u_z(z=0,\omega)) + Im(u_x(z=0,\omega))Im(u_z(z=0,\omega))},$$

$$P_{22}^{PSV}(z,0) = \frac{Re(u_x(z=0,\omega))Re(u_z(z,\omega)) + Im(u_x(z=0,\omega))Im(u_z(z,\omega))}{Re(u_x(z=0,\omega))Re(u_z(z=0,\omega)) + Im(u_x(z=0,\omega))Im(u_z(z=0,\omega))}.$$

$$(B.9)$$

Hence, for a homogeneous medium, the propagator matrix elements can be expressed in terms of displacements at the depth of interest z and at the free surface (z=0).